1-1-2014

Visualizing Interior And Exterior Jet Aircraft Noise

Manmohan Singh Moondra
Wayne State University,

VISUALIZING INTERIOR AND EXTERIOR JET AIRCRAFT NOISE

by

MANMOHAN S. MOONDRA

DISSERTATION

Submitted to the Graduate School

of Wayne State University,

Detroit, Michigan

in partial fulfillment of the requirements

for the degree of

DOCTOR OF PHILOSOPHY

2014

MAJOR: MECHANICAL ENGINEERING

Approved by:

_____

Advisor Date

_____

_____

_____

ACKNOWLEDGEMENTS

To my wife, Jasmine, without whose constant 'motivation' this dissertation never would have been completed

To my daughter, Simrit. I'm hoping she'll grow up to be an engineer.

To my parents, for their unconditional support.

To Dr. Sean F. Wu, for his mentorship and friendship over the far-too-many years it took to complete this dissertation.

To Dr. Nassif Rayess, whose guidance in the early days of this research was invaluable

TABLE OF CONTENTS

LIST OF FIGURES

CHAPTER 1 - INTRODUCTION

1.1 Background

In today's competitive aerospace industry, the quest for quiet has drawn significant attention to both the interior and exterior design of an airplane. It is becoming increasingly important in airplane design to consider noise and vibration, which now define the quality of an airplane. Passenger comfort requirements make it critical for the airplane designer to understand the mechanisms of noise transmission into the airplane fuselage.

Techniques to reduce the airplane fuselage noise level, such as double wall with insulation bags and application of damping material, are well known. However, application of these techniques is constrained by the weight and available space of acoustics treatment. The constraints are particularly severe for small to midsize business jets. Noise source localization and source strengths ranking play an import role in the design of the acoustics packages because they help the acoustic engineer to optimize the acoustic package. To achieve this in a cost-effective manner, engineers must have a reliable and robust noise and vibration diagnostic tool. Information thus obtained is useful for incorporating the optimal noise reduction measures.

Modern propulsive supersonic jets produce exterior noise sources with a high amplitude noise field and complicated characteristics, which makes them very difficult to characterize. In particular, there are turbulent eddies that are moving through the supersonic jet at high speeds along the jet boundary. These eddies in the shear layer produce a directional and frequency dependent noise. There is a need for a robust,

portable and accurate noise diagnostic tool to acquire the characteristics of an acoustic field produced by a full-scale jet engine.

Traditionally, noise diagnostics are done through ad hoc or trial and error approaches, or through measurement techniques that do not provide sufficient information to make good engineering decisions. An example is the measurement of vibration responses using accelerometers mounted on the surface or laser vibrometer scanning of surface vibration. Another method is to measure the SPL values and spectra at a few points around a vibrating structure. Noise diagnosis can also be performed by using an intensity probe that sweeps over the entire source surface at very close range. This approach is feasible only when the source surface is smooth and flat.

Combining vibration and acoustic measurement is another popular method that can be used to measure noise. This is achieved by correlating the SPL values and spectra in the field to the vibration responses of a structure and, in a similar fashion, correlating the intensity mapping to the vibration responses of a structure to identify possible causes of sound radiation of a vibration structure. Even so, the diagnostic process can be expensive and time consuming. Moreover, vibration and acoustic responses measured using traditional methods such as accelerometers, laser vibrometers, microphones, or intensity probes are valid at locations of measurements only. Because of this limitation, the results may be inconclusive and misleading.

While sound is generated by vibration, not all vibrations can produce sound. Therefore, there may not be a direct correlation between measured sound and vibrations,

or the conclusion drawn may be incorrect. Moreover, the measured values are discrete and uncorrelated, so it is not possible to get a global view of a sound field.

To increase the data output capabilities of noise diagnostics, numerical methods were devised in the early twentieth century. Due to the limited scope of computers and daunting computation times, however, these methods were not well received. With the introduction of more efficient and affordable computers in the eighties, an increasing number of noise engineers started searching for methodologies that combined numerical solutions with measurements to characterize the acoustic behavior of their products. The most prominent method is known as Nearfield Acoustic Holography[9] (NAH), which can visualize the acoustic field in a very cost-efficient manner. NAH enables one to reconstruct the entire acoustic field, both in the forward and backward directions. The insight one can gain into the acoustic characteristics of a sound source from NAH cannot be matched by any of the aforementioned traditional methods.

However, there remained many difficulties in reconstructing the acoustic field on the source surface due to an ill-posedness problem inherent in an inverse acoustic radiation problem. Moreover, the conventional NAH is derived for geometry whose coordinates are separable[22], such as an infinite plane, an infinite cylinder[21, 24], and a sphere. Thus is not suitable for an arbitrarily shaped structure such as a vehicle or an airplane. For an arbitrary surface, one approach is to use the Helmholtz integral formulation with boundary element method (BEM)[17]. This BEM-based NAH[23] is advantageous for many reasons, but it has several inherent shortcomings that will be discussed under Subchapter 1.4. These shortcomings severely limit the application of this

methodology to diagnose airplane noise and vibrations. Over the past two decades much progress has been made in improving the efficiency and accuracy of NAH, so that it now allows for reconstruction of the acoustic quantities over the source surface based upon two-dimensional acoustic pressure measurements in the field[18, 25].

1.2 Holography

The terms holograms and holography were originally coined by Dennis Gabor (known to be the father of holography) in 1947. The word hologram is derived from the Greek words "holos," meaning whole or complete, and "gram," meaning message. Older English dictionaries define a hologram as a document which is handwritten by the person whose signature is attached. Since then, the definition of holography has evolved to include applications within the field of photography as well.

In regular photography, an image is recorded on unexposed film, and the product is the recording of the differing intensities of the light reflected by the object and imaged by a lens. Instead, a hologram is a photographic record of an interference pattern. The interference between an undisturbed reference light wave front (Figure 1.1a) and one reflected by an object is photographically recorded on the hologram plate (Figure 1.1b). Hence a hologram is an image of the constructive and destructive interference patterns of the reflected wave front of the object (Figure 1.2). However, there is a special difference between photography and holography, which makes holograms so unique.

If a hologram is broken or cut up, each small portion contains information about the whole object. This is because the light bouncing from each point on the object is not focused to a point on the film, but is allowed to spread out through space between the

object and the film. The light thus covers a large portion of the film and interferes with the reference beam throughout that whole portion of the film as if each point were a spray of light, each with a certain angle of divergence. Hence, every point is coded into a large area of the hologram. In other words, there is enough information on the two-dimensional hologram to recreate the complete three-dimensional object.

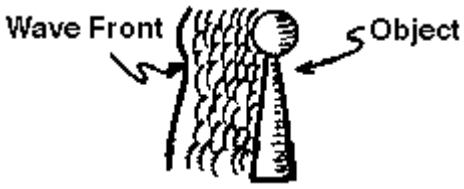

(a) (b)

Figure 1.1: The principle and setup for holography

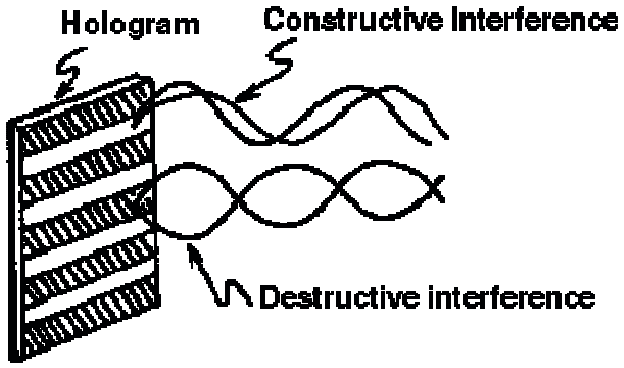

Figure 1.2: Recording of interference pattern on the hologram.

With time, any methodology that aims at reconstructing the entire three-dimensional field based upon finite observations on a two-dimensional plane is assumed as another variant of holography. Thus, in modern times, the field of holography is not

merely limited to optics. Acoustic holography, which appeared in the mid sixties[4], is an example of a similar methodology. In acoustic holography, a coherent beam of ultrasonic waves, instead of light, is used. The resulting interference pattern is recorded with microphones to form a hologram, which, when viewed with laser light, produces a visible three-dimensional image. Holography has been combined with microscopy to study very small objects; it also has industrial applications for stress and vibrational analysis.

1.3 Nearfield Acoustic Holography

Nearfield Acoustic holography[1] is a methodology employed to visualize acoustic radiation from a vibrating object by taking acoustic pressure measurements in the nerarfield around the object. It is a forward problem if the reconstruction surface is outside the measurement surface (away from the source), but is an inverse problem if the reconstruction surface is inside (toward the source). For an inverse problem, only source details greater than the acoustic wavelength can be retrieved in acoustic holography. This Fourier transform-based approach, which was developed by William *et al.* (1980), Maynard *et al.* (1985), and Veronesi and Maynard (1987)[17, 18] is the first implementation of Near-field Acoustic Holography (NAH). In NAH, the measurements are taken over a two-dimensional hologram surface very close to the source surface in order to increase the resolution of reconstruction.

NAH reconstructs the acoustic field in the entire three-dimensional field, including the source surface, based upon near-field acoustic pressure measurements[11]. Theoretically, the resolution is unlimited provided that all the nearfield effects can be captured in the measurements[22]. Nearfield acoustic holography (NAH) is different from traditional acoustic holography in that it can yield unlimited resolution by measuring all

the nearfield information. The original NAH is developed for source geometry whose coordinates are separable, i.e., planar, cylindrical, and spherical NAH. The solution of the inverse problems in these techniques relies on the expansion of pressure field in terms of a complete set of eigenfunctions corresponding to the source geometry.

For practical applications, the Fourier transform-based NAH can be performed in steps as follows:

1. First, a coordinate system needs to be selected for a given source structure. If this source structure is plate-like or is composed of planar surfaces, the rectangular coordinate system should be used. If the source surface is cylindrical in shape, the cylindrical coordinate should be used and similarly spherical shaped sources can be reconstructed by selecting the spherical coordinate system.
2. Once a coordinate system is selected, a measurement hologram surface is set up conformal to the source surface to measure acoustic pressure. For planar NAH, the measurement aperture should be at least four times the size of source surface to ensure that sufficient information is captured[9,22] .
3. In practice, the measurement distance should be kept as close to the source surface as possible, because the spatial resolution of reconstruction of acoustic quantities is dependent upon the measurement distance and signal to noise ratio. Theoretically, if the desired spatial resolution in the *x*-axis direction is $R_x=\lambda_x/2$, where λ_x is the wavelength of the shortest structural wave in the x-axis direction. With S/N=D, the measurement distance should be less than

$d<(R_x D)/(20\ \pi \log e)$[22]. The higher the required resolution, the shorter the measurement distance will be and the higher the S/N ratio, the farther the measurement aperture can be.

4. Microphone spacing is another important variable to consider. Microphone spacing should be equal to or less than the measurement distance. If microphone spacing is larger than that, it will result in an insufficient spatial sampling and result in aliasing in reconstruction results.
5. Once the measurement aperture size is known and microphone spacing has been decided, one can calculate the number of microphones needed in the measurement array.

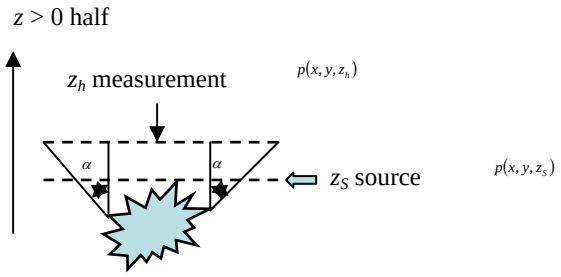

Figure 1.3: Typical measurement setup for planar NAH.

In reality, the noise source surfaces are seldom exactly planar, cylindrical or spherical. Fourier transform-based NAH can still be used for arbitrarily shaped structures except that reconstruction results are only valid in a source-free region bounded by two parallel or concentric surfaces. For exterior problem and for a rectangular source surface, one of these two parallel surfaces will be tangential to the source surface (z_s in Figure 1.3) and the other is at infinity. This approach will not be applicable to the interior region though, because the source-free requirement may not be met. In a similar fashion, for

cylindrical and spherical coordinate systems in an exterior region, one concentric surface can be the minimum surface that circumscribes the source surface, and the other is at infinity. As previously for the rectangular surface, this methodology is not valid in the interior region for a cylindrical coordinate system because the source-free requirement is not met in an enclosed cylindrical surface. However, this approach is valid for the spherical coordinate system as long as the sources are outside a maximum sphere that is tangential to the interior surface of the cavity. Note that the reconstruction results will be valid only inside this maximum sphere and there is no method to reconstruct acoustic quantities on the interior source surface.

Once all guidelines are satisfied, acoustic pressure measurements are acquired over the hologram surface and Fast Fourier transforms are taken with respect to time to obtain spectral information for the collected acoustic pressures. Another Fast Fourier transform is then taken with respect to the spectral variable to convert the acoustic pressure into wave number domain. Now the measured pressure can projected in the 3D space by using the relation

$$P(k_x, k_y, z) = P(k_x, k_y, z_h) e^{ik_z(z-z_h)} \tag{1.1}$$

in which $P(k_x, k_y, z)$ and $P(k_x, k_y, z_h)$ are the angular spectra of acoustic pressures computed at the measurement and a parallel surface in a source-free region, respectively. k_x and k_y are the wave numbers of the structural waves in the *x*- and *y*- axis directions, respectively, and $e^{ik_z(z-z_h)}$ is known as the propagator for reconstructing the acoustic

pressure. It is essentially a phase shift from the hologram/measurement surface to any parallel plane surface. Also,

$$k_z = \sqrt{k^2 - (k_x^2 + k_y^2)} \tag{1.2}$$

is the wave number in the direction of wave propagation. Note that when $(k_x^2 + k_y^2)$ is more than the acoustic wave number *k*, k_z is purely imaginary and the amplitude of acoustic pressure decays exponentially with distance z. These fast-decaying waves are known as evanescent waves. These waves essentially stay on the surface and the acoustic energy never propagates to the far-field. Since the evanescent waves decay exponentially with distance in the far-field measurement, spatial resolution of near-field acoustic holography is limited to the wavelength of an acoustic wave of interest[28]. On the other hand, when $(k_x^2 + k_y^2)$ is less than the acoustic wave number, k_z is real and a propagating acoustic wave is produced. It can then be deduced that all sound is produced by vibration, but not all vibrations produce sound. When $k = k_x^2 + k_y^2$, $k_z = 0$ and coincidence frequency is reached. The coincidence frequency is defined as the optimum efficiency that is achieved when a structure is vibrating such that the wavelength of flexural waves in the plate is equal to the wavelength of acoustic waves in the air[34].

Thus, the angular spectrum at any parallel plane to the hologram surface can be obtained by multiplying the angular spectrum at the hologram surface with the propagator or phase shift between the two planes. Note that this is true regardless of whether it is a forward problem (reconstruction plane away from hologram surface) or an inverse problem (reconstruction plane towards or on the source surface, z_s)[33]. Once we have the

angular spectrum the acoustic pressure in frequency domain can be obtained by taking an inverse spatial Fourier transform[22],

$$\hat{p}(x,y,z) = \Im_x^{-1}\Im_y^{-1}\left\{P(k_x,k_y,z_h)\,e^{ik_z(z-z_h)}\right\} \tag{1.3}$$

Once we have reconstructed the acoustic pressure, we can reconstruct the particle velocity and acoustic intensity on any parallel surface by using Euler's equation,

$$\hat{v}(x,y,z) = \Im_x^{-1}\Im_y^{-1}\left\{P(k_x,k_y,z_h)\frac{k_z}{\rho_0 ck}e^{ik_z(z-z_h)}\right\} \tag{1.5}$$

in which $\frac{k_z}{\rho_0 ck}e^{ik_z(z-z_h)}$ is the propagator for particle velocity.

$$I_{av}(x,y,z) = \frac{1}{2}\mathrm{Re}\left[\hat{p}(x,y,z)\hat{v}^*(x,y,z)\right] \tag{1.6}$$

in which $\hat{v}^*(x,y,z)$ is the conjugate of reconstructed particle velocity.

As shown in equations (1.1)-(1.6), once acoustic pressures are measured in the near-field of a source structure, all acoustic quantities in the source-free region over the planes parallel to the measurement surface, including the structural waves travelling on the target source surface, can be reconstructed.

We can deduce similar equations for cylindrical and spherical coordinates. For cylindrical coordinates we can write the NAH equations for reconstructing acoustic pressure on the source surface[22],

$$\hat{p}(r_s,\phi,z)=\Im_{\phi}^{-1}\Im_{z}^{-1}\left\{P(r_h,\phi,z)\frac{H_n^{(1)}(k_r r_s)}{H_n^{(1)}(k_r r_h)}\right\} \tag{1.7}$$

in which $\Im_{\phi}^{-1}$ and $\Im_{z}^{-1}$ are inverse Fourier transforms with respect to the cylindrical ϕ- and z- axes, $P(r_h,\phi,z)$ is the angular spectrum of the measured acoustic pressure at the hologram surface, and $H_n^{(1)}(k_r r_s)$ and $H_n^{(1)}(k_r r_h)$ are cylindrical Hankel functions of the first kind for the source surface and the hologram surface, respectively. The particle velocity can be calculated as

$$\hat{v}(r_s,\phi,z)=\Im_{\phi}^{-1}\Im_{z}^{-1}\left\{P(r_h,\phi,z)\frac{k_r}{i\rho_0 ck}\frac{H_n'^{(1)}(k_r r_s)}{H_n^{(1)}(k_r r_h)}\right\} \tag{1.8}$$

In the spherical coordinate system, the acoustic pressure in the source-free region can be reconstructed with the following equation similar to the ones used for rectangular and cylindrical coordinates[22].

$$\hat{p}(r_s,\theta,\phi)=\Im_{\theta}^{-1}\Im_{\phi}^{-1}\left\{P(r_s,\theta,\phi)\frac{h_n^{(1)}(kr_s)}{h_n^{(1)}(kr_h)}\right\} \tag{1.9}$$

in which $\Im_{\theta}^{-1}$ and $\Im_{\phi}^{-1}$ are inverse Fourier transforms with respect to the spherical θ- and ϕ- axes, $P(r_s,\theta,\phi)$ is the angular spectrum of the measured acoustic pressure at the hologram surface, and $h_n^{(1)}(kr_s)$ and $h_n^{(1)}(kr_h)$ are spherical Hankel functions of the first kind for the source surface and the hologram surface, respectively. The particle velocity can be calculated as

$$\hat{v}(r_s,\theta,\phi) = \Im_\theta^{-1}\Im_\phi^{-1}\left\{P(r_s,\theta,\phi)\frac{1}{i\rho_0 c}\frac{h_n'^{(1)}(kr_s)}{h_n^{(1)}(kr_h)}\right\} \tag{1.10}$$

But all these techniques have their own inherent disadvantages. For example, the planar near field acoustic holography can be applied only to planar surfaces[29-33]. Secondly, reconstruction on arbitrary bodies using a planar hologram surface does not yield the true picture of acoustic quantities on the surface. Thirdly, wrap-around errors occur due to a finite size of measurement aperture in practice, leading to introduction of artificial wave numbers that are actually not present. As mentioned earlier, these wrap-around errors are substantially minimized by ensuring that measurement aperture is at least four times as large as the source surface[9, 22]. Hayek and Luce's research[35] has shown that sufficient reconstruction accuracy can be achieved even when the measurement aperture is reduced to the same size as the source surface[35].

Recently, patch NAH[36-39] has been developed. It uses analytic continuation of the patch pressure and singular value decomposition (SVD) to eliminate the need to cover the entire source surface with one large microphone array and take small "patches" of measurements with a smaller microphone array to scan a large object. Another aperture effect is caused by a sudden drop in acoustic pressure level at the edge of the measurement aperture. This effect can be alleviated by introducing a window function that effectively suppresses the contributions from regions outside the measurement aperture and gradually brings the amplitude of acoustic pressures to zero[40]. This spatial window is also known as the Turkey window[41], which uses cosine and rectangle windows to reduce the amplitude of the acoustic pressure to zero at the edges of the measurement aperture. Another limitation of near-field acoustic holography is that it cannot be used to

visualize acoustic radiation from an arbitrary source such as a vehicle. In particular, it cannot be used to reconstruct the acoustic field inside a vehicle passenger compartment and it is valid only for an exterior, unbounded region. Another interesting discovery is the use of measured acoustic intensity instead of acoustic pressures as input to reconstruct the acoustic field [42].

1.4 Inverse Boundary Element Method

For an arbitrary object, one can use the Helmholtz integral theory which correlates the radiated acoustic pressures to the surface acoustic quantities. This Helmholtz integral formulation can be implemented using BEM. The advantage of using the BEM-based NAH is the reduction of dimensionality of the problem by one. However, there are several inherent drawbacks to this method. The first drawback is that the integral equation may fail to yield a unique solution when the excitation frequency is close to one of the characteristic frequencies of the related interior boundary value problem (Schenck, 1968). While this non-uniqueness difficulty can be overcome by the CHIEF method (Schenck, 1968), the efficiency and accuracy of numerical calculations may be affected. The second drawback is its inherent ill-conditioning difficulty (Wang and Wu, 1997) in which the measured data are not error-free. Regularization can be achieved through singular value decomposition (SVD) to reduce the reconstruction errors. Even with this regularization, the accuracy of the reconstruction is still limited to the near field (Kim and Lee, 1990).

Another major drawback is that the number of measurements in the field must be comparable to that of the nodes discretized on the large surface[23]. Consequently, the effectiveness of this method can be severely hindered when hundreds (or even more) of

the discretized nodes are used to describe the surface acoustic pressure distribution, making practical diagnostics virtually impossible. Another disadvantage of BEM is that to avoid aliasing and acquire certain resolution in reconstruction, one must have a minimum number of nodes per wavelength on the surface, and take the same number of measurements in the field. By solving a matrix equation, the pressure amplitudes at the nodes on the surface can then be determined. Since the number of discrete nodes increases with the excitation frequency and complexity of the source geometry, this technique may become impractical for a finite-sized object such as a jet engine or the airplane fuselage in the low-to-mid frequency regime. This is because the corresponding number of measurements needed to reconstruct the acoustic pressure field would be too large to make this process cost-effective.

1.5 Research Objective

In 1997, a new methodology named Helmholtz Equation-Least Squares (HELS) for nearfield acoustic holography was introduced by Wang and Wu for radiation into the exterior region of vibrating objects (Wang and Wu, 1997; Wang, 1995; Wu, 2000). The HELS based nearfield acoustic holography was also extended to the interior region (Wu and Yu, 1998). This method utilizes an expansion of the spheroidal functions that satisfy the Helmholtz equation to represent the radiated acoustic pressure field. Such an expansion is uniformly convergent because the basis functions consist of a uniformly convergent series of Legendre functions. The coefficients associated with these basis functions are determined by requiring the assumed form solution to satisfy the pressure boundary condition at the measurement points. The errors incurred in this process are minimized by least-squares method, so that the solutions obtained are unique. The

advantages of this HELS method are that it is applicable to both exterior and interior regions and satisfactory reconstruction of 3D acoustic fields can be obtained with relatively few measurements. This is because the expansion functions represent a complete set of eigenfunctions that satisfy the Helmholtz equation.

The solution of inverse problem provided by the BEM based NAH requires discretization of the source geometry for expansion of the pressure field in terms of a complete set of eigenfunctions corresponding to the geometry. Moreover, the number of field measurements should be comparable to the discretized nodes on the surface. On the other hand, HELS does not require the source geometry discretization. This greatly simplifies the pre-processing time and also reduces the errors in the inverse solution introduced by the source surface discretization discrepancies.

For the HELS method, the number of field measurements is no more than that of the acoustic modes needed to reconstruct the radiated acoustic pressure field. This number is small when an appropriate coordinate system is selected for the particular source geometry under consideration. Furthermore, a small number of field pressure measurements can be used to reconstruct over a comparatively larger number of reconstruction locations, which is a major limitation in BEM based NAH methods. This makes the data acquisition process viable and very flexible to incorporate.

In the previous experimental[13, 14] and numerical[14, 15] investigations, only simple and smooth geometries were used to validate the HELS method. The present research provides insight into the behavior of HELS based nearfield acoustic holography for highly non-spherical vibrating structures with sharp edges and corners. This research

centers on the development of a real-world nearfield acoustic holography tool based on the HELS method. Use of this tool will yield an in-depth understanding of jet aircraft noise that cannot be obtained by conventional measurement and analysis technologies. Specifically, the engineers and designers will be able to visualize 3D images of a sound field produced by a jet engine as well as inside the airplane on fuselage surface. By slicing a 3D sound field at different angles and viewing it from different perspectives, engineers will be able to correlate jet noise to a jet stream and how the noise is transmitted into the fuselage. In particular, engineers will be able to see the frequency-dependent sound source distribution and their propagation in the 3D space, and quantify the major acoustic radiation angles and strength. The insight and knowledge thus gained will enable manufacturers to devise more cost-effective ways to reduce jet noise and its transmission into the fuselage, and the improved designs will lead to quieter jet engines offering significant advantage in industry and benefits to the public.

As discussed previously, the HELS method employs an expansion of spheroidal functions. This implies that reconstruction will be most accurate for spherical sources. On the other hand, the vibrating structures chosen for numerical and experimental validations are highly non-spherical in nature. Thus, this study also serves as a test of robustness and versatility of the HELS method for general three-dimensional complex structures and its application in the visualization of aerodynamically generated sounds.

1.6 Thesis Overview

In this investigation, the Helmholtz Equation Least Squares (HELS) method is used for reconstruction of the acoustic field in the interior of a fuselage and around a full scale jet engine. The results of in-flight nearfield acoustic holography measurements

inside the fuselage of a business jet will be presented. A circumferential microphone array will be built to take acoustic pressure measurements inside the aircraft fuselage along the fuselage in the longitudinal direction. The measured acoustic pressures will then be taken as input to the HELS codes to reconstruct the entire acoustic field in the interior region. In addition, the interior cabin acoustic modes will also be reconstructed and visualized. This experiment will demonstrate that the HELS based NAH can become a useful tool to acquire a better understanding of the acoustic field inside an arbitrary interior region.

Experimental validations will also be presented for an aircraft jet engine in the exterior region. Arrays of microphones and stands will be designed and built so that conformal measurements of sound pressures can be taken around the jet plume. Two circular rings will be designed to hold microphone arrays. One ring is to be placed around the inlet of the jet engine, and the other larger diameter ring is to be placed downstream. The diameters of these rings were carefully determined so that microphones could be placed as close to the jet plume as possible, yet without contaminations by turbulent flow from the jet nozzle. Two rows of 31 microphones each will be created and the microphones will be spaced at 0.077m. These two rows of microphones will then be rotated along the circular rings at every 5.6º over a 360º range. To validate the reconstructed acoustic pressures, benchmark pressures perpendicular to the jet flow direction will be taken as well. Acoustic pressures will then be reconstructed in the field perpendicular to the jet plume on these benchmark pressure locations to validate the HELS method. Once the HELS-based NAH technique is validated, the sound field over the measurement surface around the plume and field points will be reconstructed.

CHAPTER 2 - THE HELS METHOD

2.1 The HELS Algorithm

Assuming the homogeneity of the medium, the acoustic pressure field is governed by the linear and homogeneous wave equation (2.1), derived from the conservation of mass and Euler's equation.

$$\nabla^2 \hat{p}(\vec{x},t) - \frac{1}{c^2}\frac{\partial^2 \hat{p}(\vec{x},t)}{\partial t^2} = 0 \tag{2.1}$$

in which the operator ∇^2 is the laplacian sum of the second derivatives with respect to the three Cartesian coordinates, i.e., the divergence of the gradient, $\hat{p}(\vec{x},t)$ is the space and time dependent acoustic pressure and c is the speed of sound in the medium.

Taking the Fourier transform of the wave equation and assuming steady state conditions, one can obtain the reduced wave equation also known as the homogeneous Helmholtz equation. The homogeneity is characterized by the zero on the right hand side, which shows that there are no other sources in the exterior or the interior region.

$$\nabla^2 p(\vec{x},\omega) + k^2 p(\vec{x},\omega) = 0 \tag{2.2}$$

in which $p(\vec{x},\omega)$ represents the complex amplitude of the acoustic pressure and $k = \omega/c$ is the wave number. At the interface of surface of the vibrating object and the acoustic medium, $p(\vec{x},\omega)$ satisfies one of the three types or their combinations of boundary conditions.

1. Dirichlet Boundary Conditions in which the pressure is defined on the boundary

$$p(x_B) = g(x_B) \tag{2.3a}$$

2. Neumann Boundary Conditions in which normal velocity is defined on the boundary

$$\frac{\partial p(x_B)}{\partial n} = g(x_B) \tag{2.3b}$$

3. Mixed Boundary Conditions in which a relationship between pressure and normal velocity exists on the surface

$$a(x_B)\, p(x_B) + b(x_B) \frac{\partial p(x_B)}{\partial n} = g(x_B) \tag{2.3c}$$

The HELS method is based on the assumption that the radiated acoustic pressure from a vibrating object in an unbounded fluid medium is expressible in terms of an expansion of certain basis functions. In other words, the solution to the Helmholtz equation (2.2) subject to the boundary conditions (2.3) can be approximated as:

$$\hat{p}(\vec{x}, \omega) = \rho c \sum_{j=1}^{j} C_j \Psi_j(\vec{x}, \omega) \tag{2.4}$$

in which $\hat{p}(\vec{x}, \omega)$ is the complex amplitude of the acoustic pressure at any field point *x* and angular frequency ω, ρ and *c* are the density and speed of sound of the fluid medium, respectively, Ψ_j are the basis functions and can be expressed in any of the coordinate systems e.g., rectangular, spherical, elliptical, prolate, oblate etc. For brevity only the

spherical basis functions are used in the present study and they are expressed as expansion of spherical Hankel functions and the associated Legendre functions.

$$\psi_i(x,\omega) = \psi_{n,m}(r,\theta,\phi,\omega) = h_n(kr)P_{n,m}(\cos\theta)\times\begin{cases}\cos(m\phi)\\ \sin(m\phi)\end{cases} \tag{2.5}$$

in which $h_n(kr)$ and $P_{n,m}(\cos\theta)$ denote the spherical Hankel functions and Legendre functions, respectively, and $k=\omega/c$ is the acoustic wave number.

The coefficients C_j in Eq. (2.4) are determined by requiring the assumed-form solution to satisfy the boundary condition $\hat{p}(x_m,\omega)$ at the measurement point x_m.

$$\rho c\sum_{j=0}^{j} C_j\Psi_{m,j}(x_m,\omega) = \hat{p}(x_m,\omega). \tag{2.6}$$

If an N-term expansion in Equation (2.6) is used, then the total number of acoustic modes $\Psi_{m,j}(x_m,\omega)$ is equal to $J=(N+1)^2$. Accordingly, there are J unknown coefficients C_j. To solve these unknowns, M measurements must be taken ($M\geq J$). Theoretically, if the measured acoustic pressures $\hat{p}(x_m,\omega)$ are exact, then the assumed form solution (2.7) converges to the true value as $J\to\infty$. In reality, however, this never happens because the measured quantities $\hat{p}(x_m,\omega)$ always contain errors due either to measurement uncertainties or to rapid decay of near field effects as it is not always possible to take measurements close to the surface. While the former can be reduced by taking more averages in the measurement, the latter is irreversible. To enhance the accuracy of reconstruction, the least squares method is utilized to eliminate the first-order errors

incurred during this process. This simple regularization technique to circumvent the ill-posed inverse problem is discussed in section 2.2.

In matrix form, Equation 2.6 can be written as follows

$$\hat{\mathbf{p}}(\vec{x};\omega) = \mathbf{\Psi}(\vec{x};\omega)\mathbf{C}(\omega) \tag{2.7}$$

The expansion coefficients can be solved by pre-multiplying $\mathbf{\Psi}^{\mathrm{H}}$

$$\mathbf{\Psi}(\vec{x};\omega)^{H}\hat{\mathbf{p}}(\vec{x};\omega) = \mathbf{\Psi}(\vec{x};\omega)^{H}\mathbf{\Psi}(\vec{x};\omega)\mathbf{C}(\omega) \tag{2.8}$$

in which the superscript H implies a conjugate transpose of the matrix. Note that ($\mathbf{\Psi}^{\mathrm{H}}\,\mathbf{\Psi}$) forms a square (normal) matrix. The expansion coefficients can be obtained by taking a pseudo inversion

$$\mathbf{C}(\omega) = \mathbf{\Psi}(\vec{x};\omega)^{\dagger}\hat{\mathbf{p}}(\vec{x};\omega) \tag{2.9}$$

in which the superscript † indicates a pseudo-inverse matrix

$$\mathbf{\Psi}(\vec{x};\omega)^{\dagger} = \left[\mathbf{\Psi}(\vec{x};\omega)^{H}\mathbf{\Psi}(\vec{x};\omega)\right]^{-1}\mathbf{\Psi}(\vec{x};\omega)^{H} \tag{2.10}$$

in which

$$\mathbf{\Psi}(\vec{x};\omega) = \begin{bmatrix} \Psi_1(\vec{x}_1;\omega) & \Psi_2(\vec{x}_1;\omega) & \cdots & \Psi_J(\vec{x}_1;\omega) \\ \Psi_1(\vec{x}_2;\omega) & \Psi_2(\vec{x}_2;\omega) & \cdots & \Psi_J(\vec{x}_2;\omega) \\ \vdots & \vdots & \ddots & \vdots \\ \Psi_1(\vec{x}_N;\omega) & \Psi_2(\vec{x}_N;\omega) & \cdots & \Psi_J(\vec{x}_N;\omega) \end{bmatrix} \quad \mathbf{C}(\omega) = \begin{Bmatrix} C_1(\omega) \\ C_2(\omega) \\ \vdots \\ C_J(\omega) \end{Bmatrix} \tag{2.11}$$

$$\boldsymbol{\Psi}(\vec{x};\omega)^H = \begin{bmatrix} \Psi_1(\vec{x}_1;\omega)^* & \Psi_1(\vec{x}_2;\omega)^* & \cdots & \Psi_1(\vec{x}_N;\omega)^* \\ \Psi_2(\vec{x}_1;\omega)^* & \Psi_2(\vec{x}_2;\omega)^* & \cdots & \Psi_2(\vec{x}_N;\omega)^* \\ \vdots & \vdots & \ddots & \vdots \\ \Psi_J(\vec{x}_1;\omega)^* & \Psi_J(\vec{x}_2;\omega)^* & \cdots & \Psi_J(\vec{x}_N;\omega)^* \end{bmatrix} \quad \hat{\mathbf{p}}(\vec{x};\omega) = \begin{Bmatrix} \hat{p}(\vec{x}_1;\omega) \\ \hat{p}(\vec{x}_2;\omega) \\ \vdots \\ \hat{p}(\vec{x}_N;\omega) \end{Bmatrix} \tag{2.12}$$

Now we substitute expansion coefficients into the HELS formulation evaluated at the measurement points $\vec{x}_m \in \Gamma$, m = 1 to M,

$$\hat{\mathbf{p}}(\vec{x}_m;\omega) = \mathbf{G}(\vec{x}_m|\vec{x};\omega)\hat{\mathbf{p}}(\vec{x};\omega) \tag{2.13}$$

in which $\hat{\mathbf{p}}(\vec{x}_m;\omega)$ is a column vector containing measured data, $\hat{\mathbf{p}}(\vec{x};\omega)$ is a column vector of unknown acoustic pressures, and $\mathbf{G}(\vec{x}_m|\vec{x};\omega)$ is the transfer matrix that correlates the measured acoustic pressure to the acoustic pressure at any location, including a source surface.

The acoustic pressure at any field point $\vec{x}$ is given by

$$\hat{\mathbf{p}}(\vec{x};\omega) = \mathbf{G}(\vec{x}_m|\vec{x};\omega)^\dagger \hat{\mathbf{p}}(\vec{x}_m;\omega) \tag{2.14}$$

Recall that

$$\hat{\mathbf{p}}(\vec{x}_m;\omega) = \boldsymbol{\Psi}(\vec{x}_m;\omega)\boldsymbol{\Psi}(\vec{x};\omega)^H \hat{\mathbf{p}}(\vec{x};\omega) = \boldsymbol{\Psi}(\vec{x}_m;\omega)\mathbf{C}(\omega) \tag{2.15}$$

As mentioned previously, in solving for expansion coefficients $\mathbf{C}(\omega)$, we need to take more measurement points than the expansion terms, namely, $M > J$. Measurements of acoustic pressure $\hat{\mathbf{p}}(\vec{x}_m;\omega)$ can be taken on a conformal surface Γ enclosing the source at

close range. The acoustic pressures $\hat{\mathbf{p}}(\vec{x}_m;\omega)$ on the source surface can be obtained in HELS by setting $\vec{x} = \vec{x}_n$, n = 1 to N

$$\hat{\mathbf{p}}(\vec{x}_n;\omega) = \mathbf{G}(\vec{x}_m|\vec{x}_n;\omega)^{\dagger}\,\hat{\mathbf{p}}(\vec{x}_m;\omega) \tag{2.16}$$

where $\mathbf{G}(\vec{x}_m|\vec{x}_n;\omega)^{\dagger}$ is a pseudo inversion of $\mathbf{G}(\vec{x}_m|\vec{x}_n;\omega)$ given by

$$\mathbf{G}(\vec{x}_m|\vec{x}_n;\omega) = \mathbf{\Psi}(\vec{x}_m;\omega)\,\mathbf{\Psi}(\vec{x}_n;\omega)^{\dagger} \tag{2.17}$$

The formulations derived above are valid for the external region only. These can be extended to reconstruction of the acoustic pressure fields in the interior region.

The Hankel function $h_n(kr)$ in Eq. (2.5) corresponds to outgoing waves, appropriate for reconstruction of acoustic pressure fields in the exterior region. Such a function is unbounded at r = 0 and cannot be used to reconstruct the acoustic pressure fields in an interior region.

We shall try to define the Hankel function and make it more receptive to reconstruction in the interior region. Mathematically, the Hankel function $h_n(kr)$ can be written as given by Morse and Ingard (1986):

$$h_n(kr) = j_n(kr) + i\,y_n(kr) \tag{2.18}$$

in which j_n and y_n are the spherical Bessel and spherical Neumann functions of order n, respectively. Rayess[12] has studied the behavior of Bessel and Neumann functions extensively. Now, j_n is finite at r = 0, while y_n is not[6, 10]. Noting that the pressure must be

finite at the origin, because the homogeneous differential equation is valid there, the above relation for the Hankel function is ill-suited for reconstruction in the interior region. Thus, due to this physical reasoning only the spherical Bessel functions are retained in Eq. (2.5) to reconstruct the acoustic pressure fields in the interior. Hence, for an interior problem the basis functions are expressed as:

$$\psi_i(x,\omega) = \psi_{n,m}(r,\theta,\phi,\omega) = j_n(kr)P_{n,m}(\cos\theta) \times \begin{cases} \cos(m\phi) \\ \sin(m\phi) \end{cases} \tag{2.19}$$

With the basis functions given by relation (2.19) the relation (2.4) can now be used to find the coefficients and, therefore, the entire acoustic field in the interior of the cavity.

2.2 Optimum Number of Expansion Terms

As discussed earlier, the acquired acoustic pressures are taken as the input to the HELS formulation. Because of the loss of near-field information and other measurement contaminants, these acquired acoustic pressures are not exact. Hence, this inverse problem is mathematically ill-posed. These restrictions always remain because in engineering applications the working environment usually hinders the data acquisition at very close distances to a complex vibrating structure. Consequently, it is not realistic to obtain accurate reconstruction before the inherent ill-posedness difficulty is solved mathematically.

As discussed in the preceding sections, the HELS formulation utilizes the principle of superposition of spheroidal wave functions to reconstruct the radiated acoustic pressure fields. Theoretically, the larger the number of expansion terms, the

more accurate the reconstructed acoustic pressure should be. This is true only if the measured data are accurate; for this investigation, though, because of loss of the near-field information and measurement errors, the measured data cannot be assumed to be accurate. Thus, in this case, an increase in number of expansion terms may not necessarily yield an accurate reconstruction. Moreover, the optimal number of expansion terms used in the HELS formulation is unknown a priori, making it an open-ended problem.

To alleviate this problem, the following methodology is employed. To determine the optimal number of expansion terms, the acoustic pressures are reconstructed at the same locations where the measurements are taken for a particular number of expansion terms. These reconstructed pressures are then compared with the measured acoustic pressure at the same locations and the sum of mean squared deviations of the reconstructed pressures from the benchmark results is calculated using the relation:

$$\left\|L\right\|^2 = \sum_i \frac{\left|P_{m,i} - P_{r,i}\right|^2}{\left|P_{b,i}\right|^2} \tag{2.20}$$

in which $P_{m,i}$ is the measured acoustic pressure at point I on the hologram surface, and $P_{r,i}$ is the reconstructed pressure at point I, and $\left\|L\right\|^2$ is the sum of mean squared errors over the entire surface.

This process is iterated for different expansion terms, say N=1, 2, 3…. and so forth, and the corresponding mean squared deviations are calculated. These iterations are

performed until the number of expansion terms is less than or equal to the total number of measurements to satisfy the conditions for equation (2.3) to hold true. The reconstruction iteration yielding the minimum mean squared deviation from the benchmark is taken as the absolute result and the corresponding expansion terms as optimum. As a graphical depiction of the above method, Figure 2.1 shows the variation of the mean squared error with the increase in number of expansion terms for the HELS formulation for a typical test experiment.

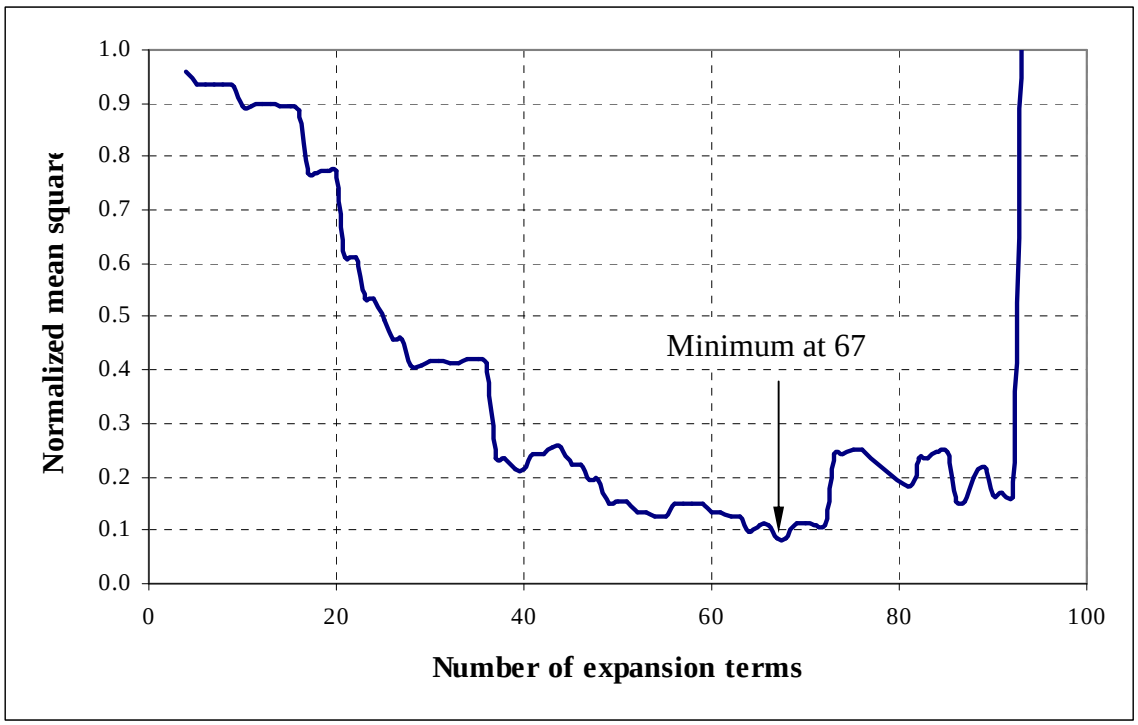

Figure 2.1: Variation of mean squared error and prediction of the optimum number of terms for a typical test case for a single frequency.

2.3 Reconstructing Normal Surface Velocity and Intensity

Using Euler's equation, we can reconstruct the particle velocity at any location, including the source surface:

$$i\omega\rho_0\vec{\hat{v}} = \nabla\hat{p} \quad \rightarrow \quad \vec{\hat{v}} = \frac{1}{i\omega\rho_0}\nabla\hat{p} \tag{2.21}$$

$$\vec{\hat{\mathbf{v}}}(\vec{x};\omega) = \frac{1}{i\omega\rho_0}\nabla\mathbf{G}(\vec{x}_m|\vec{x};\omega)^{\dagger}\hat{\mathbf{p}}(\vec{x}_m;\omega) \tag{2.22}$$

Once the acoustic pressure and particle velocity are determined, the time-averaged acoustic intensity can the be calculated

$$\vec{\hat{\mathbf{I}}}_{av}(\vec{x},\omega) = \frac{1}{2}\mathrm{Re}\left[\hat{\mathbf{p}}(\vec{x},\omega)\vec{\hat{\mathbf{v}}}(\vec{x},\omega)^{*}\right] \tag{2.23}$$

Thus, the entire acoustic field is determined.

2.4 Optimizing Test Results

In practical application a number of parameters can affect the accuracy and validity of reconstruction results. These parameters are discussed as follows.

2.4.1 Number of Field Acoustic Pressure Measurements

Theoretically, for a given *ka*, the number of expansions in the radial direction are taken as *n*=*ka* and the total expansion terms as:

$$J = (n+1)^2 = (ka+1)^2 \tag{2.24}$$

in which $ka = \frac{2\pi f}{c}a$, and *a* is the dimension of the vibrating source.

As an example, at 200 Hz and the source size of a = 2 m, ka = 7.3, the number of total expansion terms is $J \cong 69$ terms. The number of field pressure measurements is then

given as $M = 1.4J \cong 97$. This methodology had been used to estimate the number of microphones required to acquire field acoustic pressures for numerical and experimental validations. But this estimation does not usually provide the desired reconstruction resolution to rebuild the surface acoustic field, and leads to aliasing. The impact of selection of number of measurement points and other parameters affecting the accuracy of reconstruction have been studied at length through numerical simulations[43, 44]. Another method is to determine the number measurement points based on the source surface area and the wavelength of the highest vibration mode of interest instead of the highest frequency of interest as in (2.24)[66, 67]:

$$M = \frac{A}{(\Delta/2)^2} \tag{2.25}$$

in which M is the total number of measurement points, A is the area of the source surface, and Δ is the wavelength of the highest vibration mode of interest or spatial resolution. Over the years spent developing and testing the HELS code for various sources, we have found that one needs a minimum of 44 measurements, regardless of how small a structure is. This limit on the minimum number of measurements is set to ensure that at least the first few of the expansion terms are used in the reconstruction.

2.4.2 Measurement Resolution

In order to reconstruct the acoustic field with the desired surface spatial resolution, the microphones should be spaced at least one half of this desired resolution:

$$M_\delta \leq \frac{\Delta}{2} \tag{2.25}$$

in which M_δ is the microphone spacing and Δ is wavelength of the highest vibration mode of interest or the desired spatial resolution

2.4.3 Measurement Standoff Distance

Ideally, one should try to measure as close to the source surface as one can to capture the maximum possible evanescent or high wave number vibro-acoustic components that decay exponentially as they propagate away from the source surface. Evanescent waves contain all the details of structural vibrations and are extremely important in reconstruction of the surface normal vibration response. Theoretically, if all evanescent waves are captured, the spatial resolution in reconstruction can be infinitely high. Evanescent waves are not easy to capture because they fluctuate at a very high rate and their amplitudes tend to be small, often at the level of background noise or lower. However, in projecting the acoustic radiation from a source (beyond one wavelength distance), the effects of the evanescent waves can be ignored.

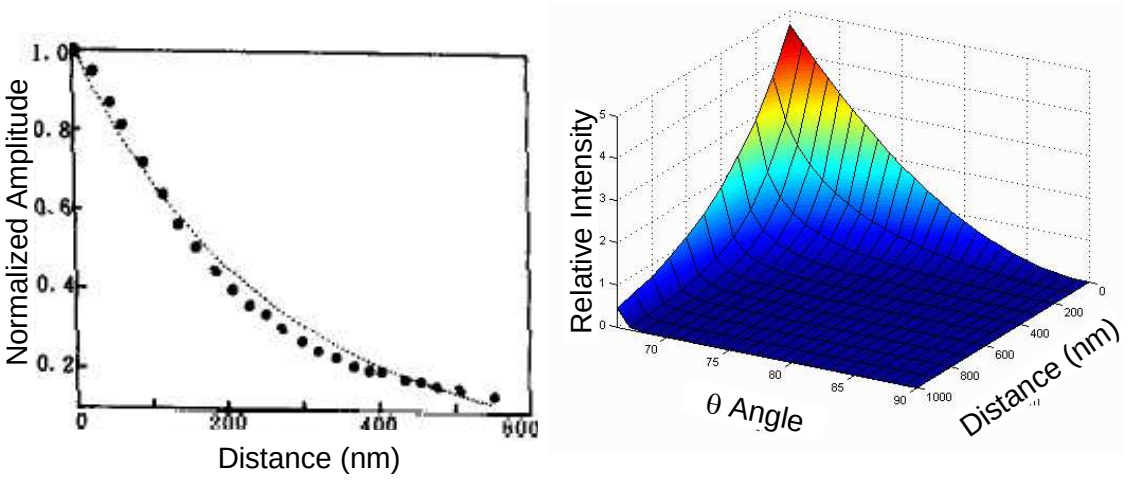

(a) **(b)**

Figure 2.2: (a) Typical evanescent wave decay rate in 2D **(b)** Typical evanescent wave decay rate in 3D.

But this is not always possible in the real-world test environments where microphones cannot get close to the source surface for acoustic pressure measurement. An example is shown in figure 2.1, where the engine test cell setup is so complex that a planar array cannot get close enough to the engine surface to measure enough of the evanescent components necessary for reconstructing surface acoustic quantities.

Figure 2.3: A typical engine test cell acoustic holography test setup with a planar microphone array.

When the S/N ratio is high (at least > 10 dB) and signal level is stable, the measurement distance can be pushed out to 1/8 of the shortest wavelength of interest so that at least 50% of the evanescent waves may be captured[67].

$$d < \frac{\lambda}{8} \tag{2.26}$$

in which d is the standoff distance and λ is the wavelength of the highest vibration mode of interest or the desired spatial resolution. In practice, it is always a good idea to use a

conformal microphone array and keep measurement distance d as close to the target source surface as possible, regardless of the value of λ .

2.4.4 Signal-to-Noise (S/N) Ratio

To obtain an accurate reconstruction of an acoustic field, the S/N ratio must be at least larger than 10dB. There are many factors that can effectively lower the S/N ratio. For example, background noise and fluctuations in signal level can drastically reduce the S/N ratio. Since the amplitudes of evanescent waves decrease with frequencies, the S/N ratio requirement should be higher at high frequencies than that at low frequencies in order to ensure a satisfactory reconstruction in the entire frequency range. Note that evanescent waves are critical in the reconstruction of both acoustic pressure and particle velocity, especially at higher frequencies.

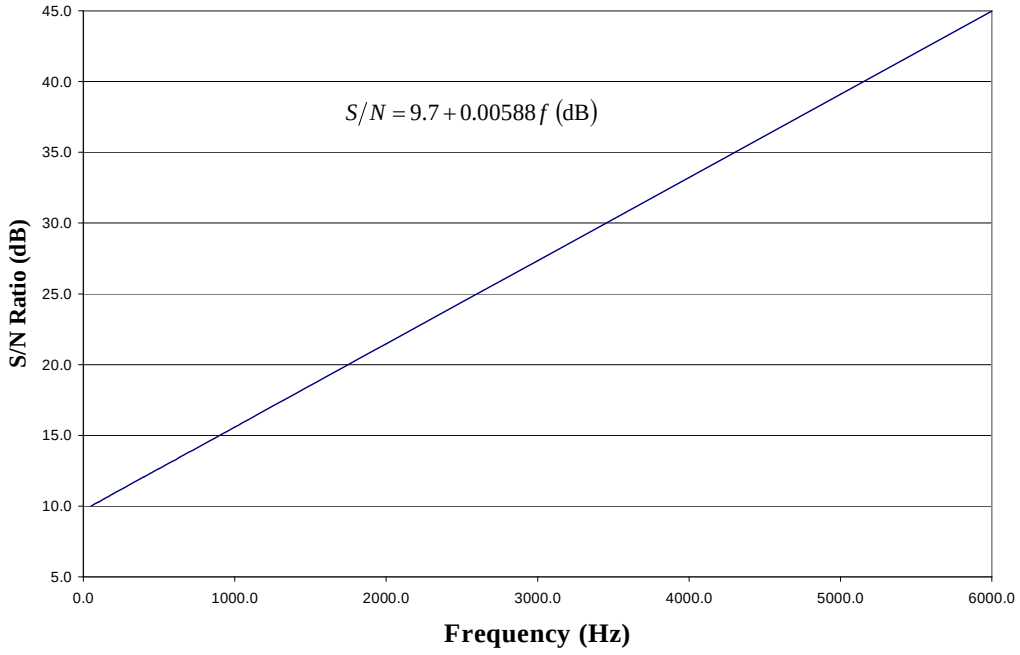

Figure 2.4: S/N Ratio requirement for frequencies of interest. The higher the frequency the higher the signal to noise ratio should be.

Apart from the background noise, the fluctuations in signal level itself can affect the S/N ratio. In practice, the signal level is not very stable and the sound pressure is fluctuating, which will cause measurement errors. These measurement errors will effectively reduce the S/N ratio. As an example, consider a case in which measurements are taken inside an anechoic chamber and the ambient noise level is 10 dB, whereas the signal level is 80 dB for frequencies above 200Hz. So the S/N ratio is 70 dB. Suppose that measurements are averaged over 6 seconds, and the measured level is 80.1 dB rather than 80 dB. This fluctuation is equivalent to the scenario in which an 80 dB sound is superimposed by background noise of 63.7 dB because

$$L_{background} = 10\log\left(10^{\frac{L_{total}}{10}} - 10^{\frac{L_{true}}{10}}\right) = 10\log\left(10^{\frac{80.1}{10}} - 10^{\frac{80}{10}}\right) = 63.7\ \text{dB} \qquad (2.26)$$

Therefore, S/N = 80 – 63.7 = 16.3 dB rather than 70 dB.

Setting the measurement distance to be as small as possible and taking a long time average (for example, 30 to 60 sec) can improve the S/N ratio for stationary cases.

2.4.5 Test Object Aspect Ratio

As mentioned earlier, for all real-world applications, the HELS method uses an expansion of spherical harmonic functions to estimate the acoustic field around an object. As such, the biggest restriction of the HELS based NAH is the aspect ratio, which is defined as the ratio of overall width to length to thickness.

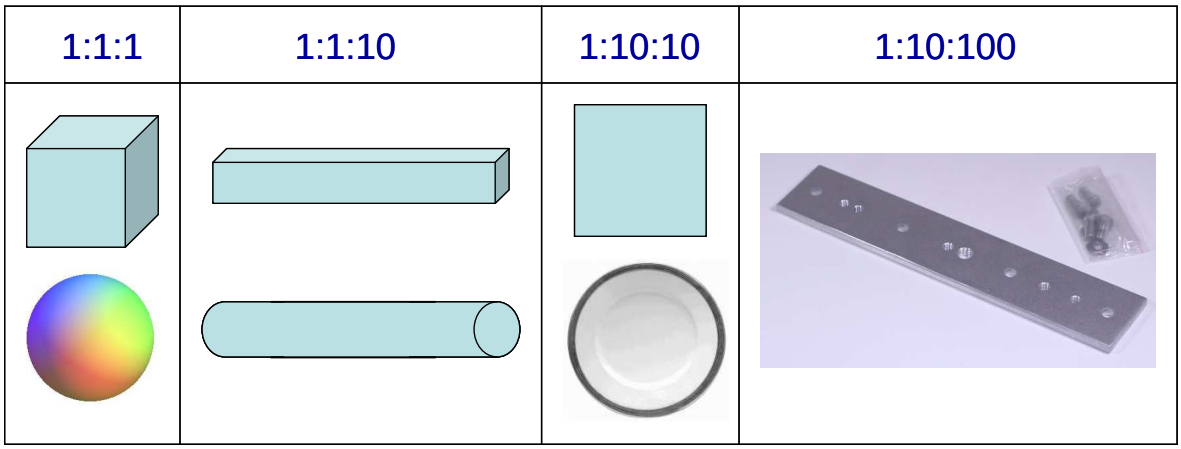

Figure 2.5: An aspect ratio of 1:1:1 implies that the width, length, and thickness of an object are equal, namely, a cubic box. Similarly, an aspect ratio of 1:1:10 is a long column with a square cross section, that of 1:10:10 is a thin, square plate, and that of 1:10:100 is a thin, flat, and long plate.

In practice, HELS is ideal for an object of aspect ratio close to 1:1:1. If the measurement surface is conformal, measurement distance is small, and signal to noise (S/N) ratio is high, the accuracy of reconstruction of an acoustic field in the entire 3D space including the 3D source surface using HELS is guaranteed for an aspect ratio up to 1:1:1.4 or 1:1.4:1.4. The accuracy of reconstruction will be reduced, but still acceptable, as aspect ratio increases to 1:1:2 or 1:2:2. The accuracy of reconstruction will deteriorate as the aspect ratio increases to 1:1:4 or 1:4:4.

When the aspect ratio is larger than 1:1:4, the accuracy of reconstruction using HELS method will be poor. This is because HELS uses an expansion of the spherical wave functions with respect to a single point, as mentioned previously.

2.4.6 Exterior or Interior Test

The key factors to consider in deciding sound radiation as an exterior or interior problem are whether a region is bounded, and how much sound reflection is in the field

of interest. Most exterior and interior problems are clearly recognizable. There are cases that require careful attention however. Some typical exterior and interior test scenarios are shown in figures 2.6 and 2.7.

Figure 2.6: A typical unbounded or free field exterior test setup.

Figure 2.7: A typical bounded or non-free field exterior test setup.

Figure 2.6 shows a typical exterior test setup in a fully anechoic chamber or free field and figure 2.7 shows a typical exterior test setup in a bounded or non-free field environment.

Note that diagnosis inside a fully anechoic chamber is much easier to handle than that in a non-anechoic environment with a considerable amount of reflections.

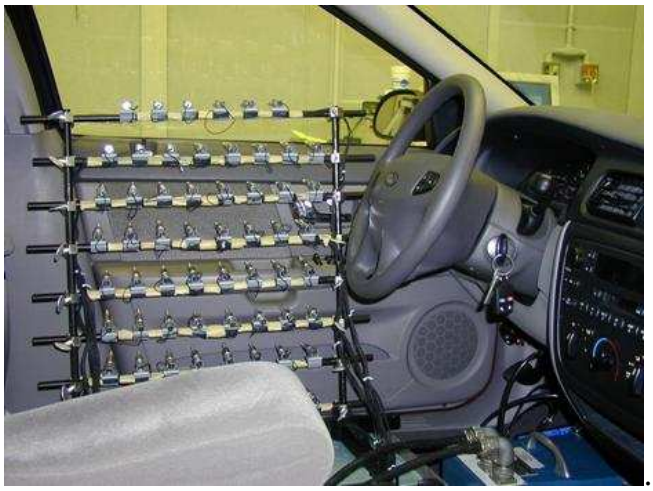

Figure 2.8: A typical completely enclosed interior test setup.

Figure 2.9: A typical partially enclosed interior test setup.

A completely enclosed region in figure 2.8 signifies a true interior problem, whereas a partially enclosed region in figure 2.9 is not a true interior problem. Figure 2.10 depicts the ideal microphone measurement schemes for exterior and interior cases.

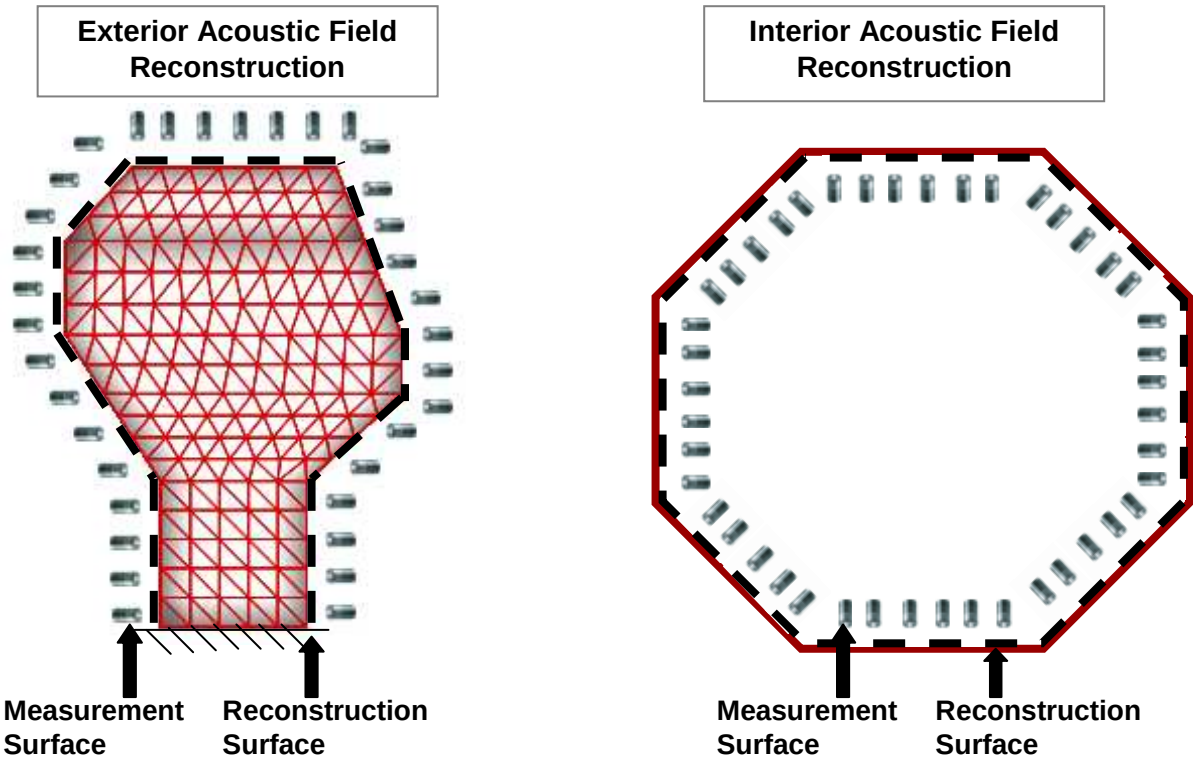

Figure 2.10: Ideal microphone measurement schemes for exterior and interior tests.

Note that it is not possible to get satisfactory reconstruction of the acoustic quantities in the entire 3D space including 3D source surfaces by using a quick look approach. It is not realistic to expect satisfactory reconstruction of acoustic quantities in the entire 3D space and on 3D source surface for an exterior problem, when the exterior region is a non-free field or measurements are taken over a portion of the source surface (Figure 2.11). Therefore, such an attempt should be discouraged.

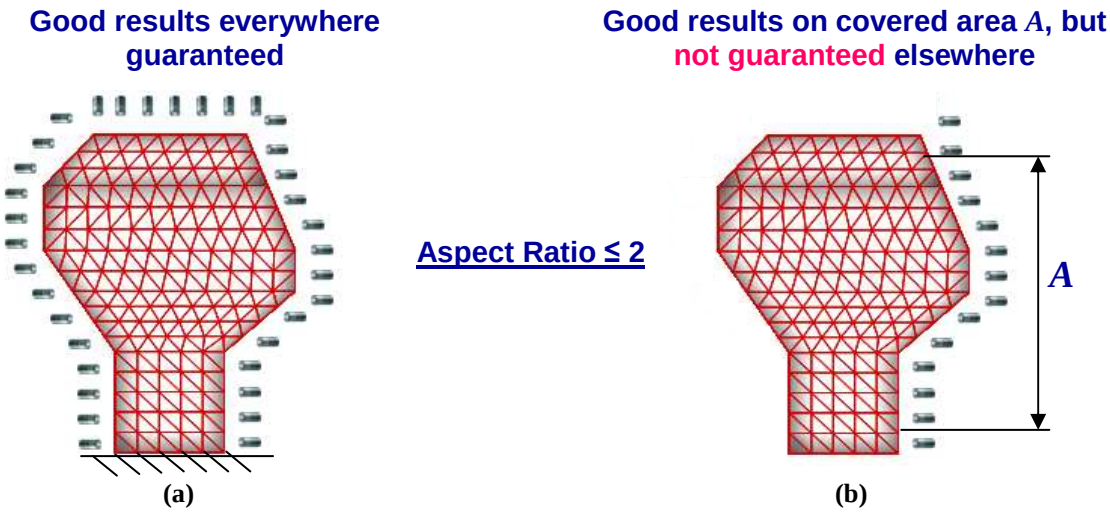

Figure 2.11: Measurement schemes in the exterior region. **(a)** Guarantees results in the complete 3D free-field around the object **(b)** good results can be achieved on the partially covered area A but nowhere else no matter which conditions exist, free field or non-free field.

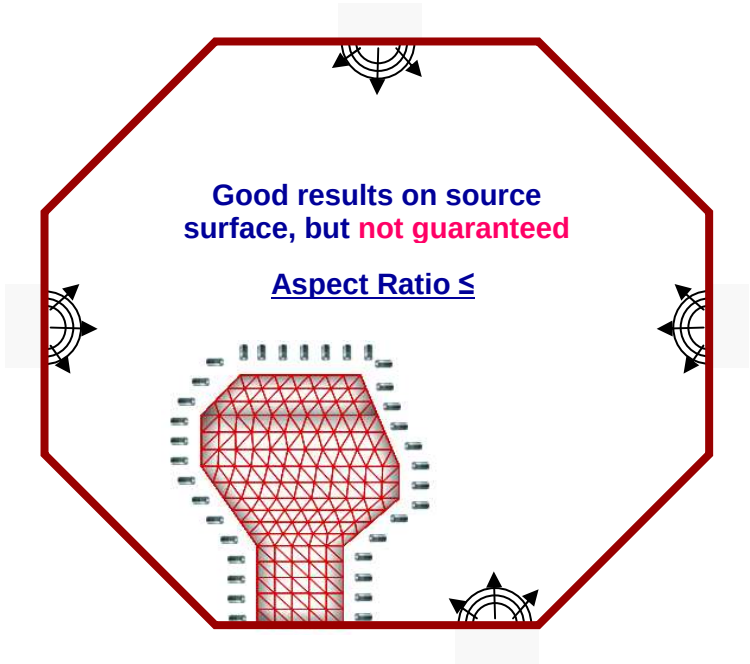

Figure 2.12: Good results can be achieved only on the source surface in a bounded region.

If reconstruction is done inside a large room with sound reflections from the ground and walls, the test setup is equivalent to an interior problem with the

measurements taken on partial surfaces only. As a result, the accuracy of reconstruction of the acoustic quantities on a source surface is good, but the accuracy in a 3D space is not guaranteed. Figure 2.12 depicts this particular scenario.

When tests are conducted in confined space, the reflecting surfaces behave like image sources. The sound pressure in confined space will consist of the direct sound from the source (ray 1) and those reflected from walls (rays 2 to 4). This is equivalent to the case in which a source and its three images lie in free space. The sound pressure consists of the contributions from all sources. Refer to figure 2.13, below.

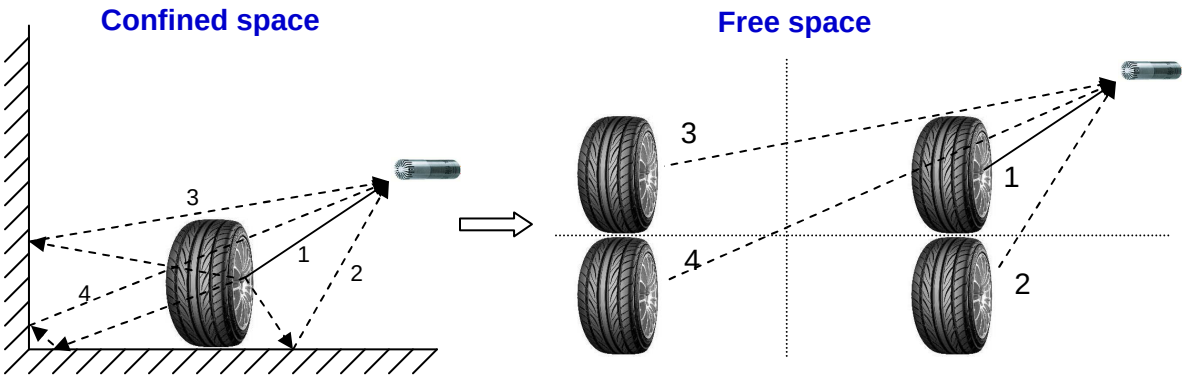

Figure 2.13: Equivalent free field sources for a source in confined space.

Hence, if measurements are taken around the source only in confined space, it is as if one is considering only the source and neglecting contributions from its images in free space. This is why the predicted results in 3D space may be erroneous when the input data are collected around the source only in the presence of reflecting surfaces. The errors may differ, however, depending on the locations. The closer it is to the source, the better the results are. The farther away the test environment is from any reflecting surfaces, the better the results are.

As discussed previously, reconstruction of acoustic quantities in the entire 3D space including 3D source surfaces can be acquired for an exterior problem inside a fully anechoic chamber, if measurements are taken over the entire surface of a target source. Similarly, reconstruction of acoustic quantities in the entire 3D space including 3D interior surfaces can be acquired for an interior problem, when the region is completely enclosed and measurements are taken over the entire interior surface (refer to Figure 2.14).

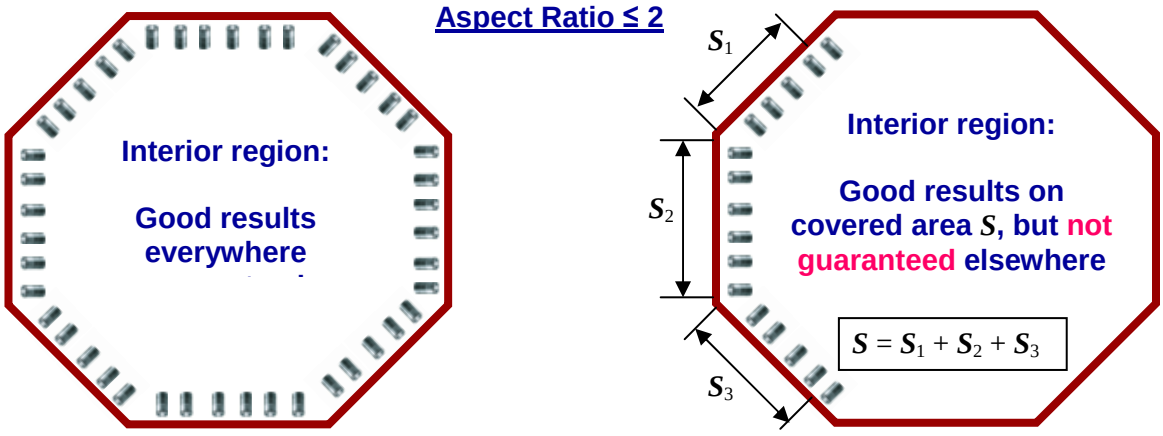

Figure 2.14: Measurement schemes in the interior region. **(a)** Guarantees results in the complete 3D field inside the object **(b)** good results can be achieved on the partial covered area *S* but nowhere else.

2.4.7 Coordinate System Origin

Since the HELS method uses expansion of spherical harmonic functions, the accuracy of reconstruction of 3D acoustic field depends on where the origin of the coordinate system is selected. The origin of the coordinate system for an interior case, such as that of a car cabin, is always set at the geometric center of the interior cavity (Figure 2.15), regardless of whether complete surface area is measured or partial.

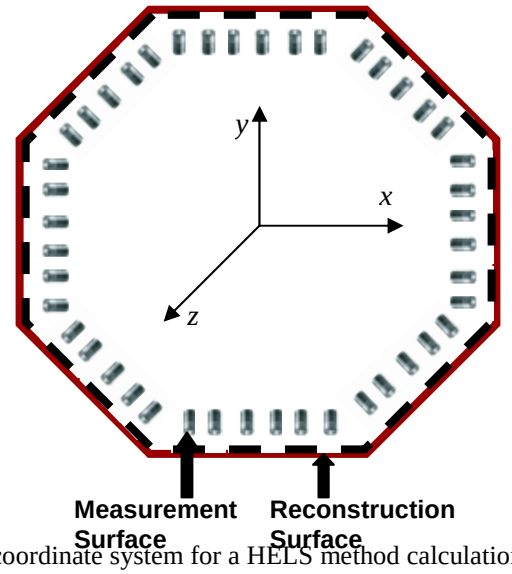

Figure 2.15: Origin of the coordinate system for a HELS method calculation in the interior region is the geometric center of the cavity.

In a similar fashion, the origin of the coordinate system is set at the geometric center of a 3D blunt object when reconstructing in the exterior region (Figure 2.16).

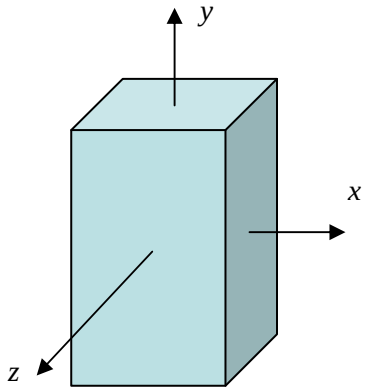

Figure 2.16: Origin of the coordinate system for a HELS method calculation in the interior region is the geometric center of the cavity.

A special case is a plate like surface (Figure 2.17) with an aspect ratio $T : H : L$, where $T << H$, $T << L$, and $H : L \leq 1{:}2$. In this case, the center of origin should be placed behind the plate, opposite to the measurement array, where z_0 is given by

$$z_0 = 0.5\sqrt{H^2 + L^2}$$

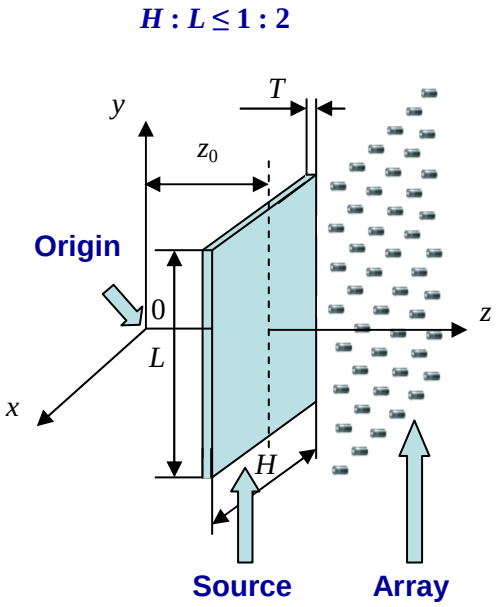

Figure 2.17: Origin of the coordinate system for a HELS method calculation for a plate like structure.

Note that the reconstructed acoustic quantities in this case will be good on one side of the surface of this structure, but not good elsewhere in the entire 3D space. If acoustic quantities on the other side of this structure are desired, the same reconstruction process should be repeated with the origin of coordinate system placed on the opposite side of the structure.

2.4.8 Measurement Aperture

For planar NAH, the measurement aperture should be four times as large as the source surface to ensure that sufficient information is captured. For example, for a plate of width W and length L, the measurement aperture should be at least $4 \times W \times L$. For the HELS method, however, the only restriction is for the measurement aperture to be at least the same size as the reconstruction surface. In order to further improve the accuracy at the

edges of the reconstruction surface, the measurement aperture must be one extra row and column larger than reconstruction surface (Figure 2.18).

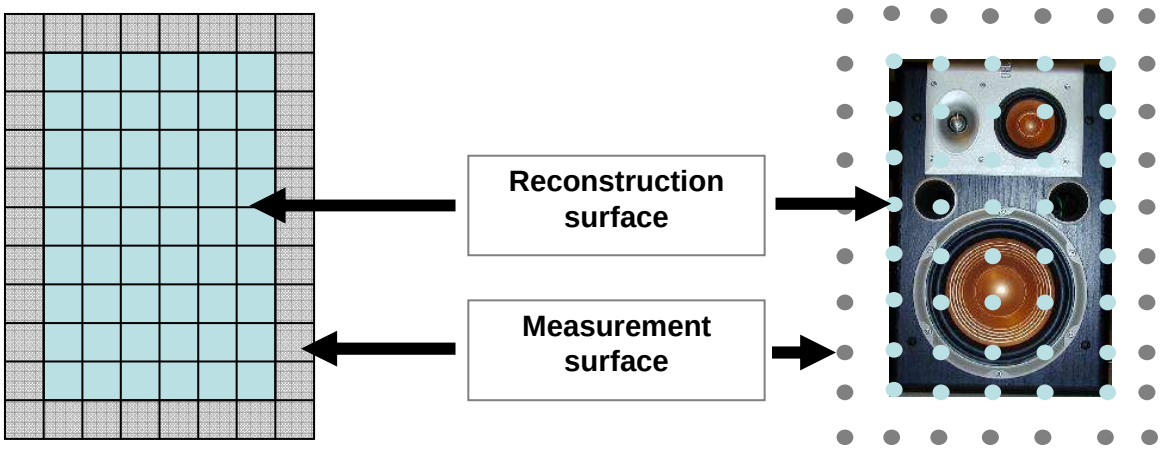

Figure 2.18: Origin of the coordinate system for a HELS method calculation for a plate like structure.

CHAPTER 3 – PROPOSED MODIFIED HELS METHOD FOR JET ENGINE NOISE VISUALIZATION

3.1 Identification and Significance of the Problem

The previous chapter discussed the HELS-based NAH technology that is has been widely used to visualize sources of noise and to diagnose a variety of sound and vibration problems in the automobile and appliance industries. This novel technology is applicable to interior and exterior regions as well as in free and confined spaces. The original HELS formulation is suitable for reconstructing sound radiation from a vibrating structure that is stationary and well defined in space. Such a scenario is completely different from aerodynamically generated sound such as that produced by turbulent flow ejected from a jet nozzle. Figure 3.1 illustrates the image of computer-simulated jet noise from a bypass nozzle[46].

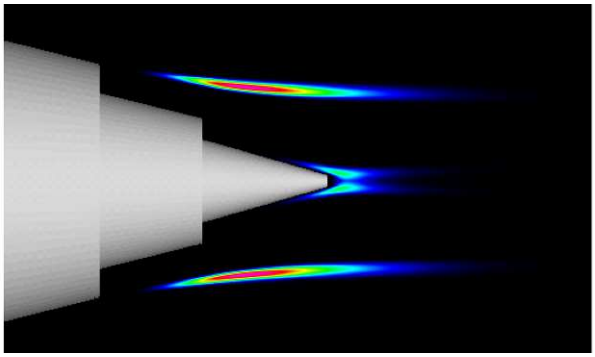

Figure 3.1: Noise source of a jet plume[46].

The inner core stream consists of a hot and high velocity gas stream passing through a jet engine combustor, whereas the outer fan stream consists of cooler and lower velocity air pulled into the engine via a fan. In this case the source locations and strengths are not fixed in space and change with the flow speed. The exact solution to such turbulent flow sound cannot be found, so the challenge is to develop an effective method

to approximate the resultant sound field. Such a method should be simple and easy to understand, so that numerical computations can be done in a timely fashion. Meanwhile, this method must be comprehensive enough to account for the major sound sources and their distributions in space.

Many modifications of the original acoustic analogy proposed by Lighthill[57] remain a major numerical tool for prediction of jet noise. Lighthill[57] showed that by exact rearrangement of the Navier Stokes equations, that the noise from a turbulent jet could be expressed as a distribution of quadrupole sources in the acoustic wave equation. The strength of these quadrupole sources depends primarily on the local fluctuating Reynolds stresses. These Reynold stresses are created by the turbulent eddies convected by the jet velocity. The motion of these eddies alters the radiated sound, an effect correctly accounted for by Ffowcs Williams[58]. The mean jet velocity has yet another influence and it refracts the sound[59,60] altering the propagation of sound from the sources to the far field. Lilley's approach[61] described this propagation through a specified mean flow velocity profile, which is a function of radius.

In comparison to the various technologies currently available, modified HELS provides a unique opportunity to confront this challenging issue. This chapter will examine the feasibility of creating a commercialization-worthy variation of the previously discussed HELS-based NAH technology to visualize acoustic characteristics of jet plumes from commercial transport engines.

The proposed technology signifies an extension of the HELS method that can account for contributions from different sound generation mechanisms such as

monopoles, dipoles, and quadrupoles, and enable one to distribute these virtual sources anywhere in space. The locations of the virtual sources can be optimized to best approximate a sound field produced by a target source. The reconstructed 3D sound field can be sliced and viewed from any angle or perspective to gain a good understanding of the sound source strengths and their distributions in space, as well as how sound sources travel in space and time.

In a preliminary test, this modified HELS-based nearfield acoustical holography was successfully applied to visualize the sound field produced by twin propeller aircraft (Chapter 4). Most importantly, it demonstrated the capability to separate contributions from the engine and propellers and to reveal the effect of sound reflection from the ground[45].

Modern propulsive supersonic jets produce exterior noise sources with a high amplitude noise field and complicated characteristics, which makes them very difficult to characterize. In particular, there are turbulent eddies that are moving through the supersonic jet at high speeds along the jet boundary. These turbulent eddies in the shear layer produce a directional and frequency dependent noise. The original HELS approach assumes a spherical source at the origin and computes the acoustic field based on spherical emission from this source. The modified HELS approach will help improve the source characterization as it is not dependent on a single source at the origin but a number of virtual sources throughout the space[56].

Research has shown that dominant source region within the aero-acoustic source region in supersonic jets appears to be located approximately 7-10 jet diameters

downstream from the nozzle exit. Beyond this length source strength gradually decays[62,63]. For subsonic jets, however, Koch et al.[64] have experimentally and numerically investigated the dominant source region and have found the location of the geometric far-field for subsonic jets. Their study has concluded that high-frequency noise appears to spread spherically from as close as 8 times the jet diameter, but that the extended nature of the low-frequency sources results in a geometrical near-field that extends as far as 50 times the jet diameter.

In this investigation we will take measurements around a subsonic commercial jet engine running at idle. Because of idle running conditions, it is expected that the jet engine itself contributes significant amount of noise to the acoustic field. Reference microphone measurements will be taken both near the engine and along the jet plume length in addition to the microphone array measurements around the jet plume. Dominant source region lengths for different frequency bands will be found by cross-correlating reference and array microphones. These correlating lengths will then be used for correct placement of virtual sources along the jet plume axis for implementing the modified HELS algorithm.

3.2 The Modified HELS Algorithm

The modified HELS method is based on superposition of distributed spherical wave that satisfies the Helmholtz equation and Sommerfeld radiation condition in a free field (refer Eq. 2.2). It can be rewritten as

$$\nabla^2 \hat{p} + k^2 \hat{p} = 0 \tag{3.1}$$

in which $\hat{p}$ is the complex amplitude of the acoustic pressure and $k = \omega / c$ is the acoustic wave number with ω being the angular frequency and c being the speed of sound in the fluid medium.

The modified HELS algorithms seek to approximate the acoustic pressure $\hat{p}$ at any location in terms of an expansion of lower order spherical wave functions with respect to a finite number of virtual sources distributed on a surface conformal to the target surface from the inside or on an axis of symmetry of the source object[56, 68].

$$\hat{p}(x,\omega) = \sum \left[C_n h_0^{(1)}(kr_n) + h_1^{(1)}(kr_n) \left\{ D_n Y_1^0(\theta_n, \phi_n) + E_n Y_1^{-1}(\theta_n, \phi_n) + F_n Y_1^1(\theta_n, \phi_n) \right\} \right] \quad (3.2)$$

in which $h_0^{(1)}(kr_n)$ and $h_1^{(1)}(kr_n)$ are the first kind of spherical Hankel functions of order 0 and 1, respectively, and $Y_1^0(\theta_n, \phi_n)$, $Y_1^{-1}(\theta_n, \phi_n)$, and $Y_1^1(\theta_n, \phi_n)$ are the spherical harmonics given by

$$h_0^{(1)}(kr_n) = -\frac{ie^{ikr_n}}{kr_n} \quad (3.2a)$$

$$h_1^{(1)}(kr_n) = -\frac{ie^{ikr_n}(i + kr_n)}{(kr_n)^2} \quad (3.2b)$$

$$Y_1^0(\theta_n, \phi_n) = \frac{1}{\sqrt{4\pi}} \cos\theta_n \quad (3.2c)$$

$$Y_1^{-1}(\theta_n, \phi_n) = e^{i\phi_n} \sqrt{\frac{3}{8\pi}} \sin\theta_n \quad (3.2d)$$

$$Y_1^1(\theta_n,\phi_n) = -e^{i\phi_n}\sqrt{\frac{3}{8\pi}}\sin\theta_n \tag{3.2e}$$

Comparing Eq. 3.2 to 2.4, shows that proposed modified HELS method spreads an expansion with respect to several points, called virtual sources in this investigation, rather than a single point as the original HELS formulation. This gives the modified HELS method certain special advantages in reconstructing acoustic quantities on an elongated body when virtual sources are distributed along the axis of elongation of the body, or in this investigation, along the axis of a jet plume. Another advantage is reconstructing acoustic quantities over an arbitrary surface by distributing virtual sources over conformal surface from the inside.

Note that the expansion functions in Eq. 3.2 satisfy the Helmholtz Equation 3.1. Like HELS based NAH methodology, the coefficients $C = \{...,C_n,D_n,E_n,F_n,...\}^T$ in Eq. 3.2 are obtained by using the assumed form solution with measured acoustic pressures in the field. The errors are minimized by using the least-square error between the approximated solution $\hat{p}$ and the measured acoustic pressure $\hat{p}_f$ similar to the traditional HELS method. In matrix form

$$C = \arg\min\left\|W_f(\Phi_f\xi - \hat{p}_f)\right\|_2^2 \tag{3.3}$$

in which Φ_f is a matrix that contains $h_0^{(1)}(kr_n)$, $h_1^{(1)}(kr_n)$, $Y_1^0(\theta_n,\phi_n)$, $Y_1^{-1}(\theta_n,\phi_n)$, and $Y_1^1(\theta_n,\phi_n)$,

$$\Phi_f = \begin{bmatrix} \cdots & \cdots & \cdots & \cdots & \\ \cdots\ h_0^{(1)}(kr_n) & h_1^{(1)}(kr_n)Y_1^0(\theta_n,\phi_n) & h_1^{(1)}(kr_n)Y_1^{-1}(\theta_n,\phi_n) & h_1^{(1)}(kr_n)Y_1^1(\theta_n,\phi_n) & \cdots \\ \cdots & \cdots & \cdots & \cdots & \end{bmatrix} \quad (3.3a)$$

$$C = \{\ldots, C_n, D_n, E_n, F_{n,}\ldots\}^T_{4N\times 1} \quad (3.3b)$$

$$\hat{p}_f = \{\ldots, \hat{p}(r_m,\theta_m,\phi_m,\omega),\ldots\}^T_{M\times 1} \quad (3.3c)$$

in which r_m, θ_m, ϕ_m, m=1 to M, represents spherical coordinates of points on the field measurement surface. M is the number of measurements taken on this measurement surface and M≥4N, and W_f is an M×M nonsingular diagonal weight matrix whose elements are determined by quadrature formula and the mesh on field measurement surface. If enough measurements are not taken, the resultant matrix may be ill-conditioned. A simple and alternate solution for a case that does not satisfy the M≥4N guideline is to use a simplified expansion 3.2 that only contains $h_0^{(1)}(kr_n)$, $h_1^{(1)}(kr_n)$, and $Y_1^0(\theta_n,\phi_n)$. This is equivalent to a) an approximation of the Helmholtz integral theory and b) expressing the acoustic pressure in terms of superposition of monopoles and normal component of dipoles only.

$$\hat{p}(x,\omega) = \sum\left[C_n h_0^{(1)}(kr_n) + D_n h_1^{(1)}(kr_n)Y_1^0(\theta_n,\phi_n)\right] \quad (3.4)$$

in which C_n and D_n can be solved by minimizing the least-square errors between an approximated solution $\hat{p}$ and the measured field acoustic pressure $\hat{p}_f$, which is

expressible in a matrix form Eq. 3.3, and Φ_f is a matrix containing $h_0^{(1)}(kr_n)$, $h_1^{(1)}(kr_n)$, and $Y_1^0(\theta_n,\phi_n)$,

$$\Phi_f = \begin{bmatrix} & \cdots & \cdots & \\ \cdots & h_0^{(1)}(kr_n) & h_1^{(1)}(kr_n)Y_1^0(\theta_n,\phi_n) & \cdots \\ & \cdots & \cdots & \cdots \end{bmatrix} \tag{3.4a}$$

$$C = \{\ldots, C_n, D_n, \ldots\}^T_{2N\times 1} \tag{3.4b}$$

The advantage of this approach is that we only need to take half the measurements. Alternatively, using the same number of measurement points M, we can now deploy twice as many virtual sources as before. For the jet noise test we will be taking nearly 1000 measurements around the jet plume. This should give us 250 virtual sources that we can deploy along the axis of the jet plume, and we can use the unmodified form of Eq. 3.3 with $h_0^{(1)}(kr_n)$, $h_1^{(1)}(kr_n)$, $Y_1^0(\theta_n,\phi_n)$, $Y_1^{-1}(\theta_n,\phi_n)$, and $Y_1^1(\theta_n,\phi_n)$.

CHAPTER 4 - RELATED WORK

Numerous experiments have been conducted using the HELS-based technologies for many complex noise and vibration problems. As an example, we will discuss examples of visualizing automobile brake squeals using the traditional HELS method and reconstruction of acoustic radiation from a twin propeller aircraft.

4.1 Brake Squeal Noise Visualization

This test was conducted in a small chamber (Figure 4.1) and the brake assembly was driven by a shaft at a constant speed. To capture as much information about the brake squeals as possible, an array of 48 microphones was built. This array was conformal to the contour of a disk brake assembly, so the standoff distances were uniform (see Figure 4.2). The reference microphone was placed at the caliper.

Figure 4.1: Test chamber for visualizing brake squeals.

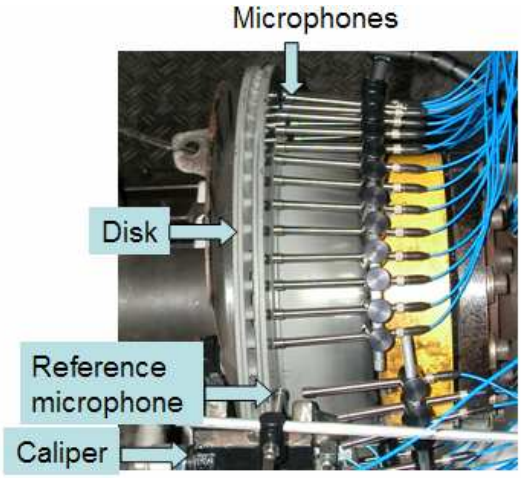

Figure 4.2: Close-up view of the test setup.

Figure 4.3 depicts six seconds of the captured squeals, which were complex and continuous. The corresponding spectra are plotted in Figure 4.4, which indicates that squeals occurred at many frequencies.

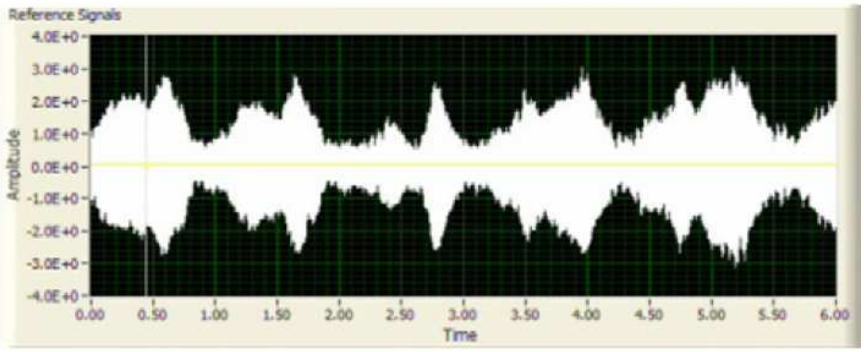

Figure 4.3: Squeal signals captured in six seconds.

Figure 4.4: Squeal spectra from 0 to 13.5kHz.

For brevity, the comparison of reconstructed and measured acoustic pressures at 2649Hz (see Figure 4.5) is demonstrated. Excellent agreements were obtained in all cases.

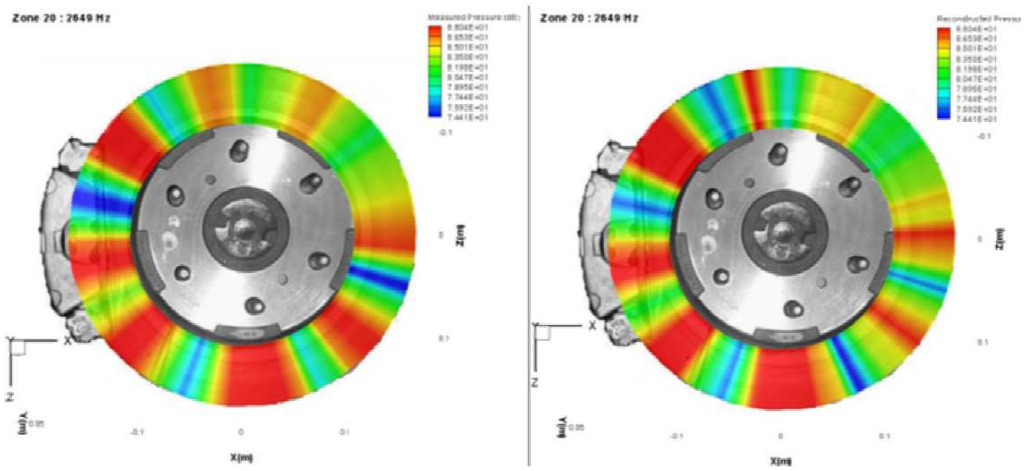

(a) **(b)**

Figure 4.5: Comparison the acoustic pressures at 2649Hz. (a): Measured; (b) Reconstructed.

To demonstrate the capability of displaying the frequency-space and space-time diagrams in the proposed project, we reconstruct the acoustic quantities for the brake squeal example in real time and plot the space-time diagrams of any acoustic quantities as needed. Also, we can take Fourier transforms of these quantities to create frequency-space diagrams to identify sound source frequency dependent spatial distributions.

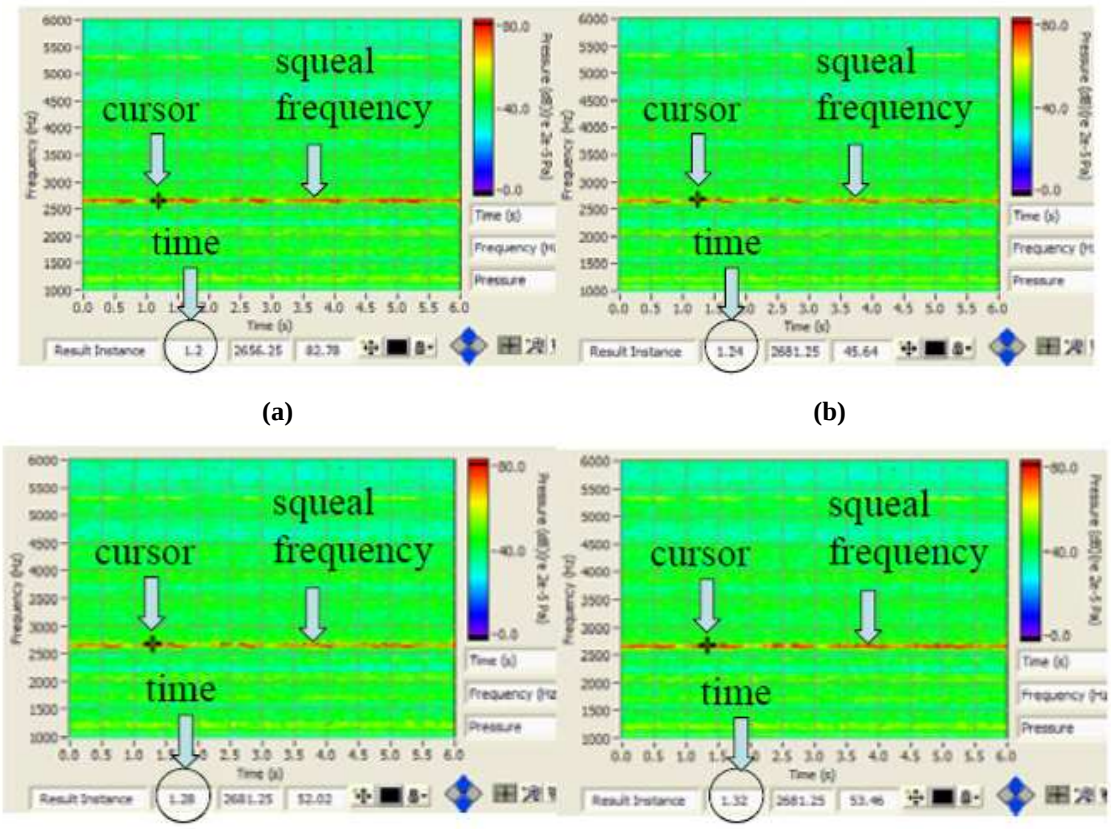

Figure 4.6: Spectrograms showing the major squeal frequency and time instances from 1.2 to 1.32 sec.

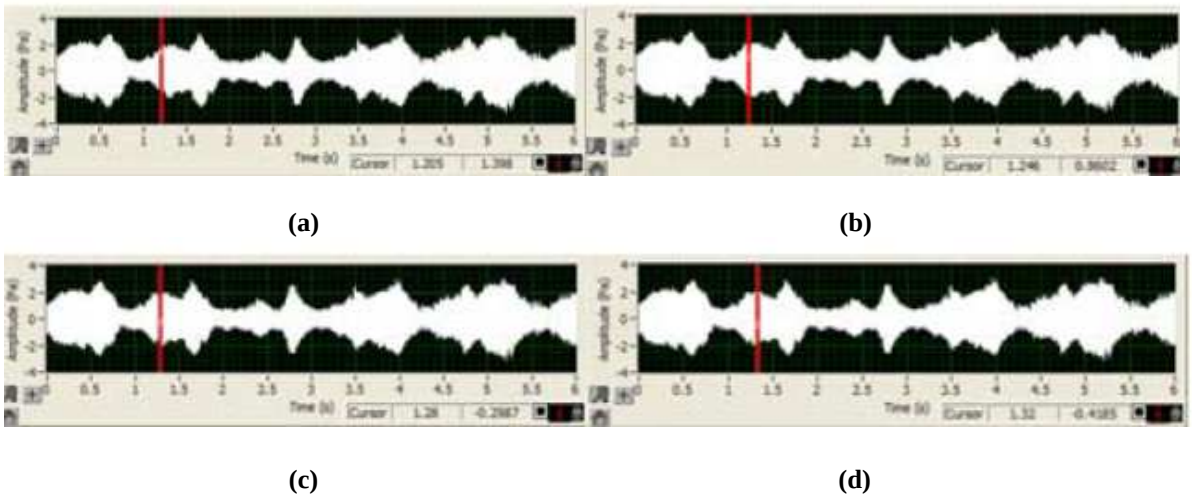

Figure 4.7: Real-time brake squeal signals. Red cursors indicate time instances from 1.2 to 1.32 sec.

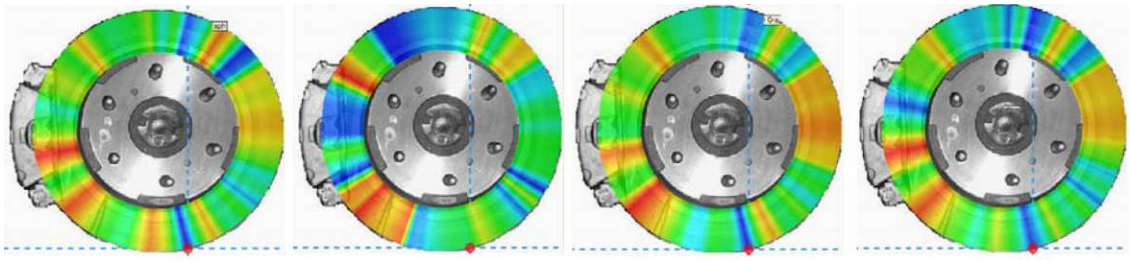

Figure 4.8: Reconstructed acoustic pressures on the brake surface at 2681Hz from 1.2 to 1.32 sec.

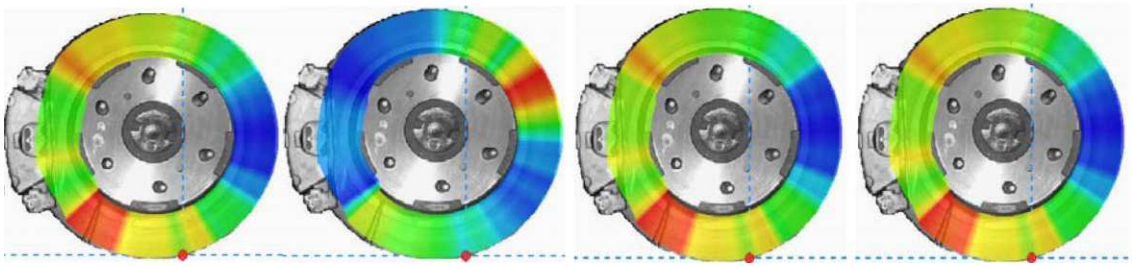

Figure 4.9: Reconstructed normal velocities on the brake surface at 2681Hz from 1.2 to 1.32 sec.

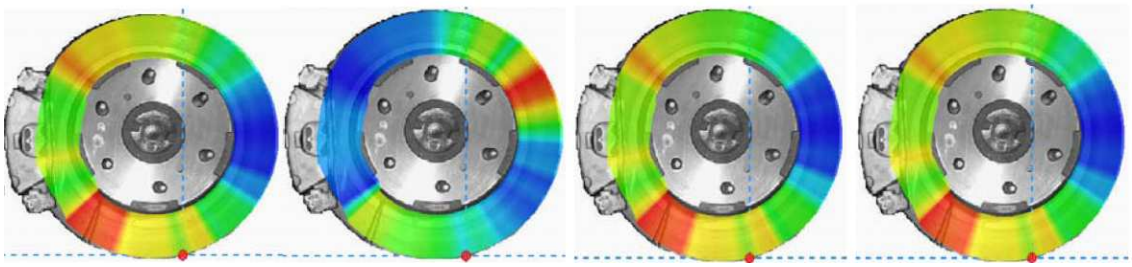

Figure 4.10: Reconstructed normal acoustic intensity on the brake surface at 2681Hz from 1.2 – 1.32 sec.

Figures 4.6-4.10 illustrate the sequence of events from 1.2 sec to 1.32 sec at a uniform interval of 0.04 sec, and demonstrate how the real-time squeal signal, reconstructed acoustic pressures, normal surface velocity, and time-averaged normal acoustic intensity distributions on disk brake surface change with time. These results provide unique insight into the distributions of brake squeals strengths and locations at which brake squeals are emitted from the disk surface. Such information cannot be acquired by conventional measurement technologies, i.e. a scanning laser vibrometer.

By using this technology, engineers have settled long-standing disputes over whether the vibration modes at squeals rotate with a rotor or not. Such a question cannot be resolved by conventional technologies.

In conclusion, HELS can handle complex brake squeals in a non-ideal environment and can yield all acoustic quantities, including the acoustic pressure, normal velocity, and normal acoustic intensity based on conformal acoustic pressure measurements at close range. One can identify the vibration modes that are responsible for brake squeals, and subsequently carry out a convenient and cost-effective brake squeal analysis.

4.2 Airplane Propeller Noise Visualization

As an example of application of the modified HELS method discussed in Chapter 3, we can demonstrate reconstruction of acoustic radiation from a twin propeller aircraft. In this case, the engine was running at an idle speed so noise was primarily produced by the propellers. The twin propeller aircraft and measurement setup are shown in Figure 4.11. The input data were collected by 60 microphones laid on the ground to minimize the effect of sound reflection from the ground. To describe the sound field produced by this aircraft, 20 virtual sources were distributed on the surfaces of impeller and engine (see Figure 4.12).

Figure 4.11: Test setup for a twin propeller aircraft.

Figure 4.12: Distribution of virtual sources.

Figures 4.13 and 4.14 illustrate the reconstructed sound pressure distributions on the impeller surface at the blade passage frequency and its harmonics in 3D space. This example demonstrates the potential of the proposed formulation to analyze the acoustics characteristics of aerodynamically generated sounds.

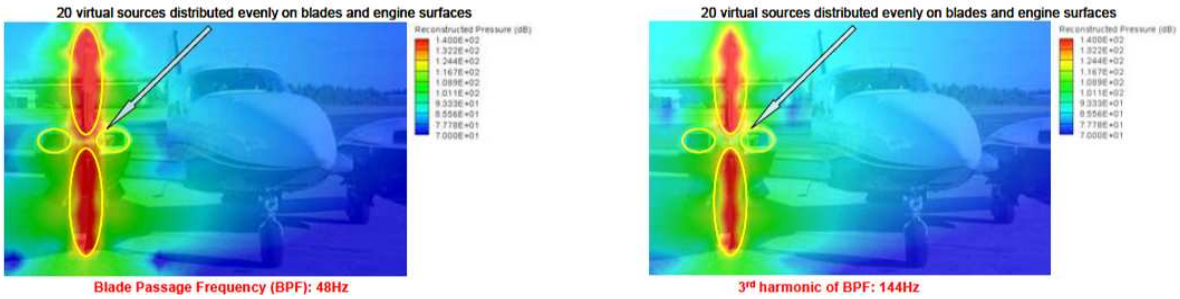

(a) **(b)**

Figure 4.13: (a) Reconstructed sound pressures at 48Hz. (b) Reconstructed sound pressures at 144Hz.

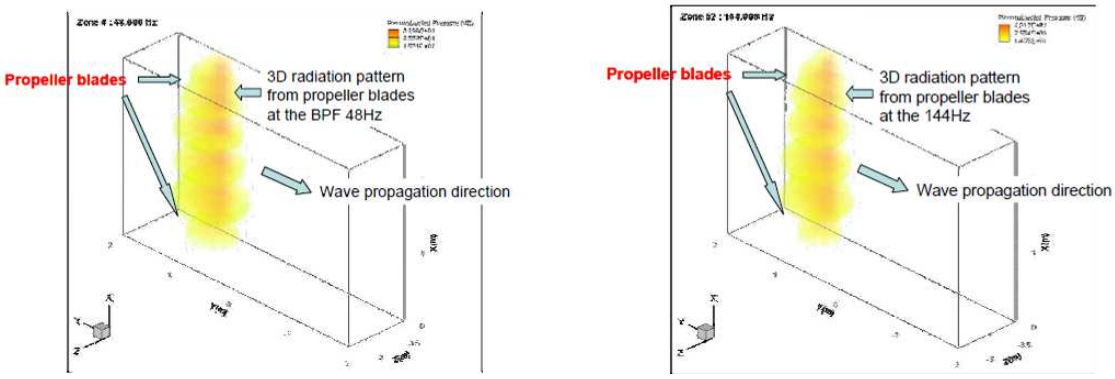

(a) **(b)**

Figure 4.14: Reconstructed 3D acoustic fields radiated from the impellers at (a) 48Hz (b) 144Hz.

It was observed that although virtual sources were distributed evenly on the propeller and engine surfaces, the source strength at the engine was much lower than that on propeller blades. This phenomenon was consistent with the fact that the engine was running at an idle speed. The source strength seemed quite uniformly distributed along the blade chord at BPF. This indicates that at BPF the blades were oscillating together at low frequencies. The source strengths seemed to converge into three segments along the blade chord at higher frequencies. This could be due to the fact that the blades vibrate at their own modes at higher frequencies. The source strength at the blade tip was not very high, which seems consistent with the fact that the major noise source is induced by a

fluctuating force exerted on the surrounding fluid medium by the blades, rather than by turbulence.

In conclusion, the modified HELS methodology allows for reconstruction of a 3D acoustic pressure field generated by any source, regardless of size, configuration or location, via measurements of acoustic pressures in the far field. It also enables one to visualize the acoustic source distributions on the surface of an arbitrary object over a wide frequency spectrum. Since the measurements are in the far field, test setup is very flexible, portable, and affordable.

CHAPTER 5 - RECONSTRUCTION OF IN-FLIGHT INTERIOR VIBRO-ACOUSTIC RESPONSE OF AN AIRCRAFT USING TRADITIONAL HELS METHOD

5.1 Introduction

Vibro-acoustic responses inside the fuselage of an in-flight business jet are reconstructed. Two microphone arrays were built to take acoustic pressure measurements inside the fuselage. One circular array was mounted on a track so that it could be moved in the longitudinal direction to measure the acoustic pressures along the circumference of the fuselage. Another planar array was used to measure the acoustic pressures on the closing surface of the fuselage in the bulkhead and cockpit positions, respectively. Over four thousand measurements of acoustic pressure were taken while the jet was flying at constant speed and altitude of 30,000 ft in the air. These measured acoustic pressures were taken as input to the Helmholtz Equation Least Squares (HELS) method to reconstruct the interior acoustic field, including the fuselage surface. The reconstructed normal surface velocities were checked with respect to the benchmark velocity spectra measured by the accelerometers mounted on the interior surface of the fuselage. This experiment demonstrates that HELS can be used to acquire a good understanding of vibro-acoustic responses inside an arbitrary interior region of a commercial aircraft.

5.2 Test Setup

A mid-size business jet Cessna XLS (Figure 5.1) was used in the test. Figure 5.2a and 5.2b show schematic diagrams of the tested aircraft.

Figure 5.1: Photograph of Cessna XLS aircraft dimensions.

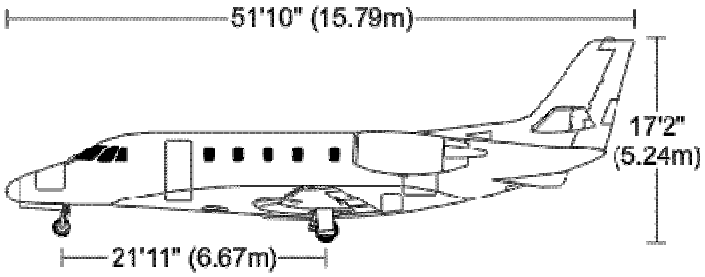

Figure 5.2a: Schematic of Cessna XLS aircraft dimensions.

All interior insulation panels in the passenger cabin, the toilet and the closet were taken out so that surface velocity can be reconstructed directly on to the fuselage surface. Figure 5.3 shows the fuselage stripped of all insulation panels, floor paneling, toilet, and closet towards the bulkhead.

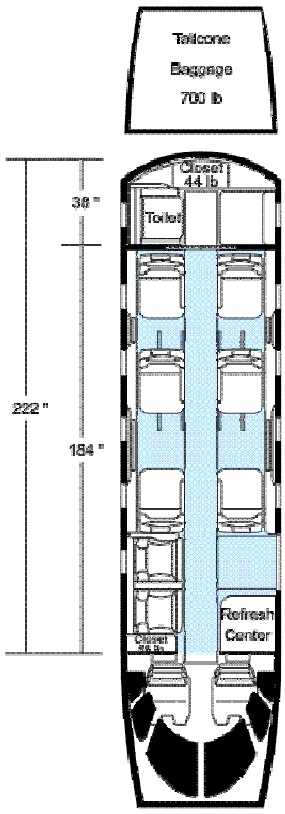

Figure 5.2b: Schematic of fuselage dimensions of Cessna XLS aircraft.

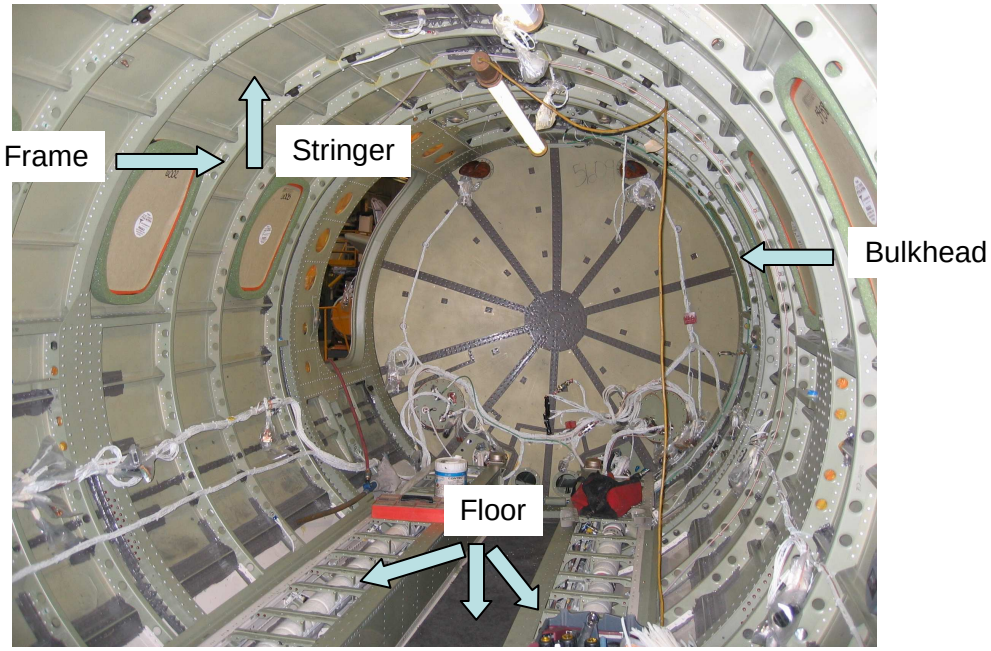

Figure 5.3: Stripped aircraft fuselage towards the bulkhead.

A conformal circular microphone array with 60 microphones was built (Figure 5.4 and 5.5) to take circumferential measurements and a planar microphone array of 50 microphones was built (Figure 5.6) for the closing surfaces measurements. The circumferential measurements were taken every 2 cm in the longitudinal direction with the measurement points located 2 cm from the skin.

The HELS formulation requires the microphone locations and the corresponding measured acoustic pressures at those locations as an input. The microphone locations were found by using 3D Sonic Digitizer kit made by the Modal Shop.

Throughout the test, the aircraft was flying at a steady altitude of 30000 feet and Mach number of 0.73. The two jet engines were running at steady N1=85% and N2=95% power. Microphone measurements were taken inside the fuselage to create a closed hologram surface. This closed measurement hologram surface included the fwd cabin skin and floor, aft cabin skin and floor and two imaginary closing surfaces (between the cockpit and the forward cabin and at the aft divider location).

The acoustic pressures in the interior region were then measured using the ICP 130D20 microphones manufactured by the PCB. These microphones were calibrated before performing the experiment. The calibration is scaled with a 114 dB tone at 250 Hz using Pistonphone type G.R.A.S. 42AA and the microphone output kept within ±0.15 dB of the tone amplitude. The phase data of the microphones was also acquired using the Larson Davis Residual Intensity Calibrator Model CAL291 and was stored in the computer for application to the field data at a later stage.

The PCB PIEZOTRONICS 64 channel multi-rack (16 channels each rack) Sensor Signal Conditioner Model 481A was used as signal-conditioning system to interface measurement signals to readout or recording devices. The unit also serves to provide excitation power for ICP-type microphones and acts as a low-pass filter. The output from the signal conditioners is then fed to the National Instruments' multi-channel Dynamic Data Acquisition cards Model 4472 (Total of 8 cards with 8 channels in a PXI-1006 chassis=64 channels) for processing on a desktop computer. This design of hardware configuration helps in simultaneous data acquisition of voltage signals from 64 sensors. Thus, this scheme shortens the data acquisition time and consequently reduces errors that may be introduced due to fluctuations in the test environment with time.

Figure 5.4: 60 microphone conformal array with telescoping arms for circumferential measurement.

Figure 5.5: Part of the conformal array used for measuring over the floor panel.

Figure 5.6: Picture of planar array used to measure the closing surface.

To maintain 2 cm offset from the cabin surface, arms of the conformal array are designed to be telescopic in nature. While traversing along the fuselage, arms of the array are telescoped in at the frame and are telescoped out at the skin to maintain a 2 cm measurement offset from all reconstruction surfaces.

i) Figure 5.7 shows the 3D representation of circumferential acoustic pressure measurement grid along the fuselage. Figure 5.8 shows transversal view of circumferential measurements. Figure 5.9 shows the 3D representation of acoustic pressure measurements on the closing surfaces towards cockpit and bulkhead. Figure 5.10 shows 3D representation of all circumferential and closing surface measurement locations together.

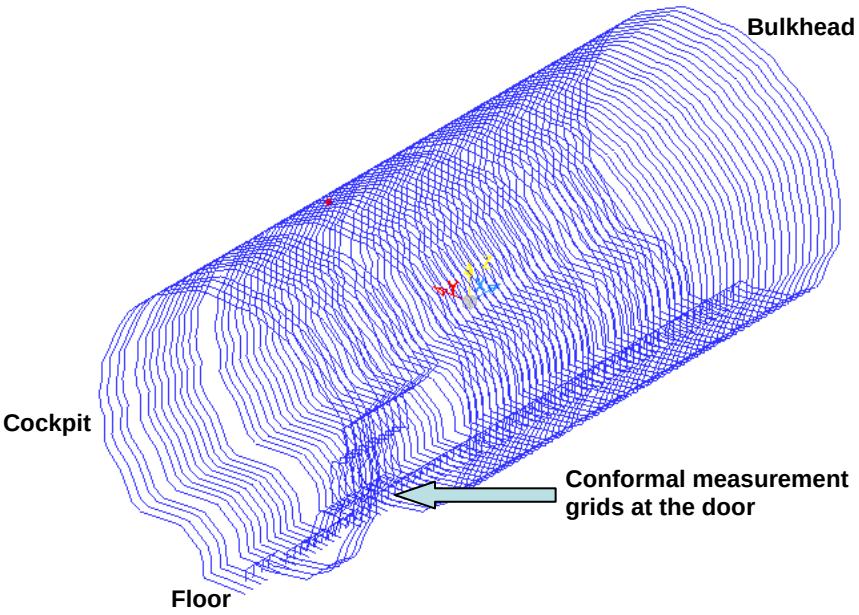

Figure 5.7: Circumferential acoustic pressure measurement locations.

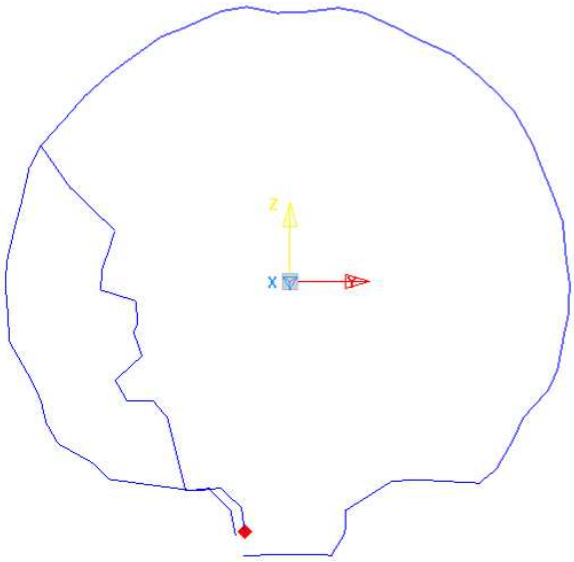

Figure 5.8: Transversal view of the circumferential measurements along the fuselage.

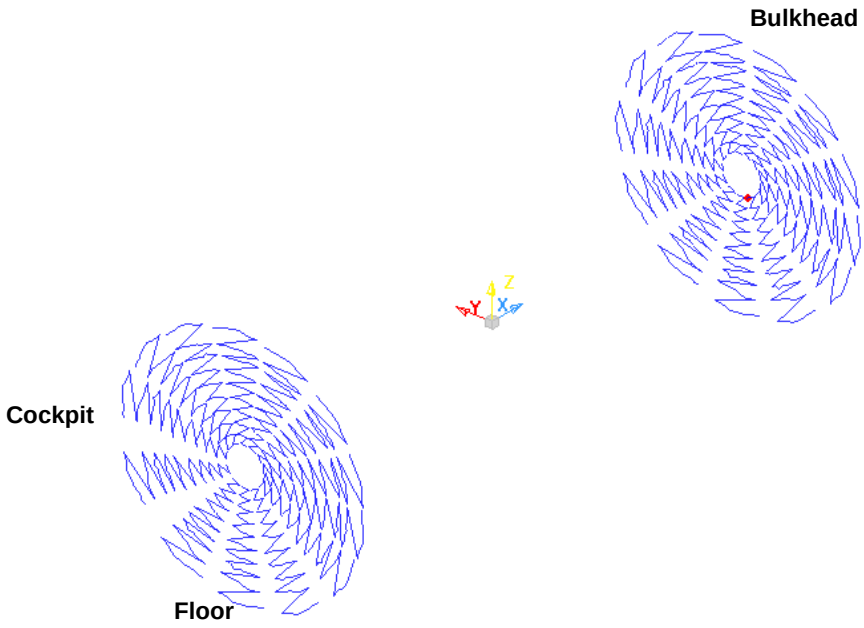

Figure 5.9: Closing surface acoustic pressure measurement locations towards cockpit and bulkhead.

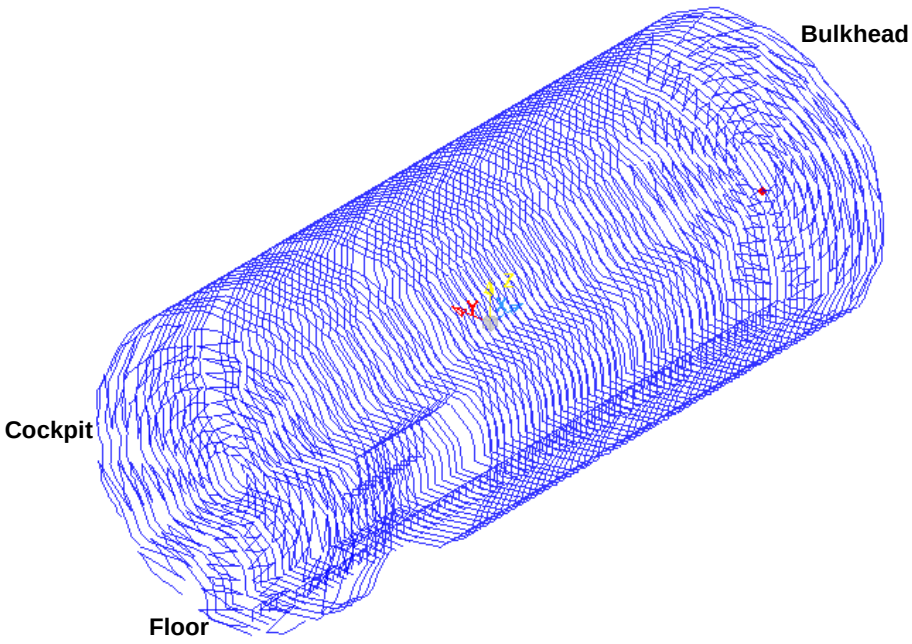

Figure 5.10: Closing surface measurements towards bulkhead and cockpit, and circumferential acoustic pressure measurement along the fuselage.

A total of three flights were taken to complete the test measurements over the whole fuselage area.

1. Flight 1: Circumferential measurements and benchmark accelerometers 1-15 in the forward cabin
2. Flight 2: Circumferential measurements and benchmark accelerometers 16-30 in the aft cabin
3. Flight 3: Radial measurements at imaginary surfaces between the cockpit and the forward cabin (F.S 180) and at the aft divider position to "close" the measurement surface

Figure 5.11 shows the circumferential measurements taken during the first two flights.

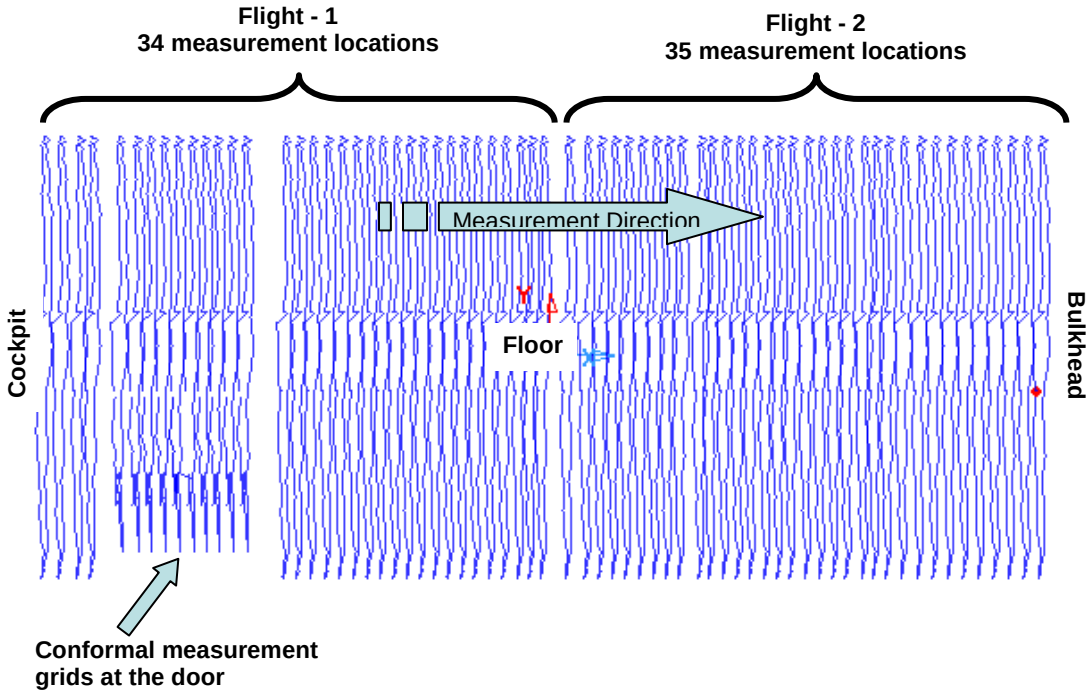

Figure 5.11: Closing surface measurements towards bulkhead and cockpit, and circumferential acoustic pressure measurement along the fuselage.

As discussed previously, for each set of measurement there are a total of 61 readings, 60 from the microphones in the array and 1 reference microphone placed over the area where the engines are connected to the fuselage as the reference signal. Accordingly, readings were taken over one longitudinal plane at a time and the data were recorded on the computer. At the end of each recording cycle the microphone array was moved to a new location manually. In addition, multiple flights were taken to acquire data in different parts of the fuselage. Manually moving the array and taking measurements over three flights may disturb the experimental setup and make the input data susceptible to errors. Although, efforts were made to maintain the repeatability of measurements, the fluctuations in the aircraft acoustic signal over the data acquisition

time can be significant. To alleviate this problem, transfer functions instead of the acoustic pressures were measured as shown in equation 5.1.

$$G(x_m \left| x_{ref}, \omega \right.) = \frac{\hat{p}_{field,m}(x_m, \omega)}{\hat{p}_{ref}(x_{ref}, \omega)} \tag{5.1}$$

where $G(x_m \left| x_{ref}, \omega \right.)$ represents the transfer function between the acoustic pressure at any measurement location $\hat{p}_{field,m}(x_m, \omega)$ and at the reference $\hat{p}_{ref}(x_{ref}, \omega)$. Once $G(x_m \left| x_{ref}, \omega \right.)$ were collected for all the array locations, the acoustic pressures were then obtained by multiplying the transfer functions by the acoustic pressure at the reference. Similar measurement technique was used for the closing surfaces, where 50 array microphones and the same reference microphone as the longitudinal measurements were acquired. Hence, this measurement scheme becomes equivalent to using a 5440-microphone array to measure the field acoustic pressures.

A 3D model of the fuselage interior surface was created and was used for reconstructing acoustic quantities over it. Figure 5.12 shows the reconstruction locations of the fuselage skin.

In addition to pressure measurements some benchmark accelerometer measurements were also taken on the fuselage surface. A total of 30 accelerometer measurements were taken over two flights (1-15 in second flight and 16-30 in third flight). Figure 5.13 shows the 3D locations of these accelerometer measurements on the fuselage skin.

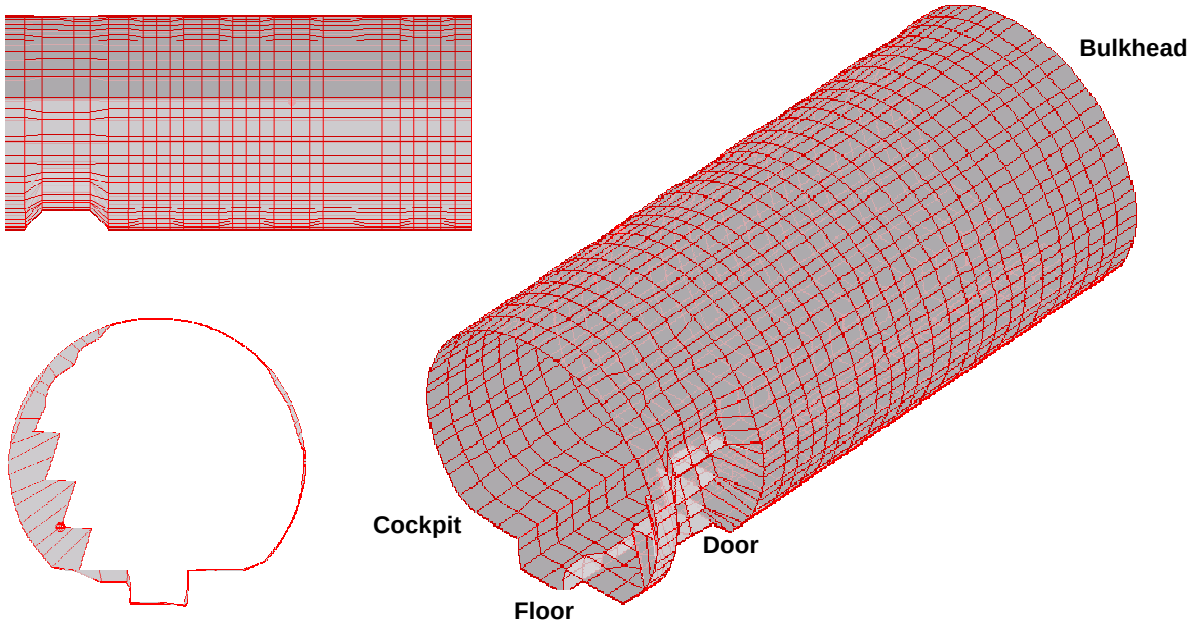

Figure 5.12: Reconstruction surface locations of aircraft fuselage.

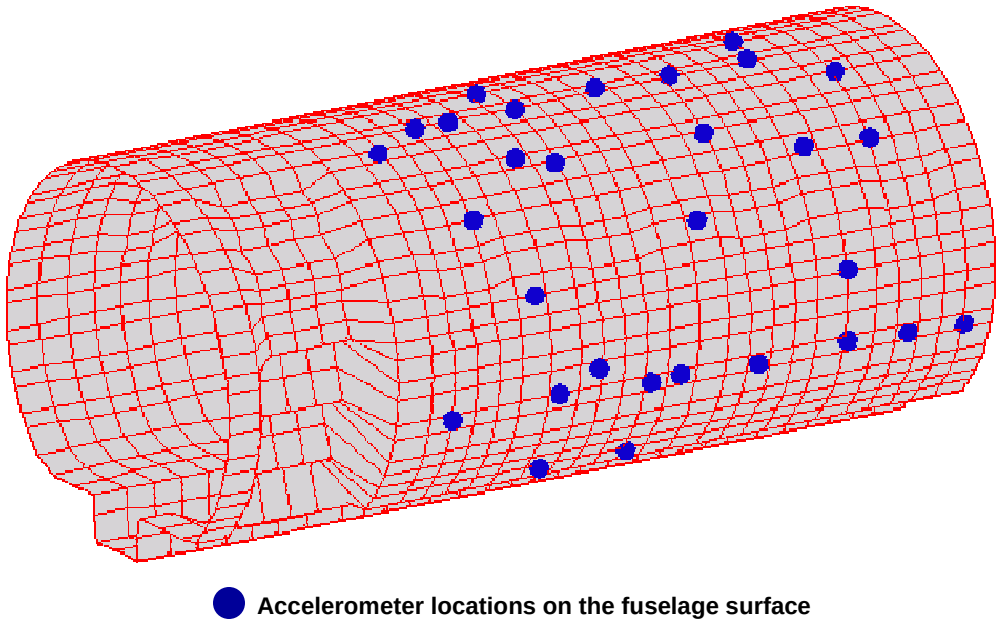

Figure 5.12: 30 accelerometer measurements taken over the fuselage surface in two flights.

Two imaginary surfaces towards the cockpit and bulkhead were also created to close the reconstruction cavity. Figure 5.13 shows the 3D representation of the end caps and fuselage skin reconstruction locations.

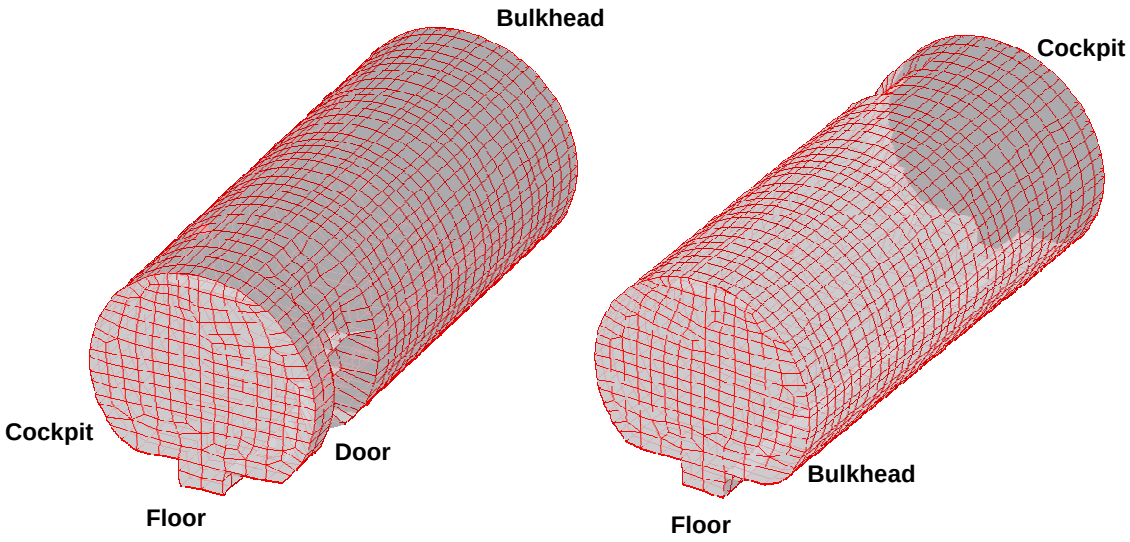

Figure 5.13: Fuselage surface and end cap reconstruction locations.

Since acoustic pressure measurements were taken almost along the entire fuselage and also over the closing surfaces, it is possible to reconstruct acoustic field in the entire 3D space inside the enclosed measurement volume, including the fuselage surface. As such, in addition to reconstructing all acoustic quantities on the fuselage surface, acoustic pressure is also reconstructed along seven horizontal planes along the fuselage. Reconstruction on these interior planes can allow us to visualize the interior cavity modes. Also, while generating these planes one of the planes is deliberately chosen to be lying on the approximate passenger ear plane. Figure 5.14a and Figure 5.14b show the fuselage surface and reconstruction locations of the seven horizontal planes inside the fuselage.

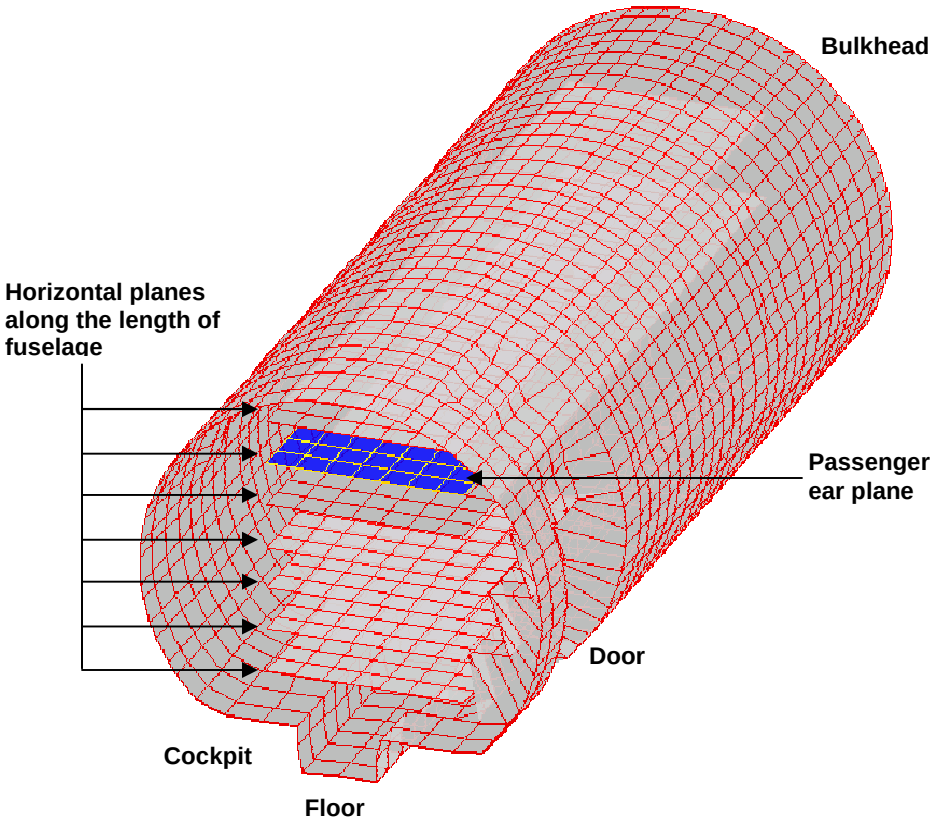

Figure 5.14a: Fuselage surface and reconstruction planes inside the fuselage cavity.

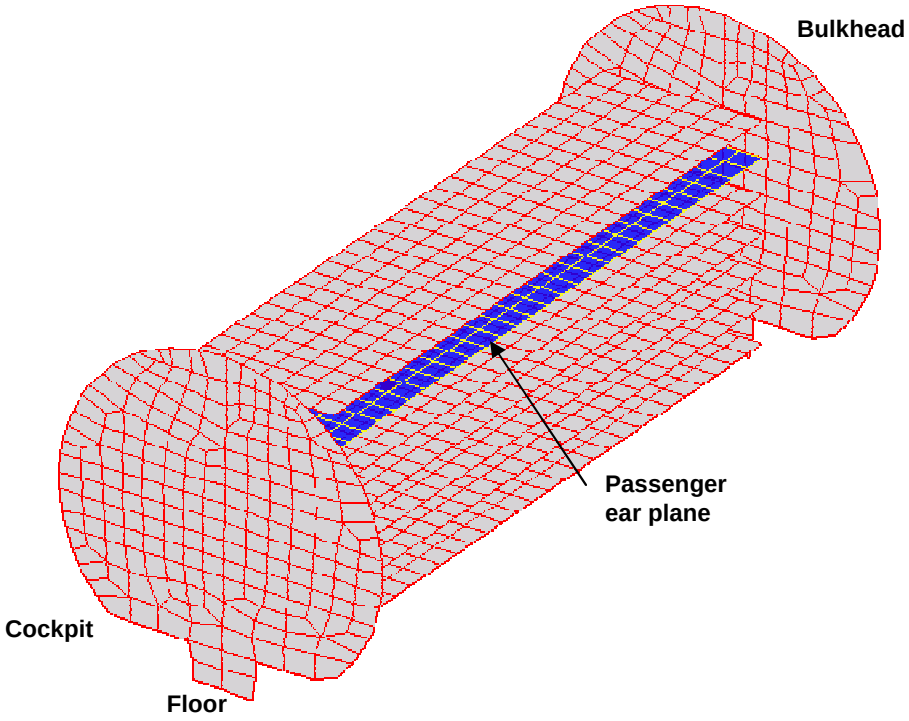

Figure 5.14b: End cap reconstruction locations and horizontal reconstruction planes inside fuselage cavity.

5.3 Reconstruction Strategy

As discussed previously, the HELS formulation is an expansion of spheroidal basis functions. As such, the HELS method may be used for any finite size source that can be enclosed in a sphere, but the results of reconstruction will be most accurate for a spherical object. On the other hand, the aircraft fuselage, though a simple geometry (rectangular), does not resemble a sphere. Thus, this inverse problem poses a significant challenge for the HELS method. In this investigation the acoustic parameters are reconstructed in the interior region of the fuselage and are discussed in the following subchapters.

As discussed in the previous chapter, the aircraft is flying with the engines providing steady power at 30,000ft. Under these cruising conditions, the fuselage cavity is excited by the vibrations from the engines and by turbulence around the aircraft. The resulting acoustic pressures acquired in the interior field were used to compute the acoustic pressures on the reconstruction surfaces and vibrating fuselage cavity surface. The use of random signals enabled reconstruction over a wider frequency range and generation of considerable amount of data for validations.

For the exterior case, a total of 4240 field measurements were used to reconstruct on fuselage surface and interior planes. Because of the errors involved in the measured data due either to the loss of near field effect or to measurement uncertainties the matrix equation (2.7) is ill posed. Thus an increase in the number of expansion terms will not necessarily yield more accurate reconstruction. Hence, an optimal number of expansion terms had to be found for accurate reconstruction of acoustic pressures.

An iterative scheme was followed to achieve this. Out of the 4240 field measurements only 2120 microphone measurements were used as collocation points and every other microphone was employed as an optimization location. For example, collocation microphones locations 1, 3, 5, ….., 4239 were used to reconstruct acoustic pressures over optimization microphone locations 2, 4, 6, ….., 4240 for a particular number of terms. The reconstructed and the measured acoustic pressures at the optimization locations were then compared and $||L||^2$ norm errors were calculated using equation (2.20) by replacing the benchmark pressures with measured acoustic pressures at the optimization locations. The reconstruction process was then repeated for a unit increase in the number of expansion terms unto the limit J=0.7N and the $||L||^2$ norm errors were stored in a file. Then the minimum norm error was read from the file and the corresponding number of expansion terms was taken as optimal for reconstruction over the entire fuselage surface, interior planes and benchmark accelerometer measurement locations.

5.4 Surface Velocity Reconstruction at Benchmark Accelerometer Locations

First, the surface particle velocities are reconstructed at the locations where benchmark accelerometer measurements (Figure 5.12) were taken. The comparison of frequency spectra of the measured and reconstructed surface velocity at the benchmark accelerometer locations on the fuselage surface are shown in Figures 5.15, 5.16, and 5.17. Note that reconstruction errors are usually larger on the edges or corners than those in the middle due to aspect ratio limitations discussed in section 2.4.5. Better agreement between the reconstructed and measured values was found in location away from edges and corners like at accelerometer 1 location. Figure 5.18 shows comparison of frequency

spectra of measured and reconstructed surface velocity at accelerometer #1 at the edge of the reconstruction surface.

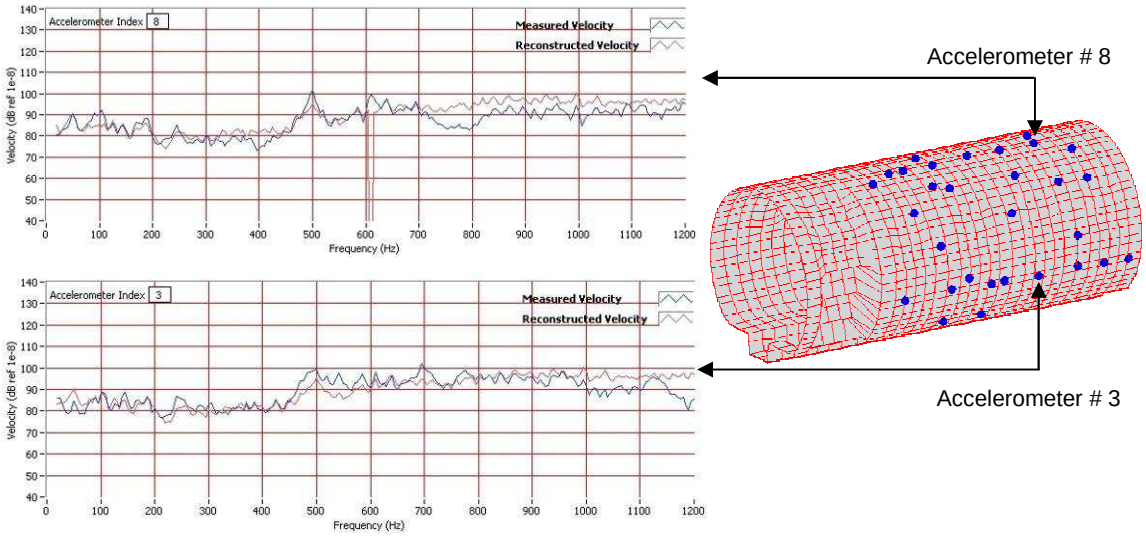

Figure 5.15: Comparison of measured and reconstructed velocity for accelerometer #s 3 and 8.

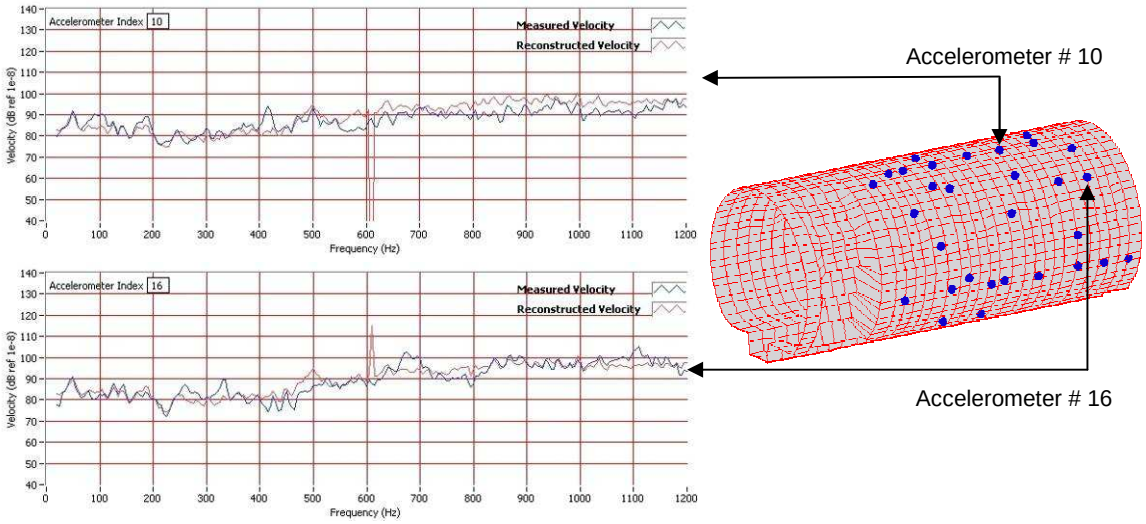

Figure 5.16: Comparison of measured and reconstructed velocity for accelerometer #s 10 and 16.

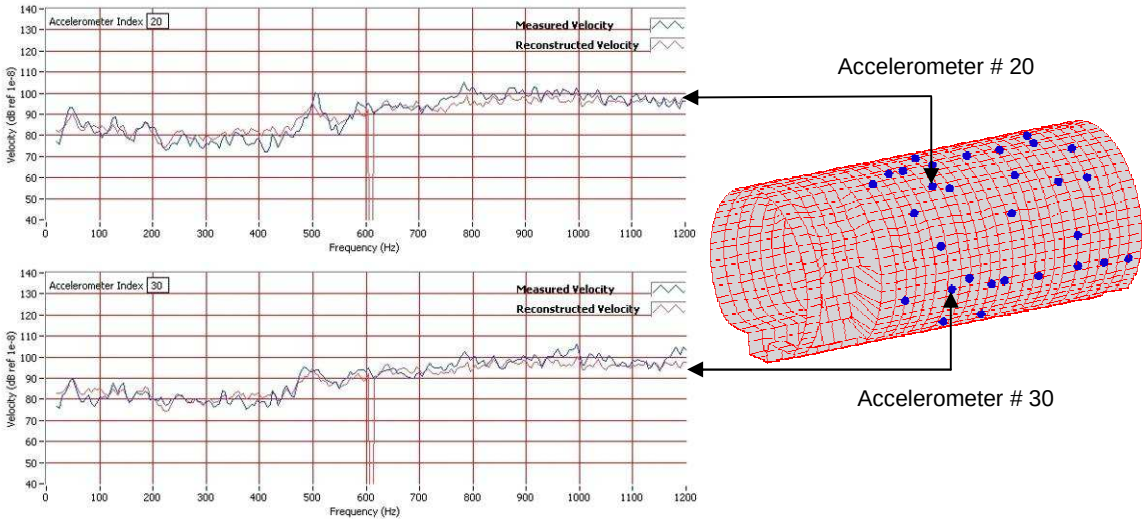

Figure 5.17: Comparison of measured and reconstructed velocity for accelerometer #s 20 and 30.

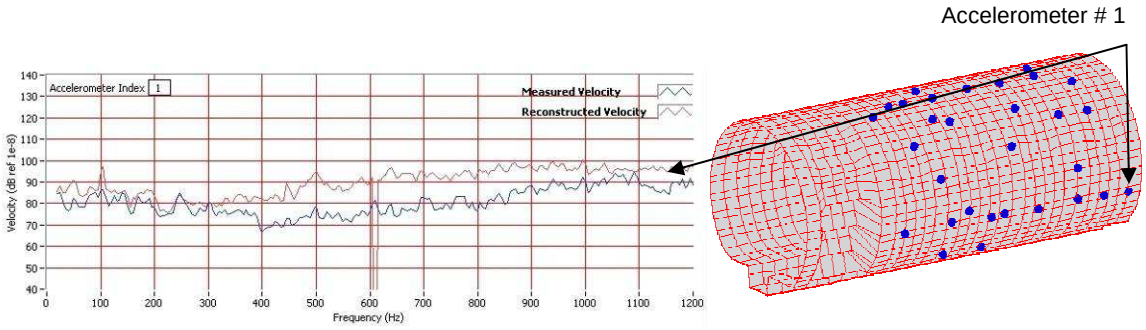

Figure 5.18: Comparison of measured and reconstructed velocity for accelerometer # 1.

Note that the HELS algorithm was not able to reconstruct surface velocity accurately at 610 Hz due to very ill-conditioned matrices as shown in figures 5.15-18.

5.5 Surface Pressure, Velocity and Intensity Reconstruction

The frequency spectra shown in figures 5.15, 5.16, 5.17, and 5.18 give an overall picture of the reconstruction results over a wide frequency range at one reconstruction location. Although, a frequency spectra gives a good inference towards behavior of reconstruction over all frequencies but the information is limited only to one reconstruction location and data interpretation over the whole reconstruction surface

becomes cumbersome. Surveying the acoustic pressure, surface velocity, and acoustic intensity distribution over the entire reconstruction surface at a particular frequency provides a more concise and perceptible reconstruction comparison. Figures 5.19, 5.20, and 5.21 surface velocity distribution over the reconstruction surface at 155 Hz, 795 Hz, and 915 Hz respectively.

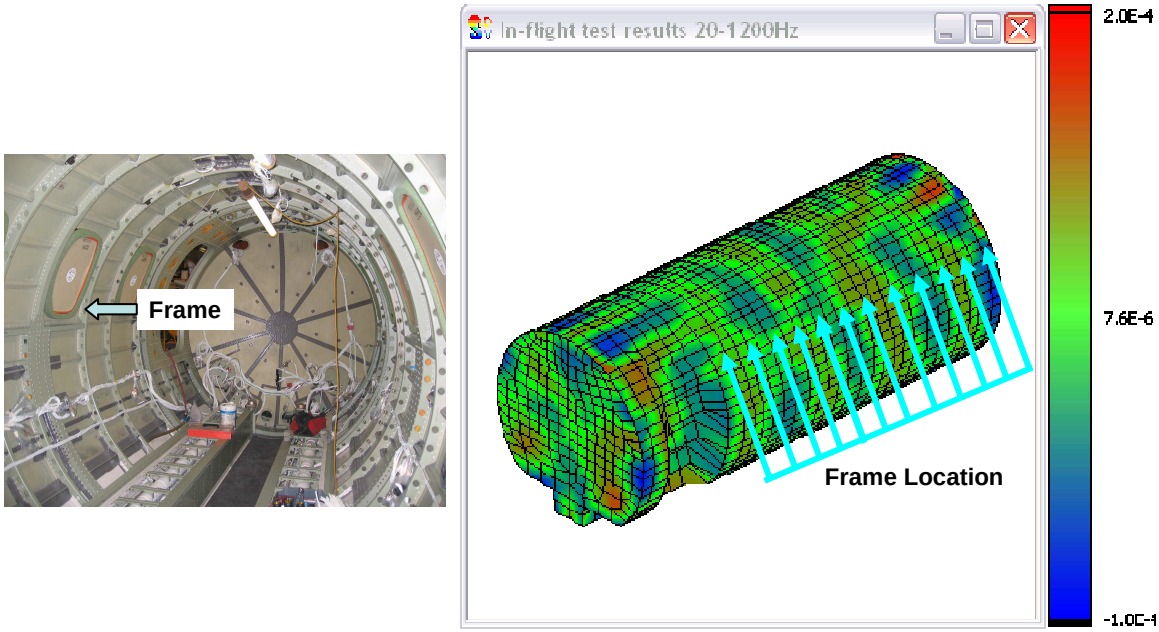

Figure 5.19: Reconstructed normal velocity distribution on the interior fuselage surface at 155Hz.

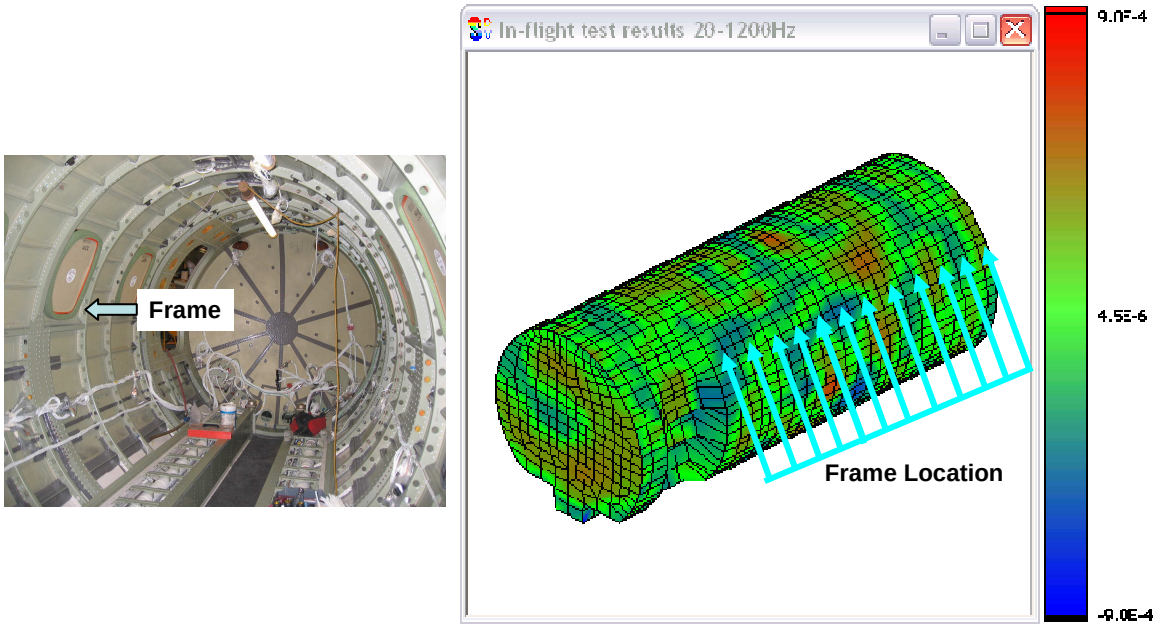

Figure 5.20: Reconstructed normal velocity distribution on the interior fuselage surface at 795Hz.

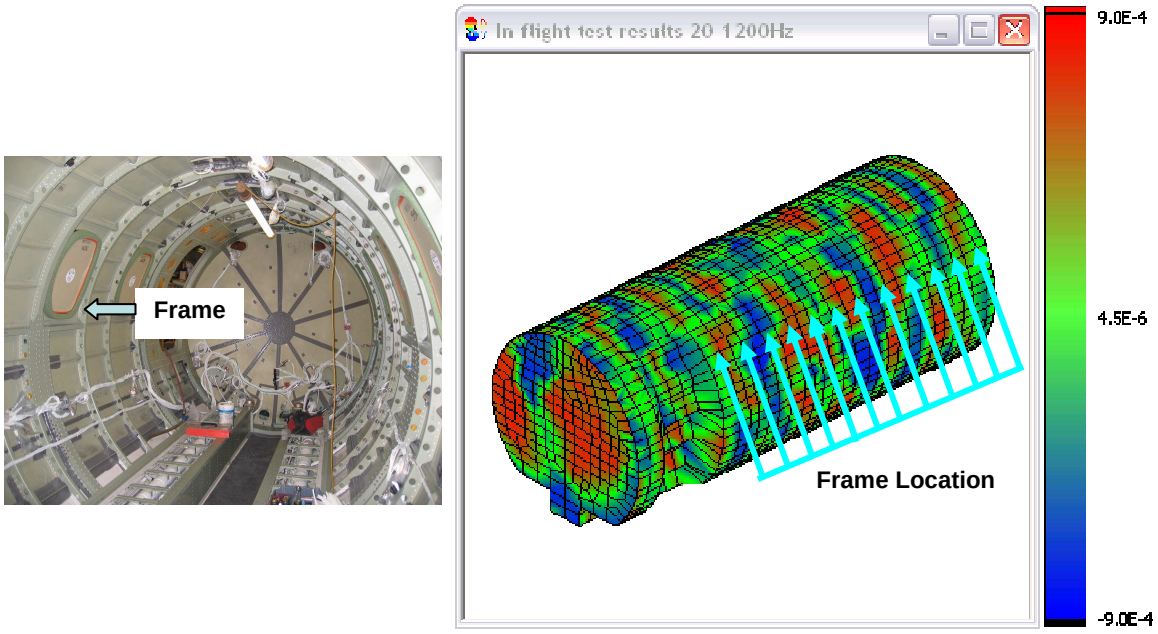

Figure 5.21: Reconstructed normal velocity distribution on the interior fuselage surface at 915Hz.

In addition to reconstructing surface velocity distribution, acoustic pressure and acoustic intensity on the fuselage surface is also reconstructed. For brevity, surface distribution of all acoustic quantities at 185 Hz, 190 Hz, 510 Hz and 515 Hz are presented in figures 5.22, 5.23, 5.24, and 5.25, where it is possible to identify “hot spot” in the cabin skin where sounds at these frequencies are more likely to be transmitted into the cabin.

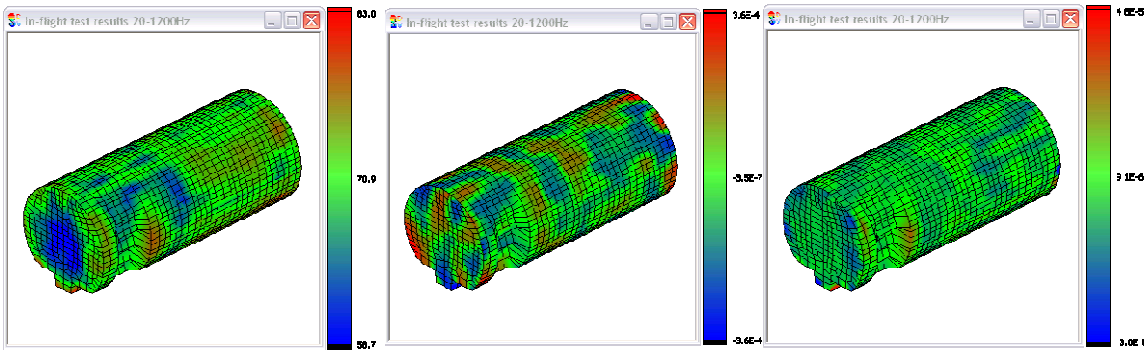

Reconstructed Pressure **Reconstructed Velocity** **Reconstructed Intensity**

Figure 5.22: Reconstructed acoustic quantities on the interior fuselage surface at 185 Hz.

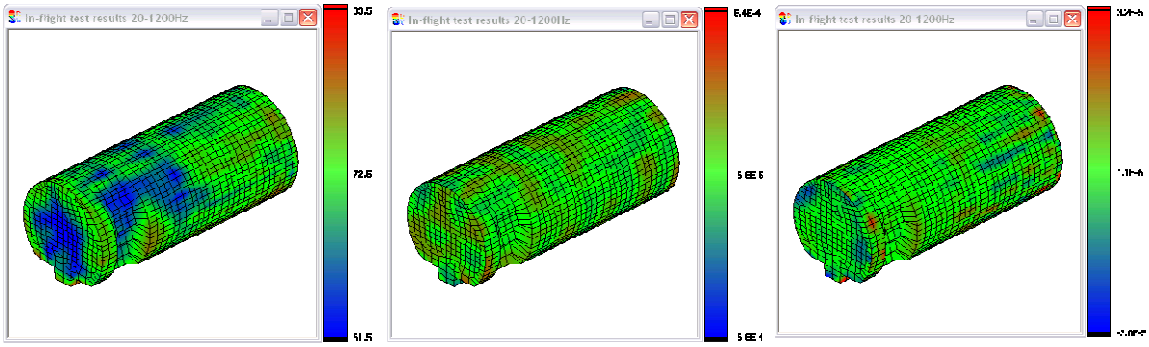

Reconstructed Pressure **Reconstructed Velocity** **Reconstructed Intensity**

Figure 5.23: Reconstructed acoustic quantities on the interior fuselage surface at 190 Hz.

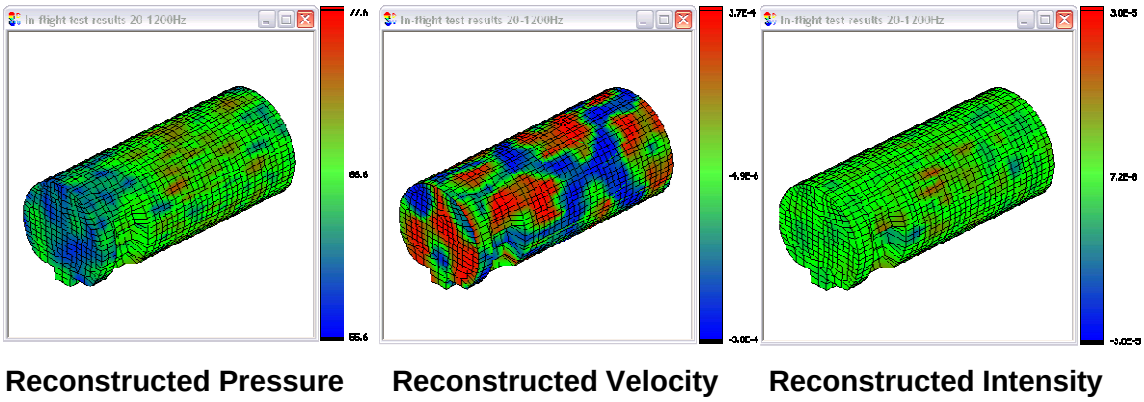

Figure 5.24: Reconstructed acoustic quantities on the interior fuselage surface at 510 Hz.

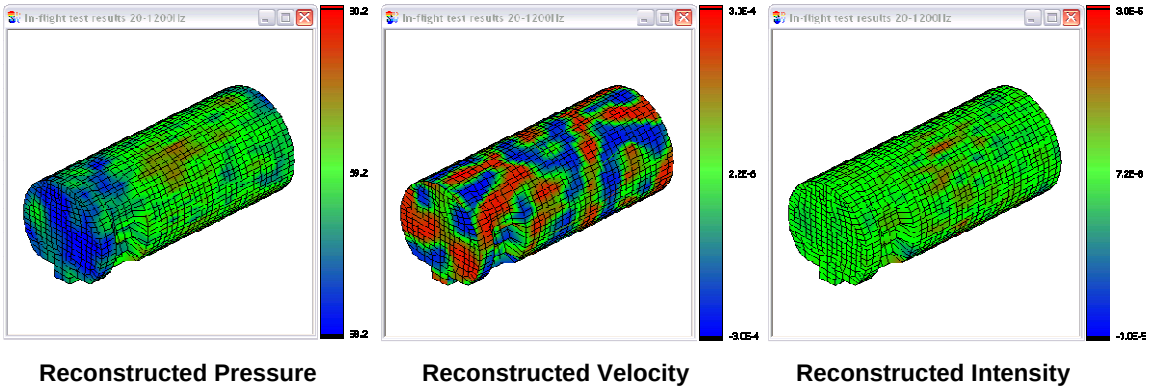

Figure 5.25: Reconstructed acoustic quantities on the interior fuselage surface at 515 Hz.

5.6 Reconstruction of fuselage cavity modes

As discussed previously, circumferential and closing surface measurements equivalent to 4240 microphone readings were taken as input to reconstruct over the measurement covered fuselage surface and interior planes. This acquisition plan also induces some errors in the input field data because of disturbance in the experimental setup for each of the array measurements. The method followed to minimize field data acquisition errors because of fluctuations in the test environment has been discussed in the previous chapter.

Later, surface velocity was reconstructed at benchmark accelerometer locations and has been found to be satisfactory. The next step is to visualize the acoustic pressure distributions over the interior planes inside the fuselage cavity. Reconstruction on these interior planes can allow us to visualize the interior cavity modes.

For brevity, acoustic pressure reconstruction over the interior planes is shown in figures 5.26, 5.27. 5.28, 5.29, 5.30, and 5.31 for 60 Hz, 165 Hz, 180 Hz, 205 Hz, 225 Hz and 295 Hz. We can clearly visualize the acoustic pressure distributions for increasing orders of interior modes with increasing frequency.

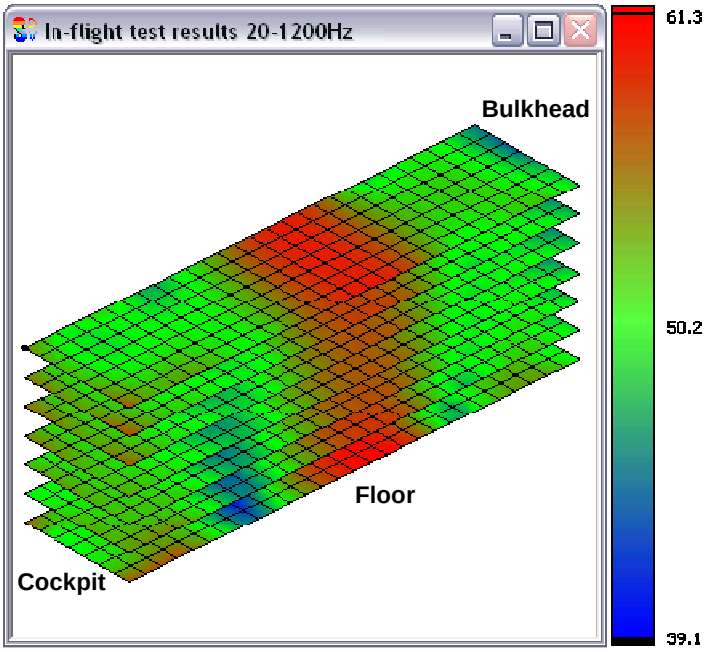

Figure 5.26: Reconstructed acoustic pressure on fuselage interior planes 60 Hz.

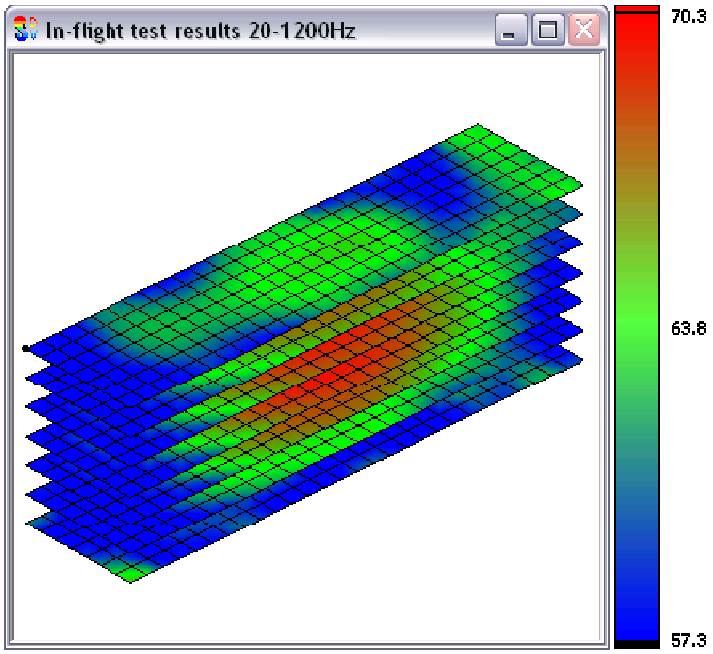

Figure 5.27: Reconstructed acoustic pressure on fuselage interior planes 165 Hz.

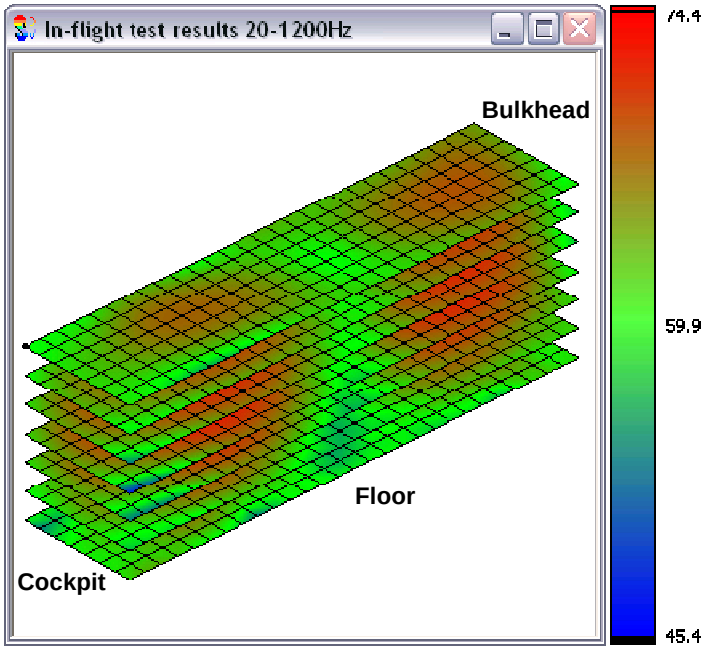

Figure 5.28: Reconstructed acoustic pressure on fuselage interior planes 180 Hz.

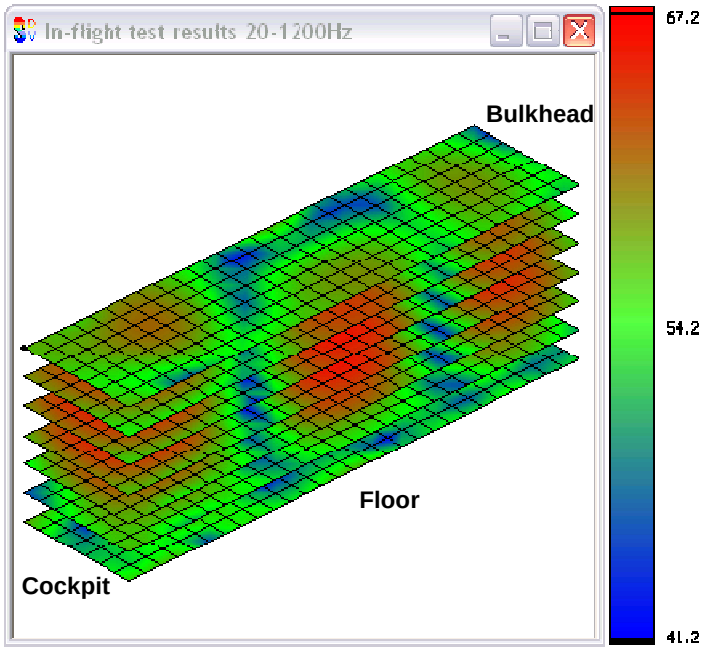

Figure 5.29: Reconstructed acoustic pressure on fuselage interior planes 205 Hz.

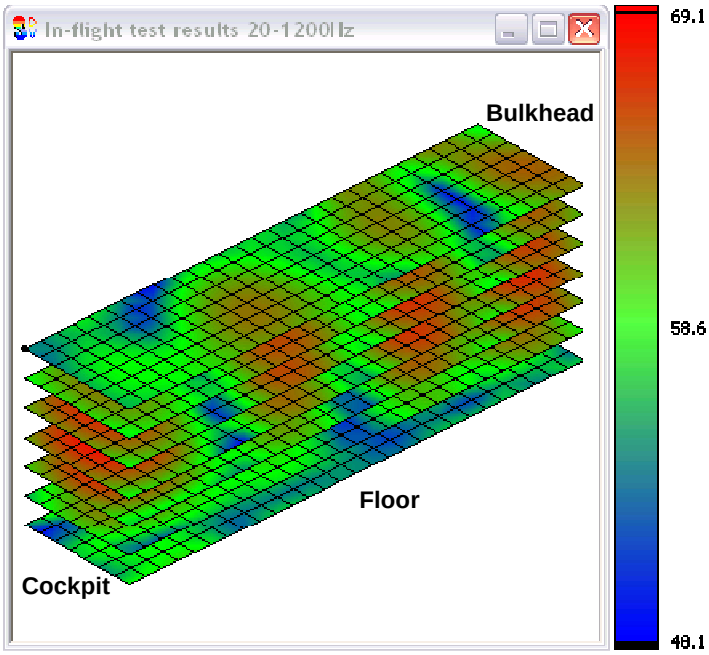

Figure 5.30: Reconstructed acoustic pressure on fuselage interior planes 225 Hz.

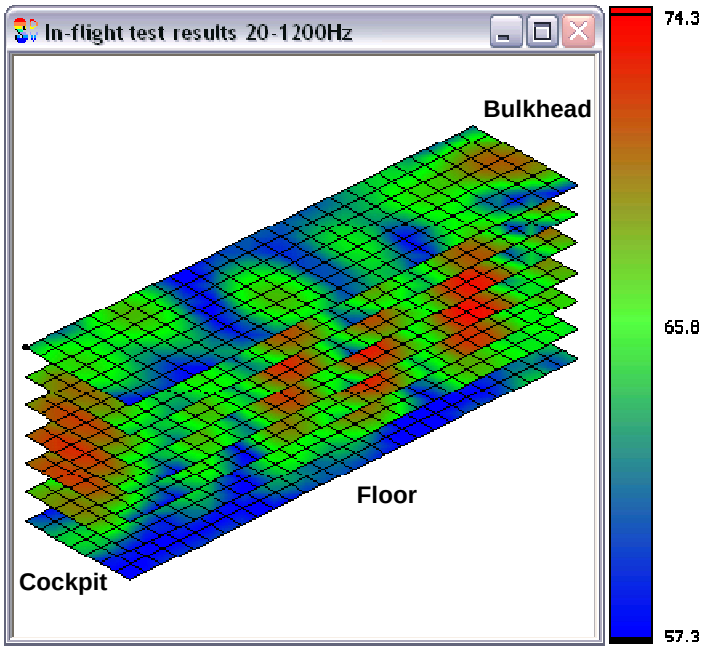

Figure 5.31: Reconstructed acoustic pressure on fuselage interior planes 295 Hz.

5.7 Concluding remarks

Aircraft NVH has always been one of the primary concerns in the aerospace industry because of ever-increasing demand of comfort and quietness. Oftentimes, the noise source strengths due to jet engines and turbulence around the aircraft and their transmission paths into the fuselage are unknown, which makes the analysis and reduction of aircraft interior NVH very difficult. There is also a great demand to ascertain the noise transmission in the exterior region and to reduce the flyby noise. Over the past decade many efforts have been made to analyze noise transmission. Yet to date, there is no single methodology that can be used to tackle these problems effectively.

Nearfield Acoustic Holography (NAH) followed by its commercial version Spatial Transformation of Sound Fields[3] (STSF) made an impressive foray in the noise diagnostics area. NAH has been particularly successful analyzing sources that conform

closely to the separable geometries. The reconstructions are very efficient, requiring only seconds of computation time per frequency[18]. However, for arbitrary shaped sources, Fourier transform based NAH fails to yield acceptable reconstruction accuracy. The NAH and BEM based nearfield acoustic holography provides the solution for arbitrary geometries, with a considerable sacrifice in computation time[23]. Further, this mating with BEM introduces a whole new set of limitations discussed in Subchapter 1.4.

A new nearfield acoustic holography (NAH) technique called the Helmholtz Equation Least-Squares (HELS) method was developed in 1997[19,20]. The present work discussed in this chapter primarily focuses on reconstructing the acoustic pressures in the interior region of a highly non-spherical vibrating fuselage.

The HELS method assumes the acoustic field in the interior and exterior regions to be a summation of certain wave functions. These wave functions may belong to Cartesian, cylindrical, spherical, or other spheroidal coordinate systems. Though there is no limitation on selecting the type of coordinate system and corresponding wave functions, for most real-world applications, spherical wave functions provide the best approximation of sound field around and within a 3D object. Furthermore, other spheroidal functions have no closed form solutions. Equation 2.4 shows the application of HELS method using spherical wave functions. The decision about the optimal number of expansion functions has to be made for correct representation of the sound field. The number of expansion terms cannot be too small or too large. Less number of expansion terms may not be able to describe the field at all and too large a number induces errors due to introduction of higher order terms. Errors in the input data are also responsible for

blowout of the solution with high number of expansion terms. A collocation type scheme discussed in Subchapter 5.3 has been used to decide upon the optimal number of terms. The number of expansion terms is found to be higher for the higher frequency range and vice versa for the low to mid-frequency domain.

The overall normal velocities, surface acoustic pressures, and normal acoustic intensity on the interior surface of the fuselage of a Cessna XLS Aircraft in flight condition were reconstructed. The reconstructed vibration response curves agree with those at benchmark points except at the edges. The overall vibration patterns reflect the fuselage design: the velocity amplitudes are small on frame but relatively large on panels. Fuselage interior modes were also visualized and a clear increase in complexity of interior modes can be seen with increase in frequency. Also, with one experimental measurement of acoustic pressure, all three acoustic parameters (pressure, velocity, and intensity) are reconstructed. These parameters can then be used for validating simulation data from SEA and/or FEA models, for example. All validations in the interior region have been performed over the enclosures that have rigid or completely reflective walls. In other words, the sound field is reactive in nature. Thus we can conclude that the HELS method provides satisfactory reconstruction results for completely reflective or reactive sound field in the interior region.

During the course of this research a fully functional prototype of the HELS based nearfield acoustic holography system has been developed. Some coarse details of this system and its various hardware and software components are enlisted in Appendix-A.

CHAPTER 6 – VISUALIZING JET PLUME NOISE USING THE MODIFIED HELMHOLTZ EQUATION LEAST SQUARES METHOD

6.1 Introduction

Reduction of jet noise has always been one of the major topics of interest for the commercial aviation industry, Department of Defense (DoD), and National Aeronautics and Space Administration (NASA). Much effort has been devoted to enhancing the performance of fighter jets while reducing noise levels of jet engines.[47-49] Many methods have been developed over the past several decades to measure and predict jet noise, such as the infrared radiation (IR) imaging system to acquire real-time dynamic thermal patterns of the exhaust jets from the engines,[50] laboratory experiments of full-scale jets to validate direct numerical simulations, large eddy simulations,[51-54] and Reynolds averaged Navier-Stokes codes.[55] However, most of these studies are focused on fluid dynamics because the acoustic source characteristics of jet plumes cannot be defined. This is due to the difficulty in making a complete set of descriptive acoustic measurements characterizing the size, intensity, directivity, and distribution of the acoustic source strengths inside a jet plume. Another method employed uses far-field microphone measurements to gain insight into the jet engine noise characteristics. Figure 6.1 shows this measurement methodology.

Recently, NAH has been proposed to examine the acoustics characteristics of jet plumes. However, conventional NAH technologies are not applicable for full-size jet engines, because conventional NAH technologies rely either on taking Fourier transform

in different domains over a surface that has a level of constant coordinates, or on solving the Helmholtz integral formulations via boundary element method (BEM).

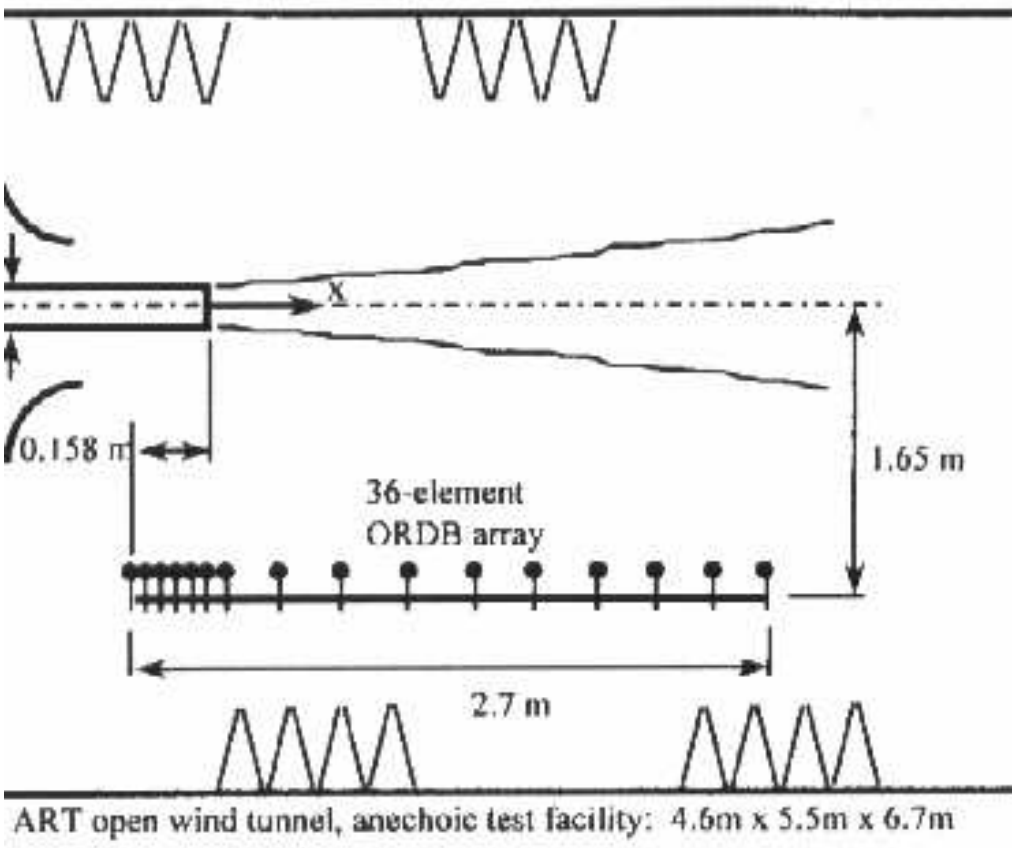

Figure 6.1: Jet noise measured by microphones placed in the far field is not helpful to gain insight into jet noise.

On the other hand, jet plumes cannot be depicted by a level of constant coordinates. Most importantly, Fourier transform based NAH is valid in a source-free region only, whereas a jet plume itself signifies a continuous distribution of sources. Therefore, there is no way for Fourier transform based NAH to analyze the acoustics characteristics inside a jet plume. BEM based NAH is not suitable for this task because a jet plume is not as well defined as solid structures. Figure 6.2 shows a typical jet engine

and plume. Moreover, BEM based NAH will require an unrealistically high number of measurement points, making it virtually useless for this project.

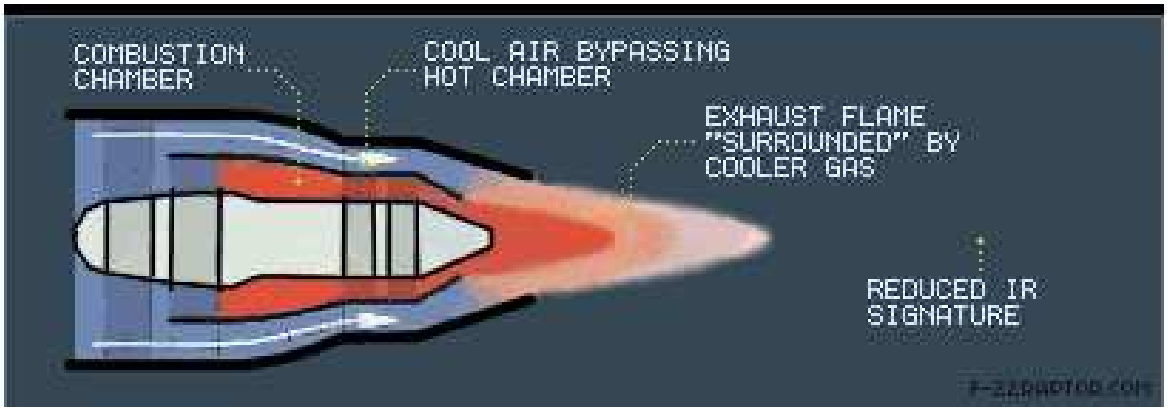

Figure 6.2: A typical jet engine and plume.

Unlike these conventional NAH implementations or the Fourier transform based NAH, HELS formulations offer great flexibility in engineering applications. The main reason is that HELS does not seek an exact solution of an acoustic field produced by an arbitrarily shaped structure. Rather, HELS attempts to find the best approximation to an acoustic field based on any given set of input data. So the more accurate the input data are, the better the HELS results are. However, the original HELS formulations cannot be used to analyze the acoustic characteristics of jet plumes. A better approach is to use the modified HELS, which enables one to describe an acoustic field in terms of expansions with respect to a number of points in space. In practice, one can distribute as many virtual sources as needed to describe a sound field of interest.

In the proposed project, we plan to distribute a number of virtual sources that represent monopoles, dipoles, and quadrupoles along the axis of symmetry of the jet engine, and use them to approximate the resultant sound field. This approach can be very

effective since the aerodynamically generated sounds consist primarily of contributions from monopoles, dipoles, and quadrupoles.

6.2 Test Setup

Jet engine plume noise characteristics are reconstructed for one of the engines of a passenger jet aircraft. The passenger jet was parked outside its hangar at Detroit City Airport (Figure 6.3) and the jet engines were run at idle speed. This was because our measurement microphones have limited dynamic ranges (40 – 122dB overall) and any higher speeds will lead to exceeding that dynamic range limit in the near-field of the jet engine plume. The sound field produced by this low-speed turbulent flow was shown to be adequately described by using three different schemes of distributed virtual sources along the axis of symmetry discussed in subchapter 6.3.

Figure 6.3: Passenger jet aircraft parked at Detroit City Airport.

Arrays of microphones and stands were designed and built so that conformal measurements of sound pressures could be taken around the jet plume. Two aluminum rod rings were designed to hold microphone arrays. Diameters of these rings were carefully determined so that microphones could be placed as close to the jet plume as possible, yet without contaminations by turbulent flow from the jet nozzle. The diameters of these two rings were 0.9m and 1.69m, respectively, whereas that of jet nozzle was 0.53m. 31 microphones were spaced at 0.077m and rotated along the rings at every 5.6° over 360° range. This resulted in 1984 measurement points around the jet plume. Measurements were taken continuously one after another while the jet engine was running at idle speed.

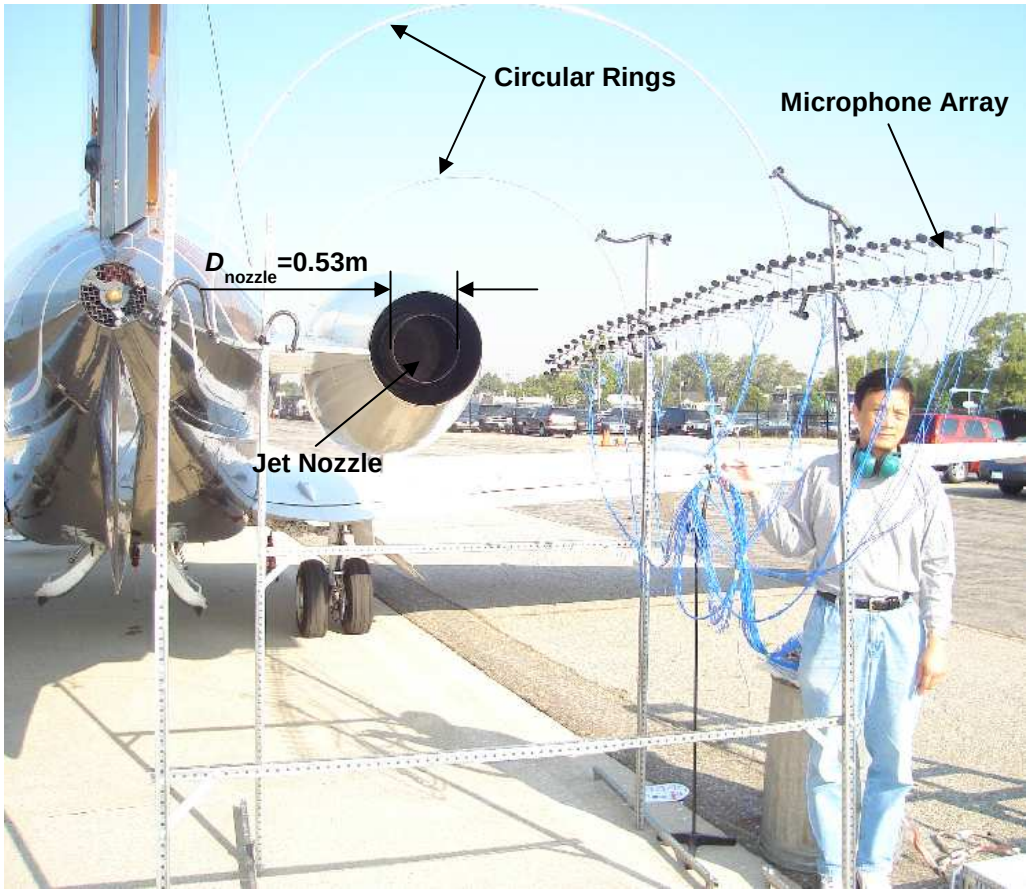

Figure 6.4: Test setup photograph showing the jet engine and microphone array used for measurement.

Figure 6.4 shows the test setup used for acoustic pressure measurements around the jet engine plume. Although every effort was made to ensure repeatability of acoustic pressure measurements, the fluctuations in the jet engine acoustic signal over the data acquisition time can be significant. To alleviate this problem, instead of measuring the raw acoustic pressures, transfer functions, as described in Eq. 5.1 were measured. To implement Eq.5.1, the reference microphone was placed right next to the jet nozzle. The position of the reference microphone was chosen such that it was as close to the jet nozzle as possible but still out of the jet plume flow. Also, the microphones were protected from turbulence by using windscreens.

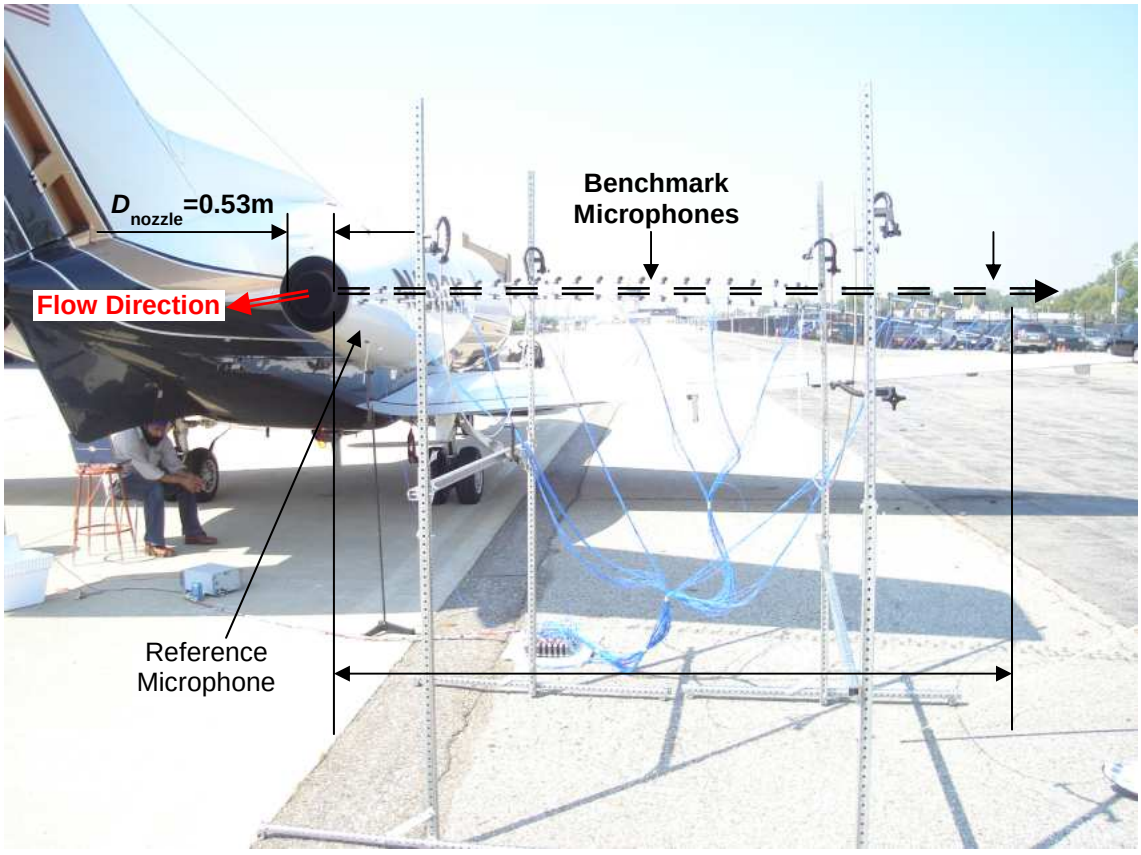

Figure 6.5: Reference microphone setup at close range to the jet nozzle and benchmark microphone array setup in the direction perpendicular to the jet flow.

Figure 6.5 shows test setup for benchmark microphone array. It also shows the location of reference microphone placed right next to the jet nozzle. This reference microphone was kept at the same location throughout the test for all field and benchmark acoustic pressure measurements. These setups allowed us to “stitch together” 64 individual microphone array measurements and simulate one big array measurement with 1984 microphones.

To validate the reconstructed acoustic pressures, benchmark pressures perpendicular to the jet flow direction were taken as well. These benchmark array microphones extend up to 4.5Dnozzle in the direction perpendicular to the flow as shown in figures 6.5. Figure 6.6 shows a 3D representation of benchmark microphone array with respect to the jet engine and field microphone measurement around the jet plume

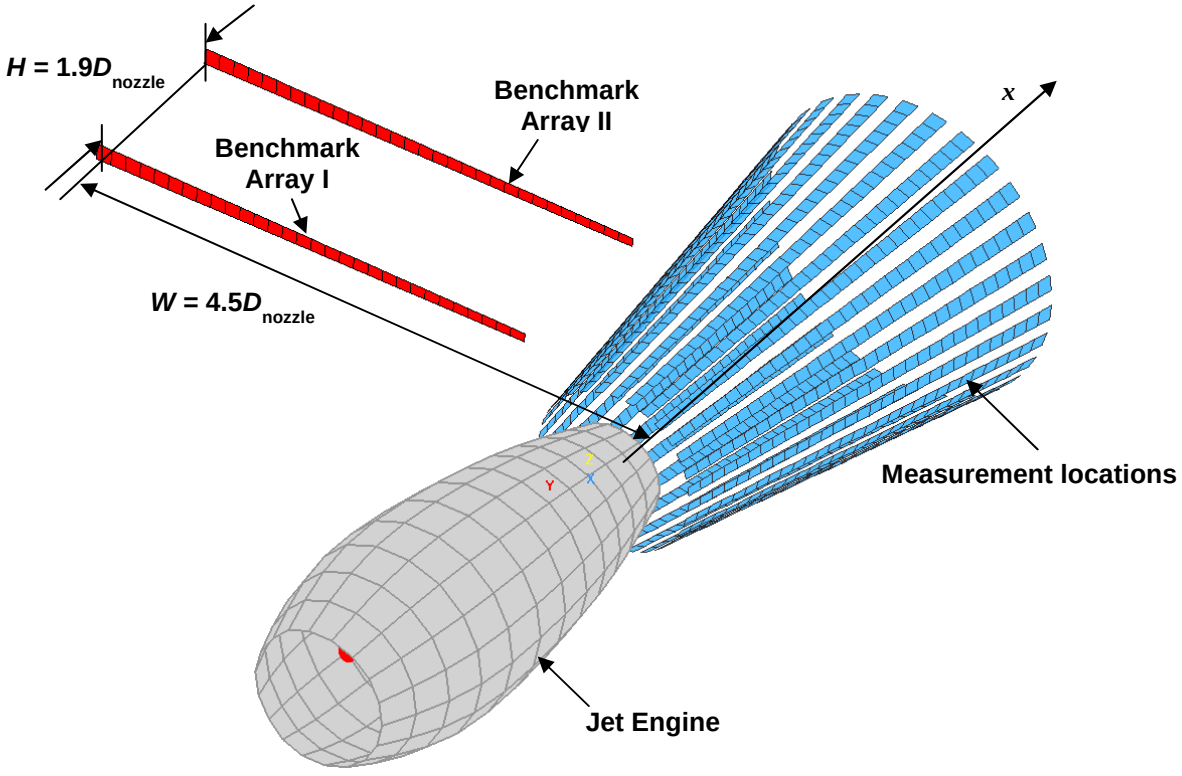

Figure 6.6: Schematic of test measurement and validation process.

6.3 Reconstruction Strategy

As discussed in chapter 2, the original HELS formulation is suitable for reconstructing sound radiation from a vibrating structure that is stationary and well defined in space. For an aerodynamically generated sound, such as that produced by turbulent flow ejected from a jet nozzle, the conditions for applying the original HELS method are not satisfied. For such a turbulent flow, the source locations and strengths are not fixed in space and change with flow speed. Finding an exact solution for such a flow becomes a challenge. As such, a new modified HELS formulation was introduced in Chapter 3 which accounts for contributions from different sound generation mechanisms such as monopoles, dipoles and quadrupoles. In addition, as compared to using one virtual source for the original HELS method, the new methodology allows one to distribute multiple virtual sources within or around the jet engine plume.

The locations of these virtual sources needs to be optimized to best approximate a sound field produced by a target source. For a jet engine plume, these virtual sources could be placed in the entire 3D space of the plume itself and they can be uniformly or randomly distributed. For the current test, the jet engine is run at idle speed and it can be safely assumed that all noise is produced by linear phenomena. This simplifies virtual sources optimization process as the acoustic field could be described by simply distributing sources along the axis of symmetry. Two different schemes are used, one with uniformly distributed virtual sources and the other with virtual sources biased towards the jet engine nozzle. For both these virtual source distribution schemes, virtual sources are distributed along a length of up to 18 times the diameter of jet nozzle in the flow direction.

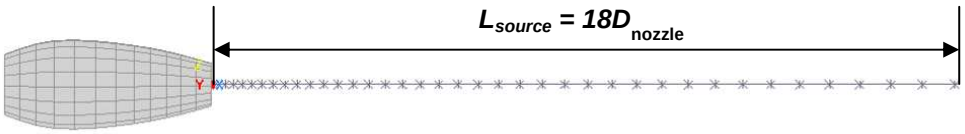

Figure 6.7: Schematic of 45 virtual sources distributed along the jet plume axis and biased towards the jet nozzle. The virtual sources extend to approximately 18 times the diameter of jet nozzle

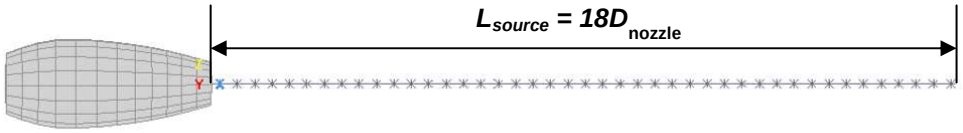

Figure 6.8: Schematic of 45 virtual sources distributed uniformly along the jet plume axis. The virtual sources extend to approximately 18 times the diameter of jet nozzle

Figure 6.7 shows virtual source distribution scheme with 45 virtual sources biased towards the jet engine nozzle and Figure 6.8 shows 45 virtual sources distributed uniformly along the jet plume axis up to a distance equivalent to 18 times the diameter of jet nozzle or approximately 9.5m.

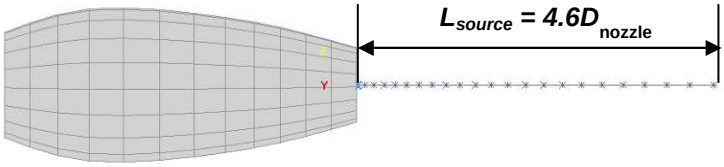

Figure 6.9a: Schematic of 31 virtual sources distributed along the jet plume axis and biased towards the jet nozzle. The virtual sources extend to approximately 4.6 times the diameter of jet nozzle.

In addition to the above two virtual source distribution schemes, another scheme with a shorter length was used to reconstruct the acoustic pressures around the jet plume. Figure 6.9a shows this scheme where 31 biased sources are placed on the jet plume axis extending up to approximately 4.6 times the dimater of the jet nozzle. The virtual sources

in this scheme extend slightly out of the measurment array which extends to 4.5 times the jet nozzle diamter. This is depicted in Figure 6.9b.

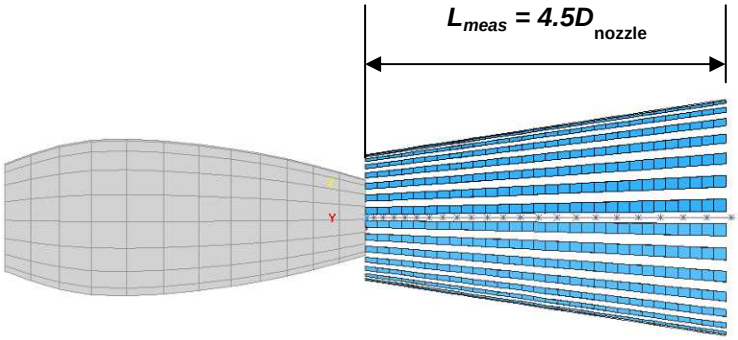

Figure 6.9b: Schematic of microphone measurements and 31 virtual sources distributed along the jet plume axis and biased towards the jet nozzle. The measurement array extends to 4.5 times the diameter of jet nozzle.

All 1984 microphone measurements are then used in Eq 3.2 and coefficients are calculated by using the assumed form solution. The errors are minimized by using the least-square error between the approximated reconstructed solution and the measured acoustic pressures from the microphones in the microphone array similar to the traditional HELS methodology discussed in subchapter 5.3.

The reconstructed and the measured acoustic pressures at the optimization locations were then compared and $||L||^2$ norm errors were calculated using equation (2.20) by replacing the benchmark pressures with measured acoustic pressures at the optimization locations for all three virtual source distribution schemes discussed above. Figure 6.10 shows comparison of $||L||^2$ norm errors for a frequency range of 900Hz to 6135Hz for the three different virtual source distribution schemes.

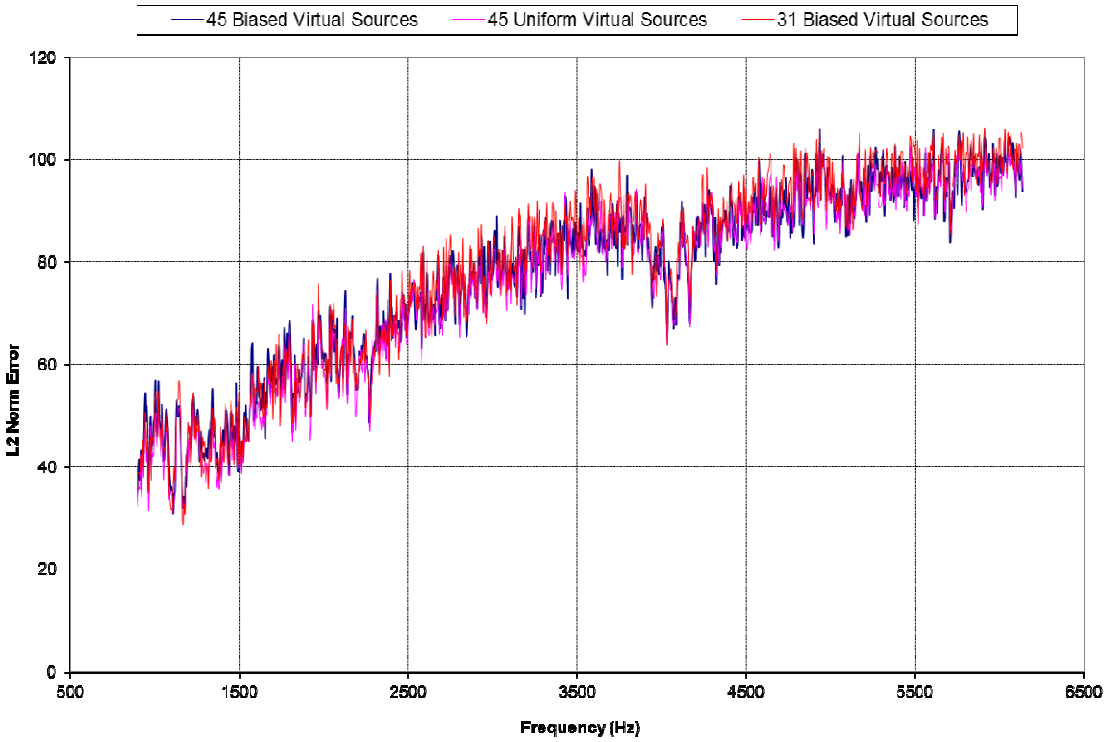

Figure 6.10: Comparison of $||L||^2$ norm errors for different virtual source distribution schemes.

As is evident from Figure 6.10, the $||L||^2$ norm error curves for different virtual source distribution schemes are nearly identical. Hence, any virtual source distribution scheme should yield reconstruction results similar to the others. For brevity, the scheme with 31 biased sources is chosen and results are presented henceforth based on this scheme.

6.4 Validating Modified HELS Acoustic Model

Once the virtual source distribution scheme is chosen, the acoustic pressure measurements around the jet plume are used to reconstruct acoustic pressures on the benchmark locations (Figure 6.6) perpendicular to the flow direction of jet plume. Note that these benchmark locations extend nearly 4.5 times the diameter of jet nozzle or

approximately 2.4m into the far-field. In addition, the acoustic pressures are also reconstructed back on to the measurement locations and compared to the measured acoustic pressures. If good comparison is achieved at these benchmark locations, the acoustic model based on modified HELS method will be considered validated.

Comparisons of measured and reconstructed acoustic pressures are made over the entire measurement surface at 1984 locations and on 124 benchmark locations perpendicular to the flow direction over the frequency range of 917Hz to 5168Hz in 1/24 octave bands. For brevity, a few of those comparisons are shown below. Figures 6.11, 6.12 and 6.13 show comparison of measured and reconstructed acoustic pressures at microphone numbers 6, 20, and 24 for 9th measurement patch.

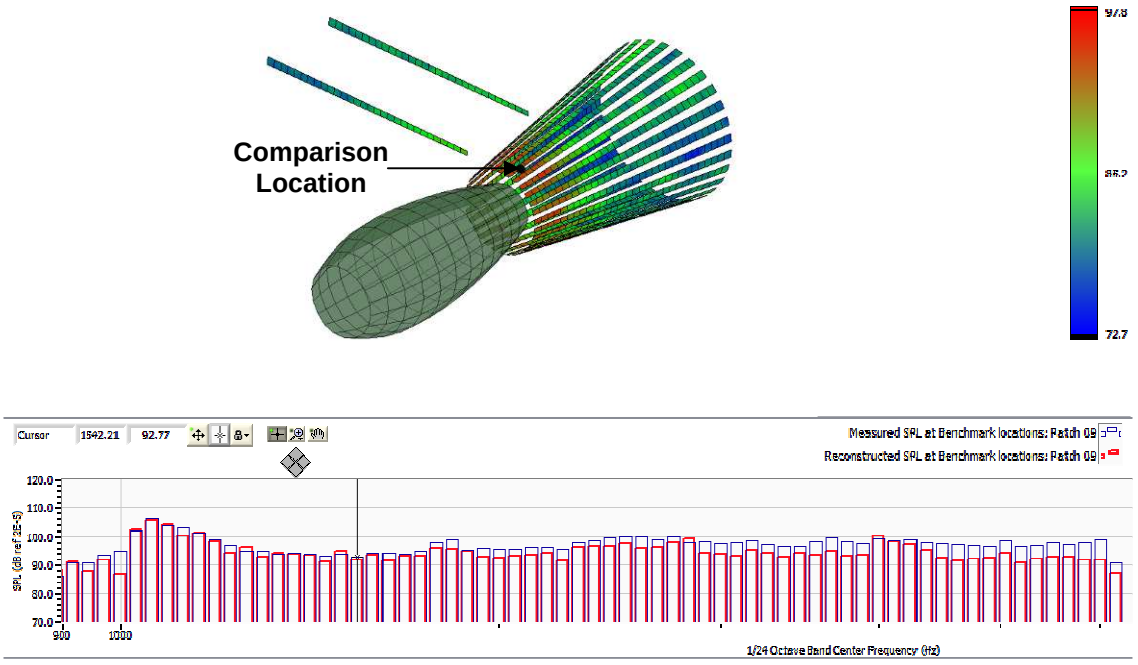

Figure 6.11: Comparison of measured and reconstructed acoustic pressures at field microphone location #6 on measurement patch # 9.

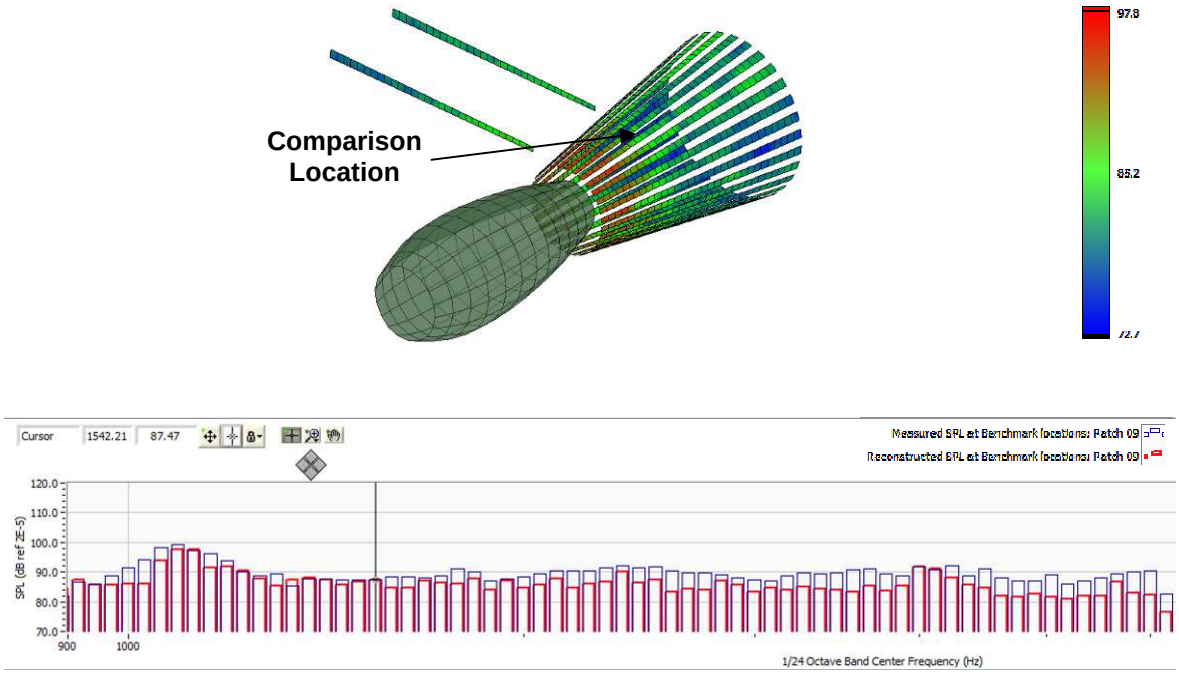

Figure 6.12: Comparison of measured and reconstructed acoustic pressures at field microphone location #20 on measurement patch # 9.

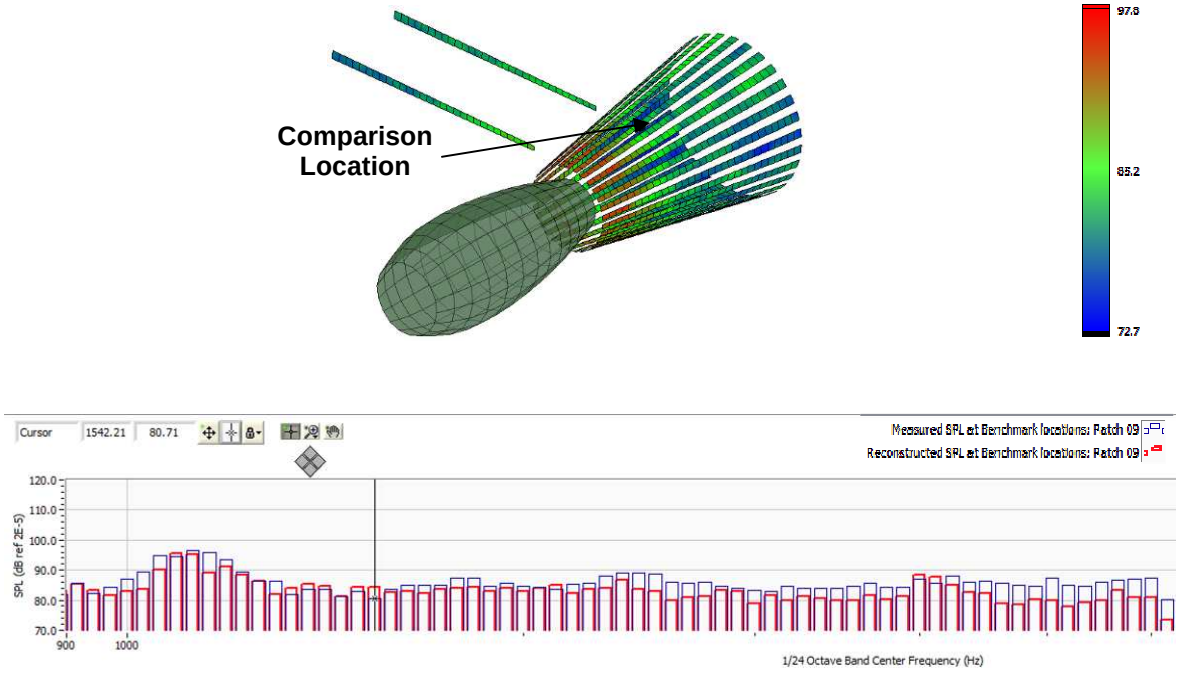

Figure 6.13: Comparison of measured and reconstructed acoustic pressures at field microphone location #24 on measurement patch # 9.

The comparisons of measureed and reconstructed acoustic pressures at field microphone locations are very good, especially in the low to mid frequency range. This means that the modified HELS based acoustic model is working and can be used next to reconstruct on the benchamark microphone locations peropendicular to the flow direction. Figures 6.14, 6.15, and 6.16 show comparison of measured and reconstructed acooustic pressures at microphone numbers 20, 28, and 61 of the benchmark microphone array I (Figure 6.6) closer to the jet nozzle.

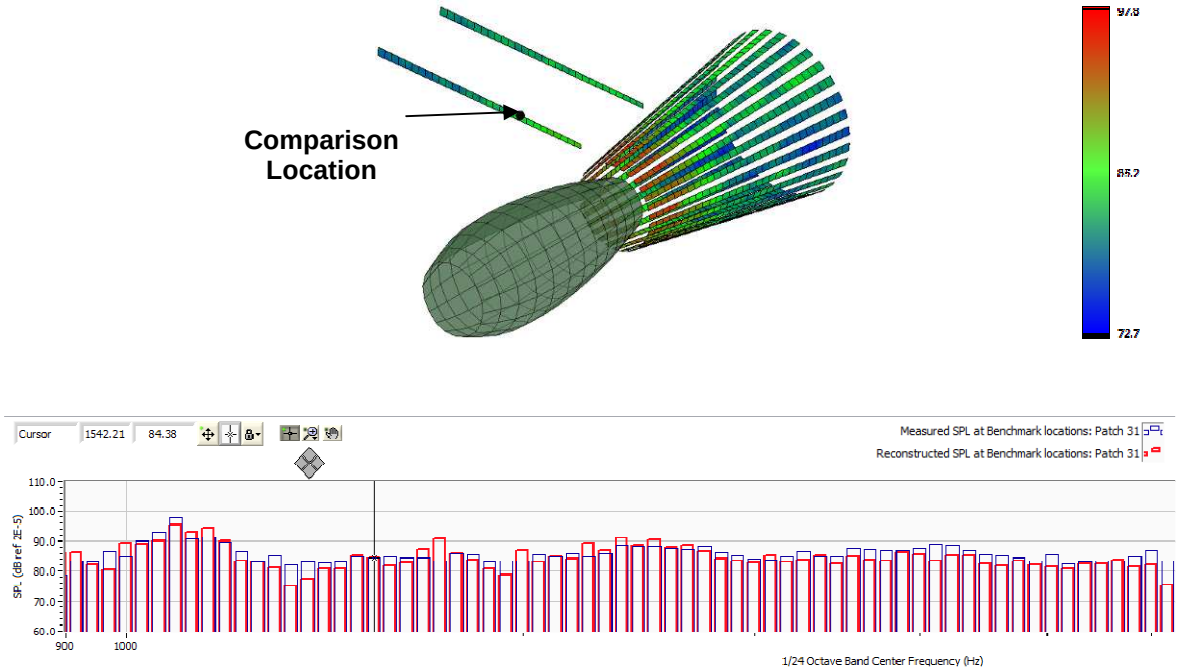

Figure 6.14: Comparison of measured and reconstructed acoustic pressures at microphone location #20 on the benchmark microphone array I closer to the jet nozzle.

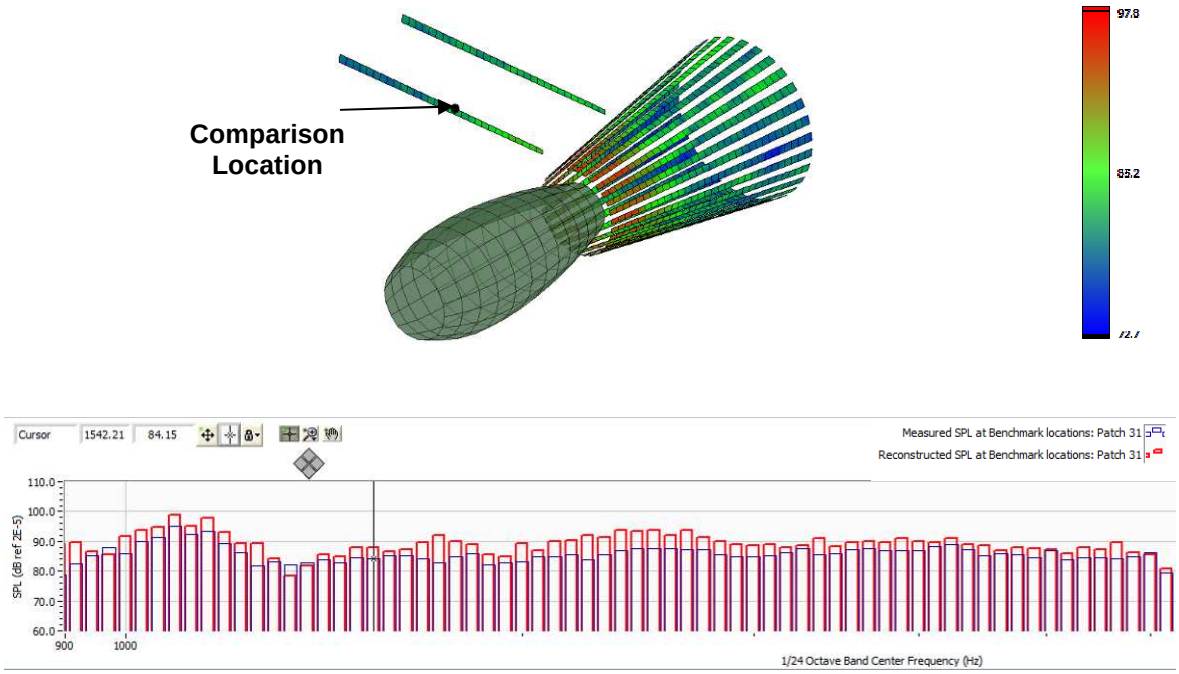

Figure 6.15: Comparison of measured and reconstructed acoustic pressures at microphone location #28 on the benchmark microphone array I closer to the jet nozzle.

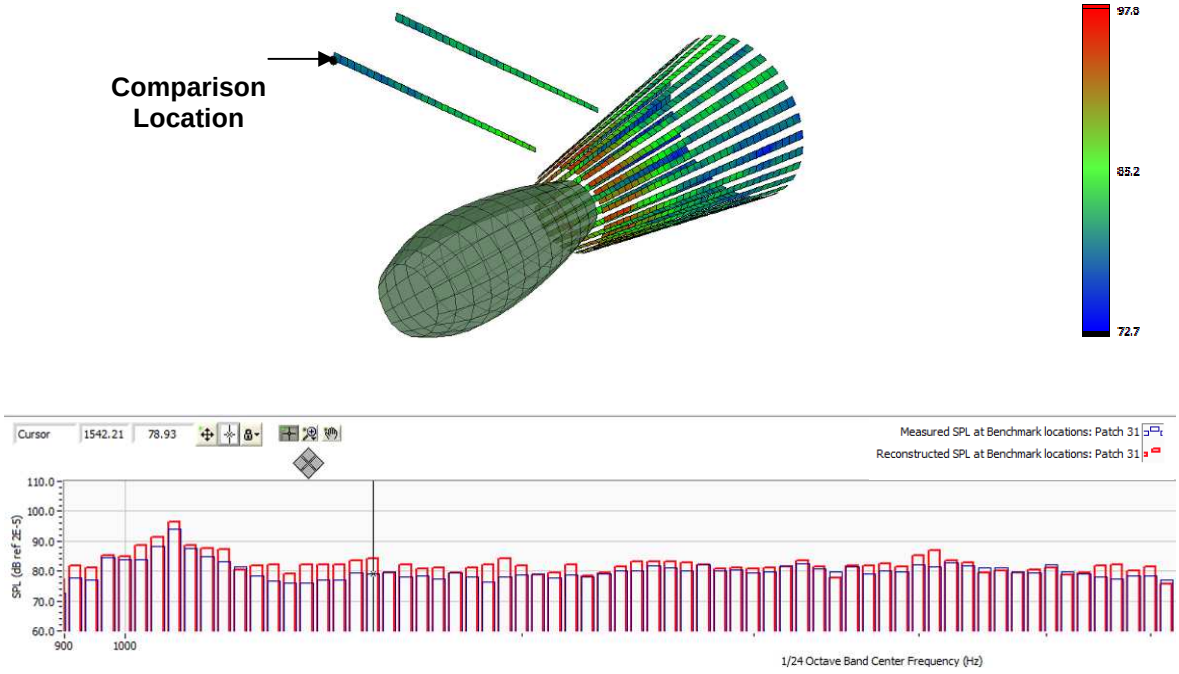

Figure 6.16: Comparison of measured and reconstructed acoustic pressures at microphone location #61 on the first benchmark microphone array closer to the jet nozzle.

As is evident from Figures 6.14, 6.15, and 6.16, the comparions for measured and reconstructed acoustic pressures are very good throughout the computed frequency range. Further, it should be noted that comparison quality is not affected and does not deteriorate with increasing distance from the jet nozzle along the perpendicular direction for the first benchmark location array. Acoustic pressure comparisons are also made at the benchmark array II (Figure 6.6) microphone locations. Figures 6.17, 6.18, 6.19, and 6.20 show the comparison of meaured and reconstructed acoustic pressures at microphone numbers 1, 10, 48, and 61, respectively.

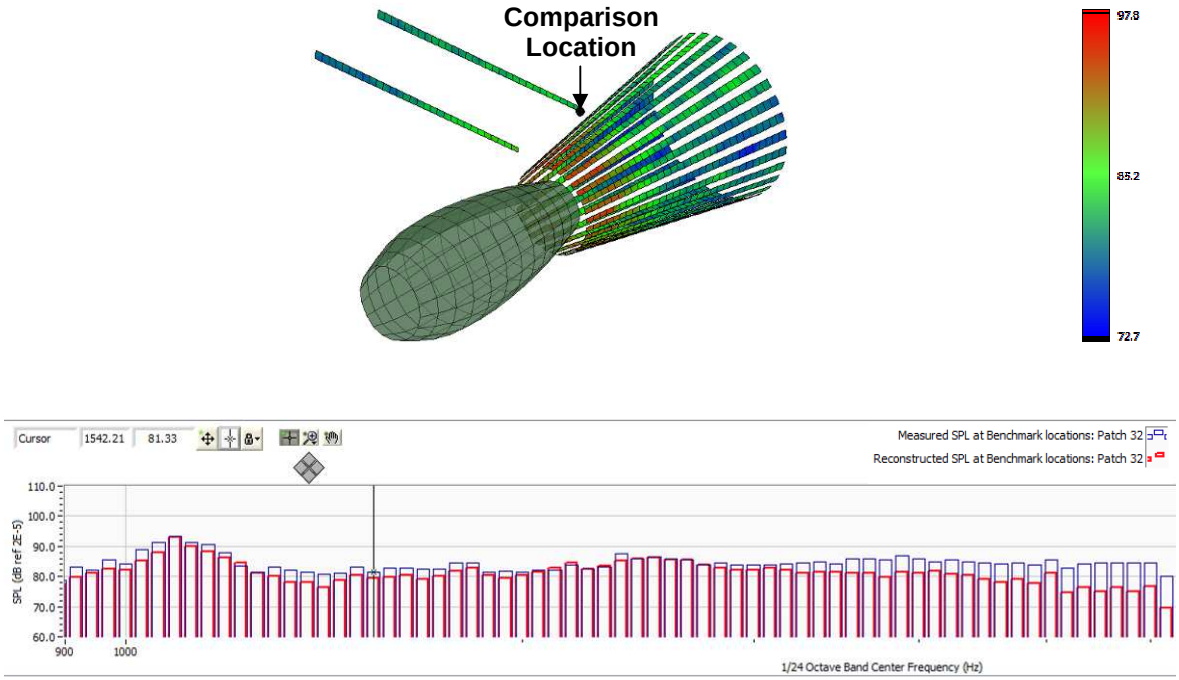

Figure 6.17: Comparison of measured and reconstructed acoustic pressures at microphone location #1 on the second benchmark microphone array father from the jet nozzle.

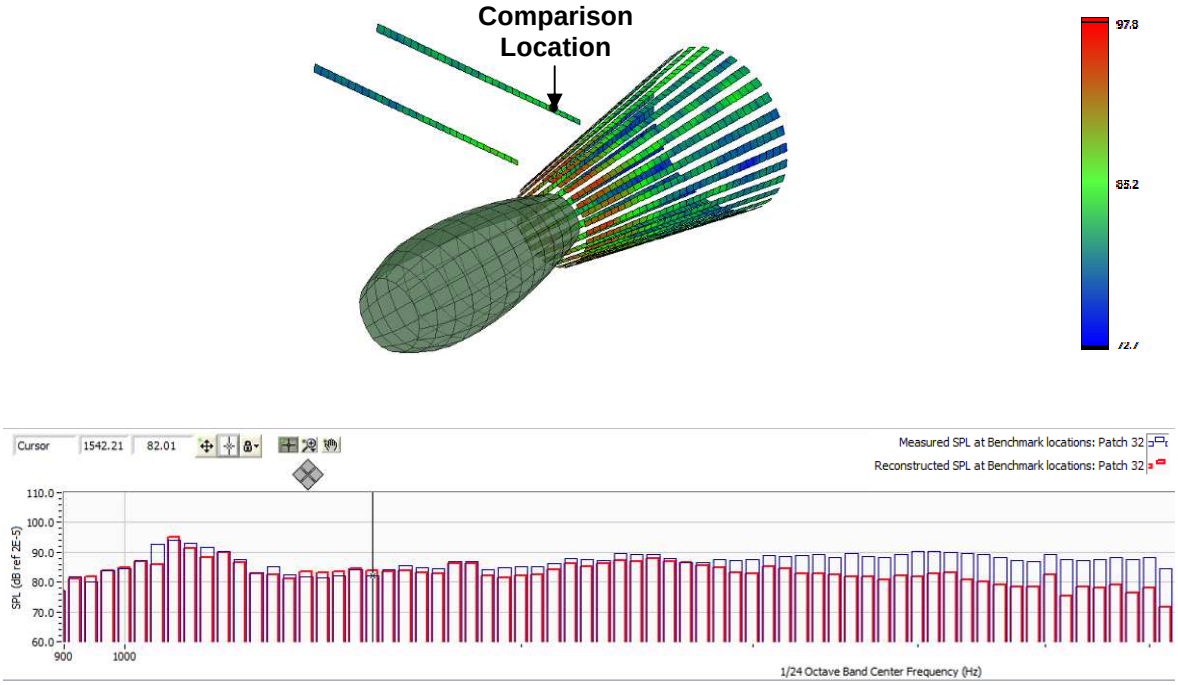

Figure 6.18: Comparison of measured and reconstructed acoustic pressures at microphone location #10 on the second benchmark microphone array father from the jet nozzle.

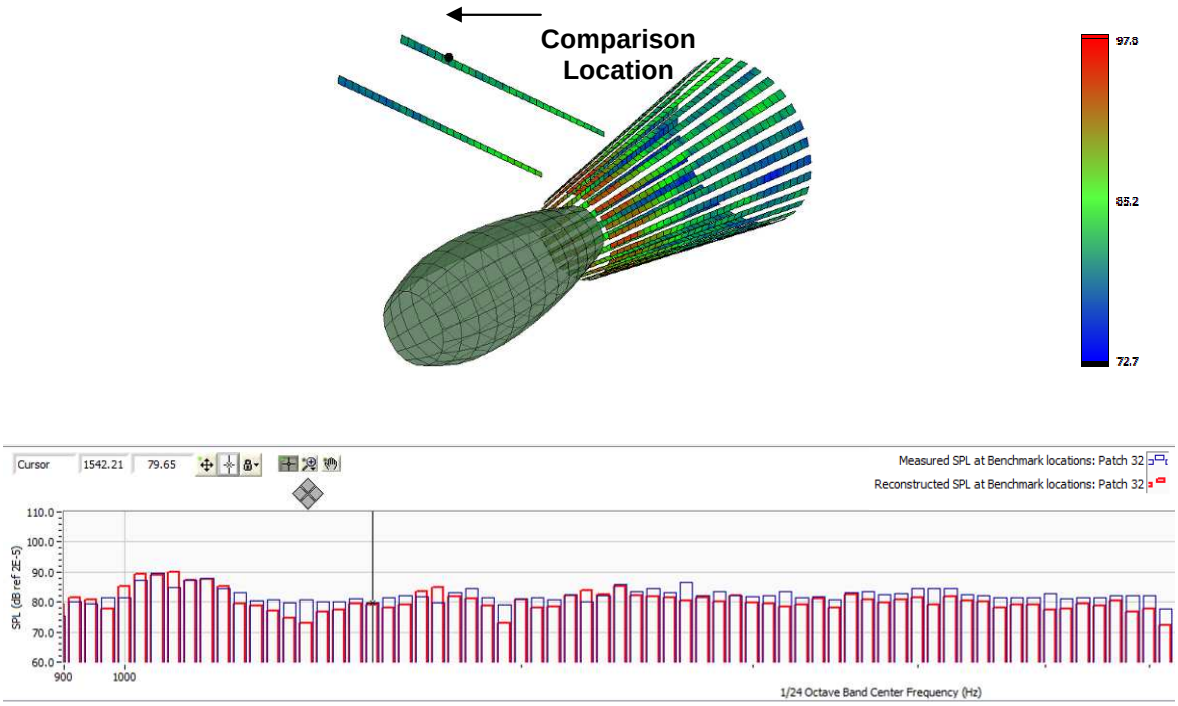

Figure 6.19: Comparison of measured and reconstructed acoustic pressures at microphone location #48 on the second benchmark microphone array father from the jet nozzle.

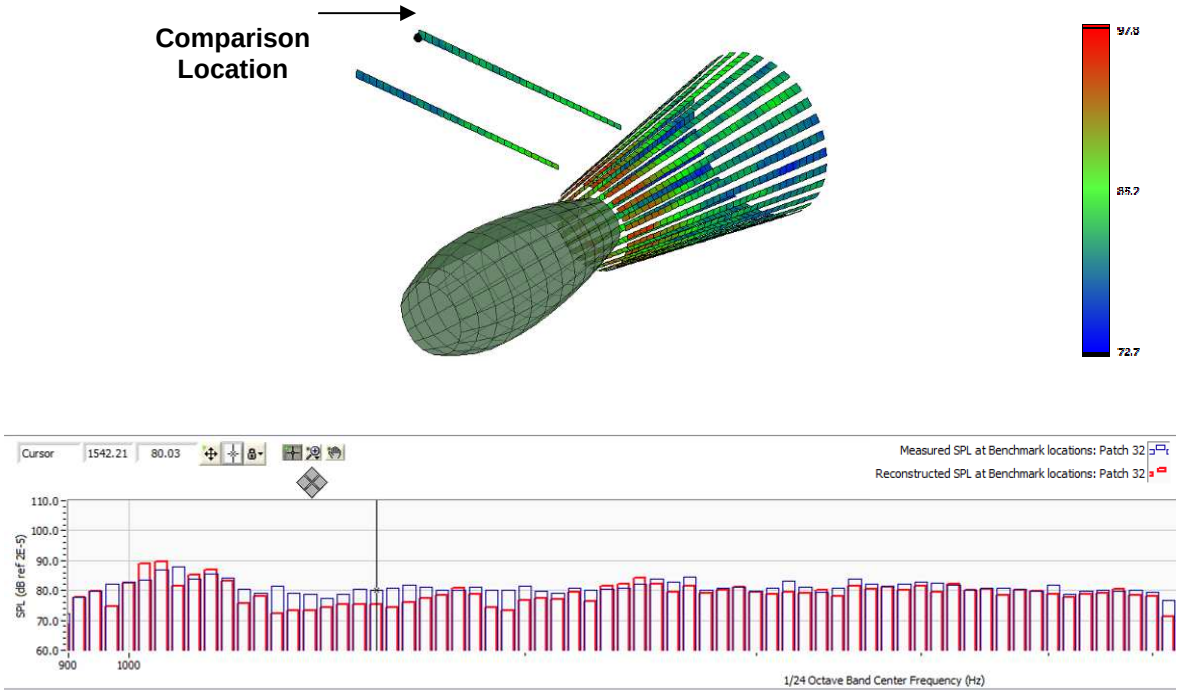

Figure 6.20: Comparison of measured and reconstructed acoustic pressures at microphone location #61 on the second benchmark microphone array father from the jet nozzle.

The comparison of measured and reconstructed acoustic pressures at benchmark array II (Figure 6.6) in Figures 6.17, 6.18, 6.19, and 6.20 look very promising and further validate the accuracy of acoustic model. Once again, the accuracy of reconstruction does not deteriote as much with distance in the perpendicular direction. Infact, closer the benchmark microphones are to the jet plume, less accurate is the reconstructed acoustic pressures in the frequency bands from 3268Hz to 6168Hz. The reconstructed pressure in these bands diverges from the meaured acoustic pressures with increase in frequency (Figures 6.17 and 6.18). This could be because only monopoles and dipoles are used to create the acoustic reconstruction model and they are not enough to appropriately account for contribution from quadrupoles at higher fequencies in the near-field of jet plume. For

the scope of this investigation, only reconstructioin with monopoles and dipoles is performed. Reconstruction with quadrupoles will be conducted in the future.

6.5 Reconstruction of Acoustic Field inside the Jet Plume

It is emphasized that the proposed approach seeks to acquire the best approximation of an acoustic field resulting from a turbulent flow ejected from a jet nozzle, because the exact solution cannot be found. As such, our mathematical model may not be perfect and may not account for all fluid dynamic effects. For example, the turbulence eddies may expand and drift at a high speed after exiting the nozzle, and a high Mach number will change the sound field. These effects can be accounted for if particle velocities and hydrodynamic pressures are measured or are available as input. Therefore, we decide to distribute a set of virtual sources inside a jet plume to describe an overall sound field generated by a jet engine.

It must be noted that in the current investigation, the jet engine was run only at idle speed and Mach numbers are significantly lower. This gives us an opportunity to reconstruct within the jet plume by assuming low Mach numbers and minimal fluid dynamic effects. Also, we may not need to take particle velocity and hydrodynamic pressure measurements in the jet plume.

Once the modified HELS-based NAH technique was validated (Subchapter 6.4), the sound field inside and outside the jet plume in the downstream direction were calculated. In this case, we covered the sound field to 17 times the diameter of the jet nozzle, consistent with most studies in turbulent flows even for a supersonic jet. In particular, we sliced across the jet plume to visualize the source strength distributions

inside the jet plume. Note that we can slice across the jet plume at any angle with any increment in the azimuthal direction. This enables us to acquire a better understanding of the acoustic characteristics of the jet plume and their source strength distributions. Figure 6.21 shows one such slice through the jet plume that extends to 17 times the diameter of jet nozzle.

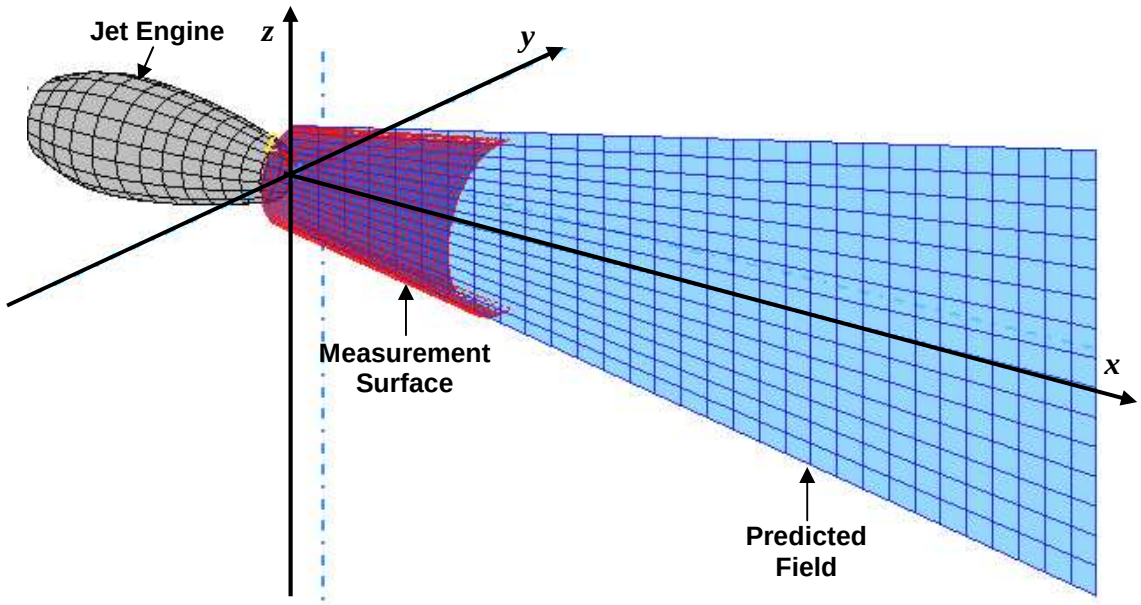

Figure 6.21: Schematic of jet nozzle, measurement and prediction regions.

The 1984 acoustic pressure measurements are then used to reconstruct on four slices through the jet plume. Figures 6.22, 6.23, 6.24, 6.25, 6.26, and 6.27 show acoustic pressure distribution on one slice through the jet plume for 1060Hz, 1122Hz, 1682Hz, 2378Hz, 4000Hz, and 5656Hz center frequency 1/24 octave bands, respectively.

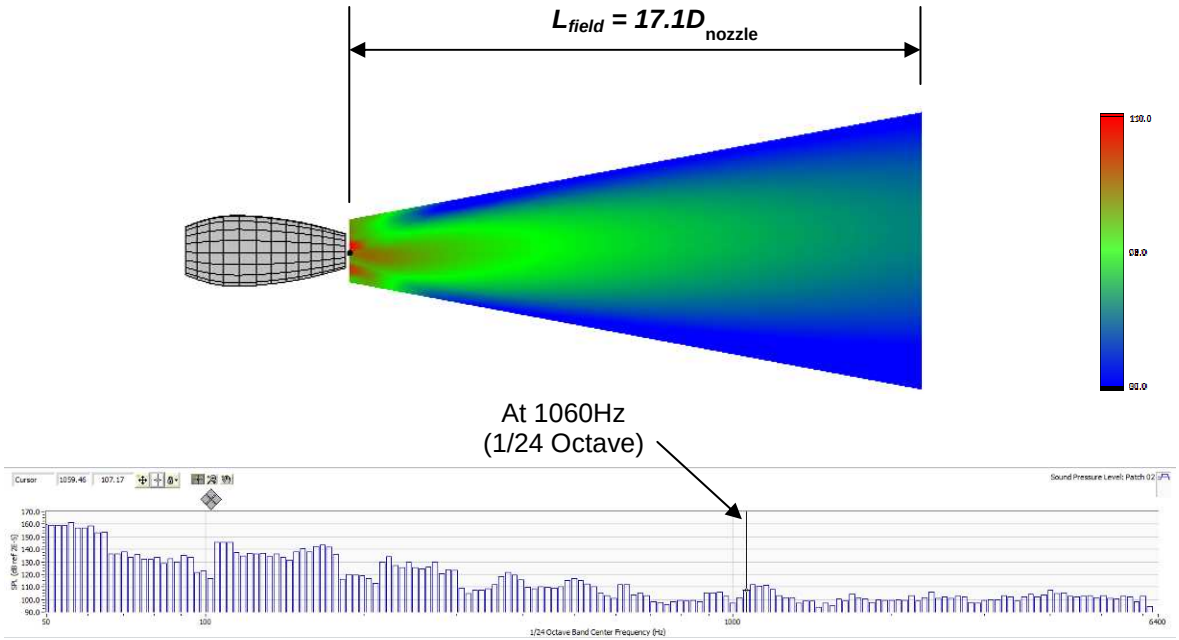

Figure 6.22: Visualization of acoustic pressure distribution of jet plume at 1060Hz center frequency 1/24 octave band.

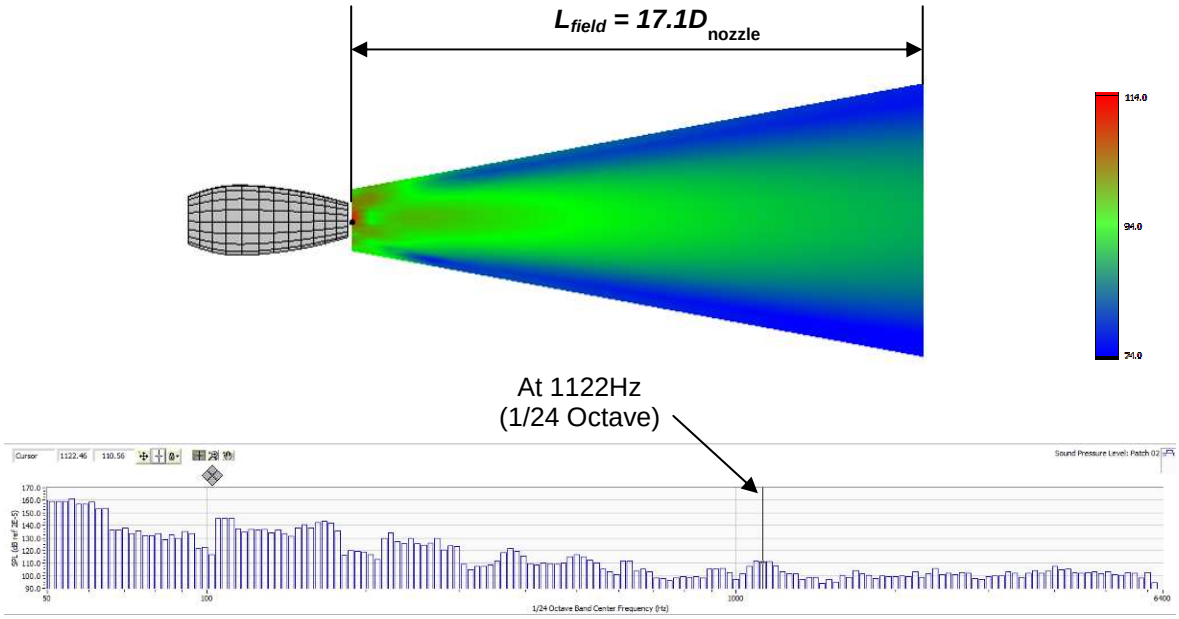

Figure 6.23: Visualization of acoustic pressure distribution of jet plume at 1122Hz center frequency 1/24 octave band.

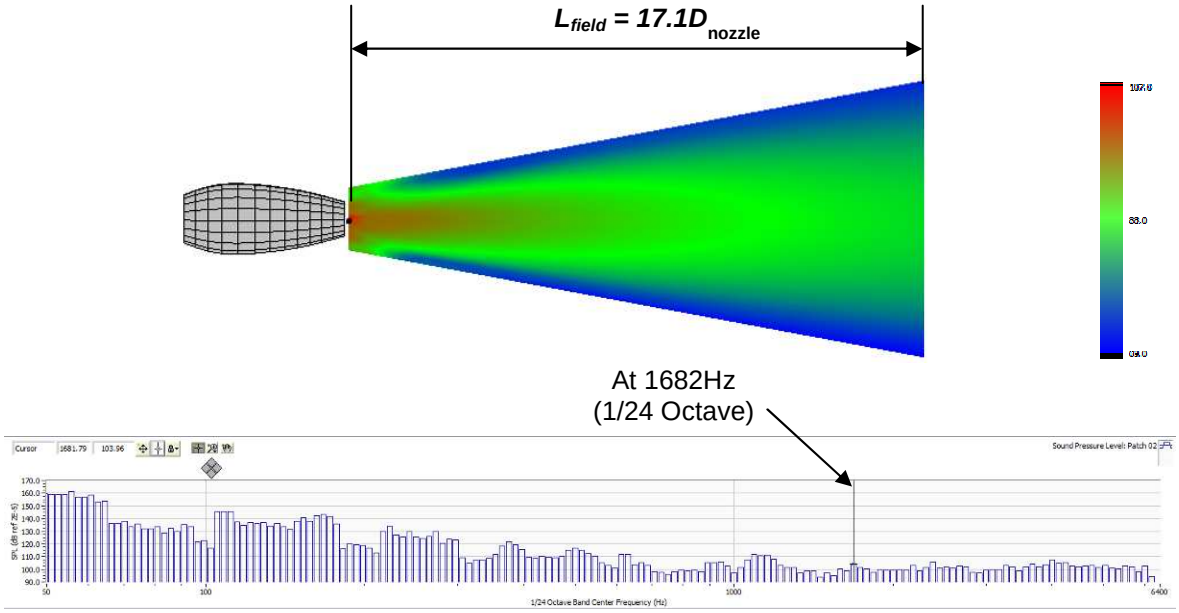

Figure 6.24: Visualization of acoustic pressure distribution of jet plume at 1682Hz center frequency 1/24 octave band.

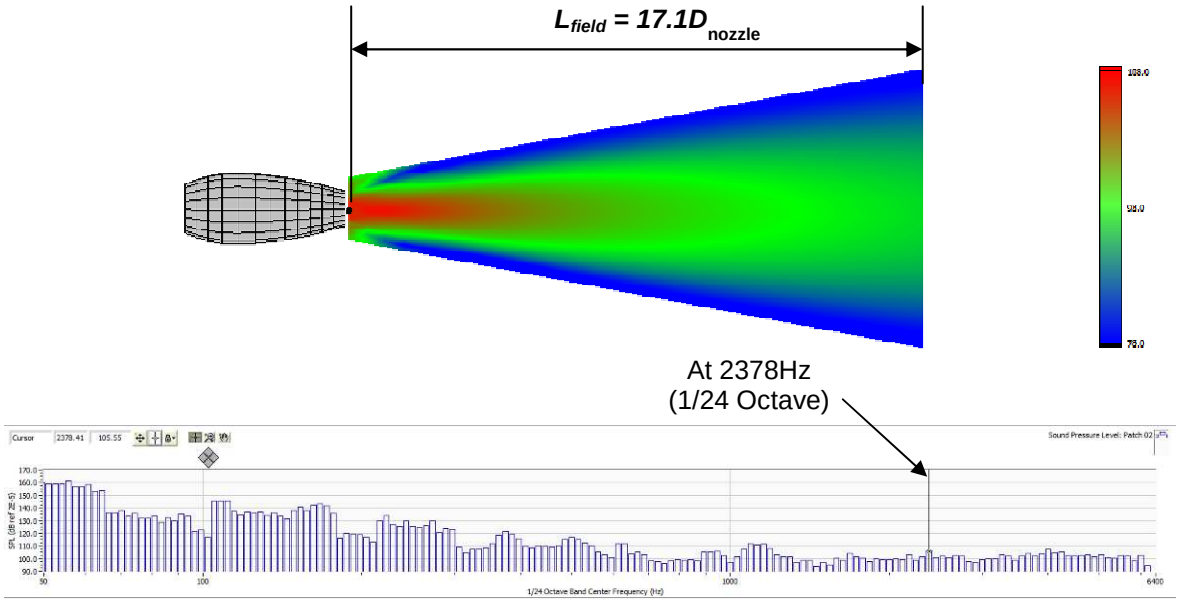

Figure 6.25: Visualization of acoustic pressure distribution of jet plume at 2378Hz center frequency 1/24 octave band.

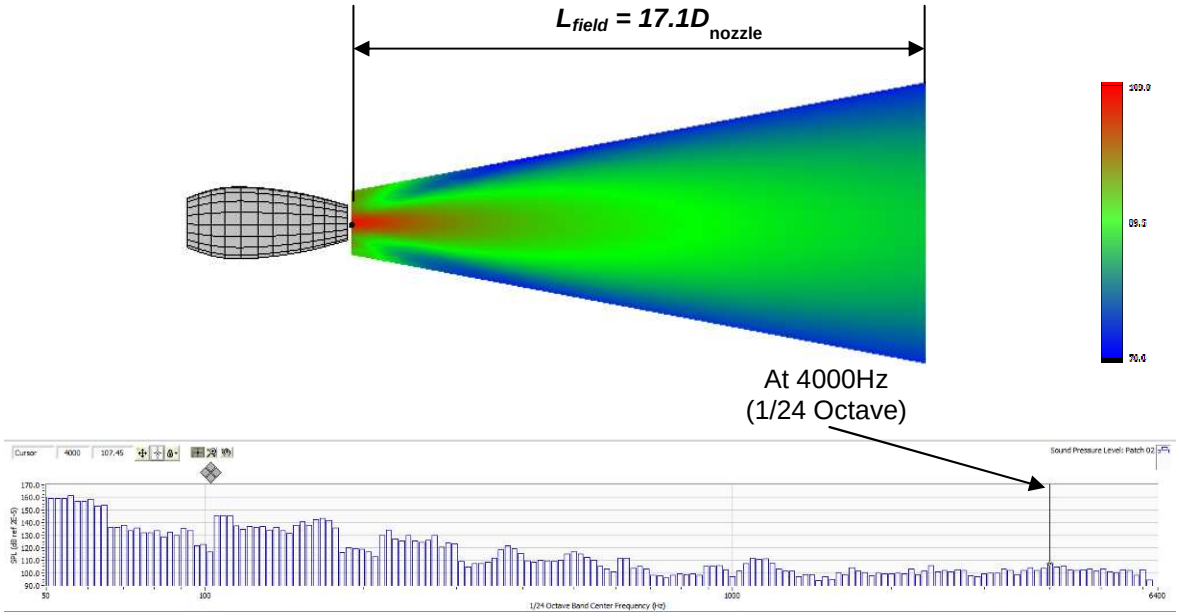

Figure 6.26: Visualization of acoustic pressure distribution of jet plume at 4000Hz center frequency 1/24 octave band.

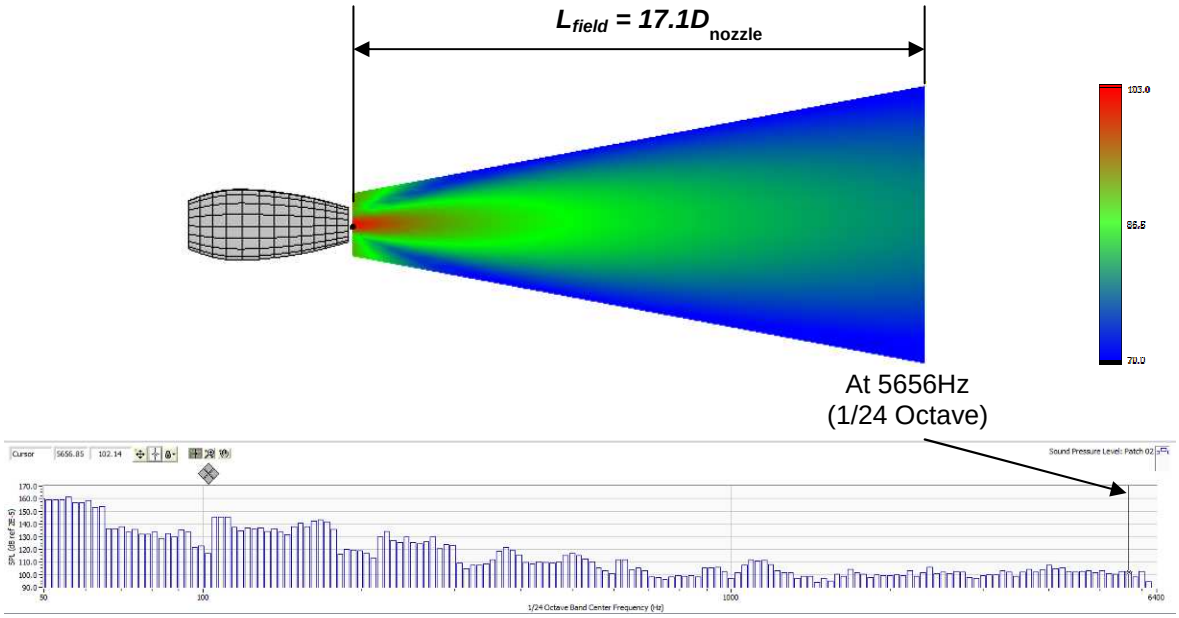

Figure 6.27: Visualization of acoustic pressure distribution of jet plume at 5656Hz center frequency 1/24 octave band.

The acoustic pressure distribution predictions seem to be plausible and seem to represent expected flow in the jet plume but there is no data available to validate them. The solution could be to compare predicted data to simulation data created by other researchers. Time-averaged Streamwise velocity contours in vertical plane, from Eastwood and Tucker[65] (Figure 6.28), show excellent similarity to the acoustic pressure field reconstructed by using the modified HELS formulations.

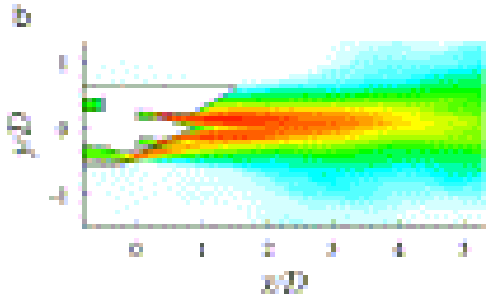

Figure 6.28: Time-averaged streamwise velocity contours in vertical plane, from Eastwood and Tucker[65].

The methodology was further applied to 3 more slices within the jet plume and acoustic pressure distributions were reconstructed. For brevity, visualizations on all 4 slices through the jet plume, for only two frequency bands are depicted. Figure 6.29 and 6.30 show reconstruction results for center frequencies of 1060Hz and 5656Hz 1/24 octave bands. It should be noted that, reconstruction results for all 4 slices are calculated in only one computation and not 4 different computations for individual slices.

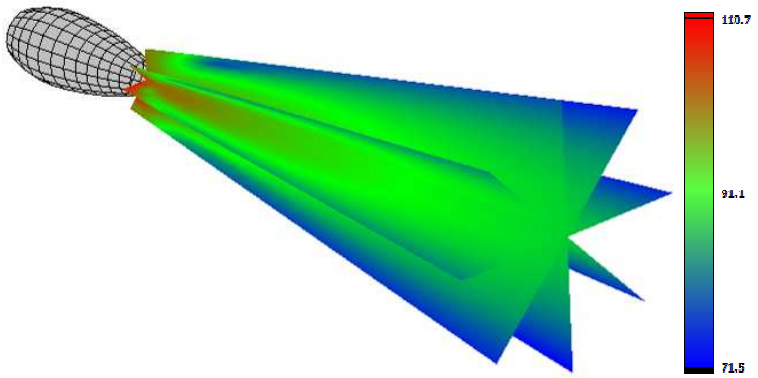

Figure 6.29: Visualization of acoustic pressure distribution over 4 slices through jet plume at 1060Hz center frequency 1/24 octave band.

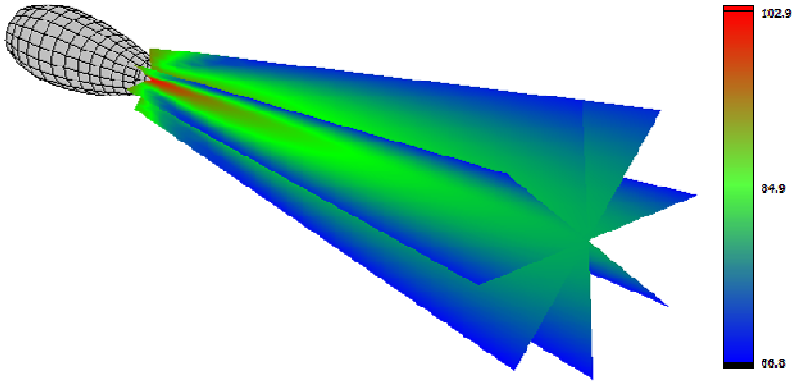

Figure 6.30: Visualization of acoustic pressure distribution over 4 slices through jet plume at 5656Hz center frequency 1/24 octave band.

This investigation shows that acoustic characteristics of jet plumes be depicted adequately by superposition of distributed monopoles, dipoles, and quadrupoles. Results demonstrate that the HELS-based NAH technology allows for visualization of the acoustic characteristics of a jet plume such as the extent and directions of major and side lobes. Since the measurements were taken around the jet plume, we could visualize the acoustic characteristics of a jet plume on any cross section in the azimuthal direction.

6.6 Future Work

The significance of the current research cannot be overstated because it yielded an insightful understanding of the acoustics characteristics of jet plumes that cannot be offered by conventional technologies. Comparing to all other related technologies, the proposed modified HELS technology and its implementation seem to be uniquely suited for analyzing the acoustics characteristics of a jet plume. The modified HELS based NAH technology enables one to distribute any number of virtual sources of any type at any location to describe an aerodynamically generated sound field. It allows for visualizing the source strengths even inside the core plume based on the acoustic pressures measured outside the plume.

It is the author's belief that current application of modified HELS method has laid a solid foundation for future work. Any further research should be directed towards the following aspects to enhance the accuracy in analyzing the acoustics characteristics of jet plumes.

1. Implementation for supersonic jet engines: Current setup has been implemented for a subsonic jet engine. The next step should be to design a test setup with high dynamic range and high maximum pressure limit microphones to implement this methodology for supersonic jet engines.
2. Implementation of Modified HELS method for instantaneous acoustic pressure reconstruction: Current investigation uses a 62 microphone array to take 1984 measurements around the jet plume. This is only possible because of the assumption that the jet plume is populated with steady/stationary sources. In

reality, however, the turbulence eddies inside the plume may expand and drift at a high speed after exiting the nozzle, and a high Mach number will also change the sound field. To capture and reconstruct these transient events within the jet plume, one will need to take a large array of microphones that can cover the jet plume in one measurement.

3. Improving the computation efficiency in the high-frequency regime: It will be helpful to modify the HELS formulations so as to facilitate broadband reconstruction. This will greatly speed up the efficiency of numerical computation for analyzing jet noise up to 30 kHz.
4. Extending to moving NAH: Modify the HELS formulations to account for a source convection motion. This is especially important in describing of a sound field from a high-speed airflow as the high Mach number will greatly change a sound field.
5. As shown in the case study of propeller noise test discussed above, the modified HELS formulation was able to reduce the effect of reflections from ground. With lessons learnt from this research future researchers may need to modify it further to extend the methodology to include the effects of typical features of an aircraft carrier deck, such as a Jet Blast Deflector (JBD) and superposition of multiple jet streams.
6. Optimize the number of input data points needed during this investigation and develop a practical prototype procedure/methodology that can be implemented with minimum effort and yield accurate source characterization.

7. Optimizing Virtual Source Locations and Number: The proposed technology signifies an extension of the HELS method that can account for contributions from different sound generation mechanisms such as monopoles, dipoles, quadrupoles, and enable one to distribute these virtual sources anywhere in the space. The locations of the virtual sources can be optimized to best approximate a sound field produced by a target source. In the current investigation, only three different virtual source schemes were implemented that seemed to be appropriate approximation for sources in a slow speed jet plume. In practice however, the algorithm should be able to identify an optimal virtual source distribution scheme automatically. An iterative process can be used to achieve this. For example, we take a set of virtual sources on a surface Γ, use the modified HELS formulation to reconstruct the acoustic pressures at the measurement points, and minimize reconstruction errors with respect to measurement data by using least squares. Next, we change the locations of the virtual sources and repeat the reconstruction process and carry out the iteration steps until the errors is minimal. The resultant locations of the virtual sources are said to be optimized with respect to the set of collected data.

APPENDIX-A: HARDWARE COMPONENTS OF THE HELS SYSTEM

A.1 Introduction

The HELS method has proved to be an extremely flexible nearfield acoustic holography tool in the numerical validations carried over the interior surface of a vibrating cavity. The experiments carried out in the exterior region during initial stages of development have also validated the viability and accuracy of the HELS methodology13. Though, the data acquisition has been painstaking and cumbersome. Thus, the onus lies on carving out a set of hardware apparatus that matches the functionality of this methodology and at the same time keeps the costs low.

Keeping this in mind, a hardware scheme was developed for application of the HELS method to engineering problems. This system may be divided into four major subsystems. These are:

1. 3D Sonic Digitizer for acquiring the coordinates of the field microphones.

2. A 64-microphone array to gather the acoustic field information along with the sensor signal conditioners that provide signal conditioning and anti-aliasing filtering.

3. Data acquisition modules for processing the analog microphone signals and storing the acoustic pressure data onto the computer hard disk.

4. The software components: the HELS program, that processes the acquired acoustic pressures to compute the unknown acoustic parameters at the

desired locations, and post-processing software packages for better visualization of the computed results.

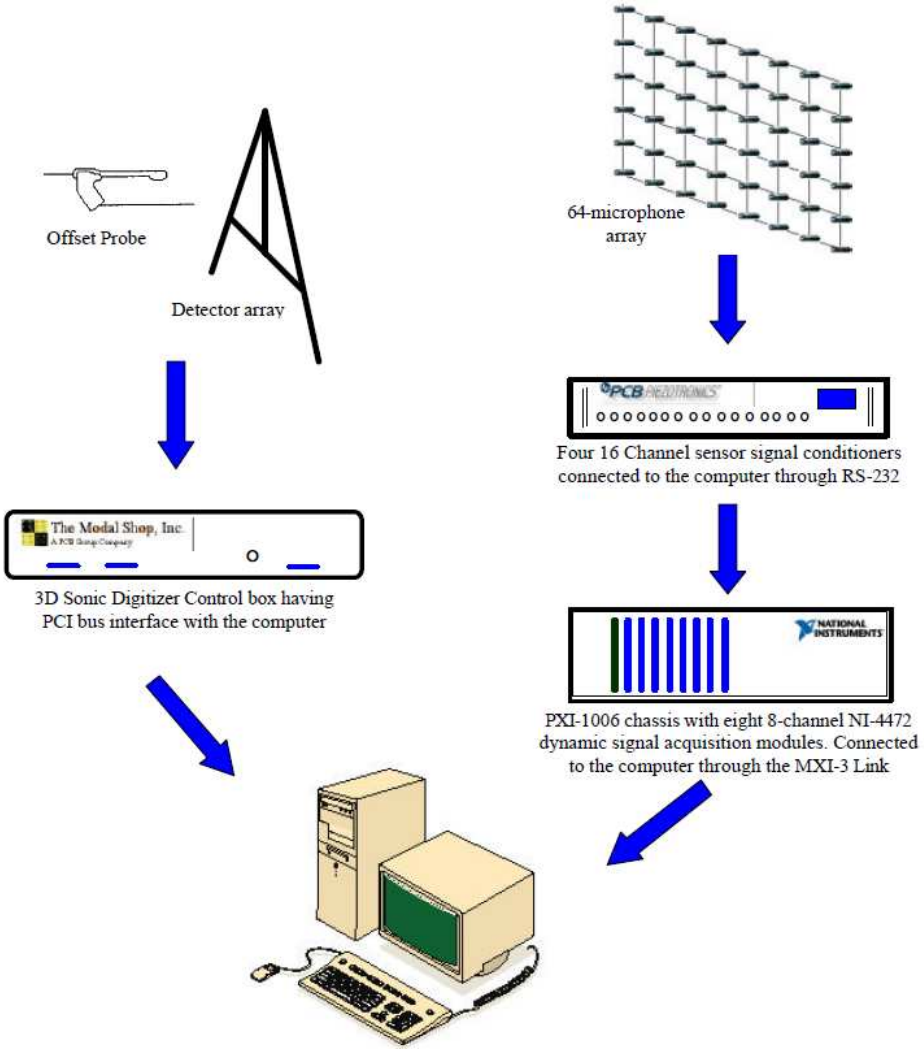

Figure A.1: Schematic of the hardware components of the HELS system and data flow.

A.2 3D Sonic Digitizer for Acquiring Field Microphone Coordinates

Sonic digitizers measure the time delay between an impulse from a sound emitter and the detection of the signal by a sound receiver. If the speed of sound is known or measured, then the distance between the emitter and the receiver is simply the time delay multiplied by the speed of sound. If a sound wave travels from a single emitter to three or more receivers of known orientation, and the speed of this sound wave and the time

duration between the emitter and each receiver are known, then it is possible to calculate the location of that emitter in three-dimensional space.

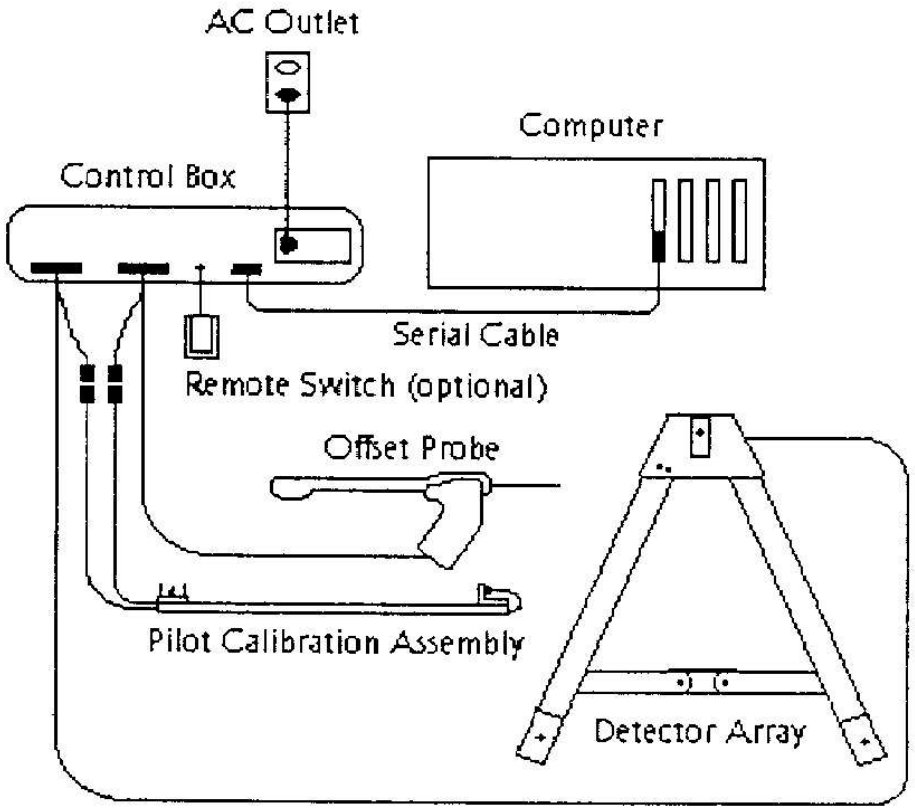

Figure A.2: Schematic of the 3D Sonic Digitizer components.

While the sonic digitizer offers the advantage of being able to digitize any material, including metals, there are some practical limitations that need to be observed. Every emitter/receiver combination being used requires a direct line of sight. In other words, an object directly between an emitter and any receivers listening to the emitter will disrupt the digitizing process. Thus, the probe emitters must face the detector array.

The higher the degree to which the speed of sound is measured, the higher the level of digitized accuracy will be. The 3D Sonic Digitizer supports two types of real-

time speed of sound compensation. These methods measure the speed of the digitizing environment at the time of digitizing (real time):

- *Probe compensation* works well in 1 Meter Mode volumes and requires less hardware that the following pilot method. Probe compensation relies on knowing the distance between the two probe emitters and interactively adjusting the speed of sound until the digitized distance between the emitters is correct.

- *Pilot compensation* is more accurate, particularly in larger volumes, than probe compensation. Present experimental setup uses pilot compensation for calculation of speed of sound. Pilot compensation uses an emitter fixed at a calibrated distance from a receiver. Each time the offset probe is digitized, the pilot distance may also be digitized allowing calculation of the current speed of sound. It should be noted that differences in the speed of sound between the calibration bar location and the offset probe location due to thermal gradients or other factors can influence the accuracy of the compensation method.

The schematic in Figure A-2 shows the components of the 3D Sonic Digitizer system.

A.3 ICP® Microphone Cartridge Model No. TMS130C10 and Pre-Amplifier Model Nos. TMS130P10 & TMS130P11

The ICP® Microphone Cartridge employs an electric condenser microphone as its sensing element. The 130C10 mates with the 130P10 and 130P11 preamplifiers by a 10-32 microdot connection. The outputs of 130P10 or 130P11 is wired to an intermediate patch panel and then to the ICP® sensor signal conditioner. The nominal microphone sensitivity is 25 mV/Pa. The complete list of technical specifications is provided in Table A.4. For this study the TMS 130P10 was used as the pre amplifier.

Figure A.3: The ICP® Microphone Cartridge Model No. TMS130C10 and Pre-Amplifier Model No. TMS130P10.

Response:	Free-field
Nominal Microphone sensitivity at 250 Hz (±25%)	25 mV/Pa
Frequency response characteristics: ±1 dB Guaranteed ±1 dB Typical ±1 dB Typical	 100 Hz to 4 kHz 20 Hz to 7 kHz 10 Hz to 15 kHz
Directivity:	Omni directional
System dynamic range: Lower limit (1/3 octave at 1 kHz): Lower limit (Lin spec, 10 Hz-10 kHz): Upper limit (3% linearity): Upper limit (Saturation):	 < 15 dB < 35 μV_{rms} > 128 dB > 132 dB
Sensor impedance:	< 10 Ω
Temperature range:	-10 to 65 deg C (15 to 150 deg F)
Temperature effects at 250 Hz (-10 to 65 deg C):	< ±0.5 dB
Vibration sensitivity at 250 Hz (1 m/s^2 axial):	< 53 dB

Figure A.4: Features and technical specifications of ICP® Microphone Cartridge Model No. TMS130C10 and Pre-Amplifier Models No. TMS130P10 & TMS130P11.

A.4 Microphone Data Acquisition (An Introduction to PXI)

The primary concern for any data acquisition system is its interface with a computer. A better interface leads to better data interpretation and acquisition capabilities. PCI (Peripheral Component Interconnect) devices seem to provide the best solution for low channel data acquisition. On the other hand, for high channel data acquisition, due to low count of PCI buses on the standard desktop computers the use of conventional PCI devices is prohibitive. Thus, for high volume data handling, a more robust, and preferably, a standalone device is required for a diminished burden on the computer hardware structure. The solution is presented by PCI eXtensions for Instrumentation (PXI). PXI modular instrumentation delivers a PC-based, standardized,

high-performance measurement and automation system. Some obvious advantages of PXI instrumentation are:

- Superior software and hardware integration
- Widest selection of measurement hardware -- DAQ, instruments, vision, and motion
- Real-time performance with LabVIEW Real-Time
- Lower overall system costs

A.4.1 PXI Chassis

The major component of a PXI system is the PXI chassis that can hold the standard PXI/CompactPCI modules from hundreds of vendors. Limiting this discussion to the present study, the general purpose NI PXI-1006 chassis manufactured by theNational Instruments was used as the base of the data acquisition system. Figure A.5 shows a PXI-1006 chassis with different measurement modules. The major features and specifications of this chassis are as follows:

- Full-featured 18-slot chassis for high-module-count applications.
- 3U PXI and CompactPCI modules accepted
- Multiple power supply options
- Optional battery backup
- Remote power inhibit and monitoring.

Figure A.5: A representative photograph of an 18 slot PXI-1006 chassis.

A.4.2 Data Acquisition Modules

The Dynamic Signal Acquisition Cards, NI-4472, were used as the measurement modules fitted inside the PXI-1006 chassis. A picture of one of the cards is shown in Figure A.6. A total of 8 NI-4472s equivalent to a 64-channel data acquisition platform were used for this investigation. The main features and specifications of the NI-4472 Dynamic Signal Acquisition module based PXI system are as follows:

- 64 simultaneously sampled analog input channels (with 8 modules)
- 24-bit resolution
- 120 dB dynamic range
- AC/DC coupling
- NI-DAQ software for Windows 2000/NT/Me/9x

The NI PXI-4472 is combined with the Sound and Vibration Toolset provided by the National Instruments to perform accurate frequency measurement analysis.

Figure A.6: An 8-channel PXI NI-4472 Dynamic Signal Acquisition module.

A.4.3 MXI-3 Link for PC Control of PXI Chassis

MXI-3 is a new technology that brings the fastest and most flexible PC extension technology to PXI/CompactPCI. MXI-3 gives PCs direct control of PXI/CompactPCI via a software and hardware transparent link with speeds approaching 100 Mbytes/s over distances up to 200 meters. Thus, you can now use a PC instead of an embedded computer to control your PXI/CompactPCI modules, reducing your overall system cost. The same technology extends existing PXI/CompactPCI systems to secondary chassis providing more available slots for I/O.

The PXI-PCI-8330 series kit includes one half size PCI-8330 plug-in board, which is installed on the computer; one 3U-size PXI-8330 module, which is installed in the PXI/Compact PCI chassis; and a flexible MXI-3 cable. The MXI-3 cable serves as a link between the PC and the PXI/compact PCI system. Figure A.7 shows the major components of the MXI-3 link and how it is connected to the computer and a PXI chassis.

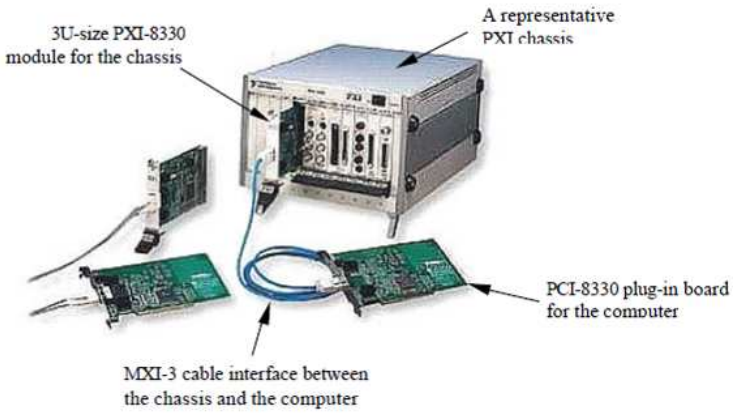

Figure A.7: The major components of the MXI-3 link and how they are connected to the PXI Chassis and the computer terminal.

A.5 Calibration of Microphones

Different calibration instruments were used for calibrating the microphone analog output and also the phase of the microphones with the reference signal (white noise in this case).

A.5.1 G.R.A.S. Pistonphone Type 42AA

The type 42AA (Figure A.8) is a precision sound source for calibration of microphones. The pistonphone is battery operated and produces a constant sound pressure level of 114 dB equal to 10 Pa at 250 Hz or 105.4 dB(A). All 42AA are within 0.1 dB from the nominal value and are delivered with individual calibration chart. The pistonphone includes barometer for class 1 static pressure corrections. For class 0 static pressure corrections a precision barometers is needed. The pistonphone can be used both for field checks of complete measurement systems and for laboratory calibration of measurement microphones. The features and specifications are given in Figure A.9.

Figure A.8: G.R.A.S Pistonphone type 42AA and Octopus adapter type RA0025.

Sound pressure level:	114dB (re. 2*10-5 Pa) 0.08 dB (individually calibrated)
Frequency:	250 Hz
Temperature Range:	-10°C to +55°C
Batteries:	4 x AA alkaline (IEC LR 6)
Accuracy:	IEC 942 (1988) Class 1
Weight:	325 gm

Figure A.9: Features and technical specifications of G.R.A.S Pistonphone type 42AA.

A.5.2 Larson Davis Model CAL 291 Residual Intensity Calibrator

The accuracy of the reconstruction is strongly dependent upon the phase measurement accuracy between field microphones and the reference signal. No phase measuring devices are available but an intensity calibrator may serve the required purpose. For direct calibration or verification of the accuracy of a sound intensity measurement system, IEC 1043 and ANSI S1.9 call for the use of a sound intensity calibrator which delivers to the probe microphones the simulated intensities at a specified temperature, atmospheric pressure and nominal microphone separation. For this investigation, phase difference between the reference (white noise) signal and the probe microphones was measured using the intensity calibrator and stored in ASCII format to

be used by LabView VIs (Virtual Instruments) for signal processing. Figure A.10 shows a photograph of the calibrator.

The main features of the Residual Intensity Calibrator are:

- Applies the same signal with zero phase difference to a pair of 1/2" or 1/4" microphones
- Driven by external signal generators
- Amplifier provides signal levels to 127 dB

Other technical specifications are listed in Figure A.11

Figure A.10: Larson Davis model CAL 291 residual intensity calibrator.

Input:	Connector: BNC Impedance: 1 M
Output:	○ Sound Pressure Level), 1% harmonic distortion): 25 - 127 dB @ 1 kHz ○ SPL difference between channels: < 0.1 dB @ 1 kHz ○ Maximum pressure-intensity index: > 27 dB
Mechanical Specifications:	Length 25.6 cm (10.3 in) Width 10.0 cm (4.0 in) Height 5.3 cm (2.1 in) Weight 1.0 kg (2.2 lb.)
Power:	DC Power: 9 - 16 Vdc, 400 mA provided by PSA004 DC Power Supply (included) 90-264 Vac @ 50 - 60 Hz

Figure A.11: Technical specifications for Larson Davis model CAL 291 residual intensity calibrator.

APPENDIX-B: PROCESSING AND VISUALIZATION SOFTWARE

B.1 Introduction

The output signals from the sensor signal conditioners are analog in nature and are converted into digital format by the NI PXI-4472 dynamic signal acquisition modules. The data thus recorded is in time-domain but the HELS methodology used for this investigation requires the acoustic pressure data at discrete frequencies. Thus some software modules are required to perform Fast Fourier Transforms (FFT) to convert the time signals into a more refined frequency data. The LabView software package distributed by the National Instruments seemed to be the obvious choice because of its seamless interface with the data acquisition hardware and easy availability of FFT and windowing routines. Furthermore, some customized routines for sound and vibration computations were also available in the LabView Sound and Vibration Toolset.

For acquiring field microphone locations, 3D digitizer Freept3D software and driver were used as an interface between the control box and the computer terminal. The digitizer software gives the coordinates of the digitized point either in Microsoft Excel format or in ASCII format. Another commendable feature of this software is “keyboard emulation”. This feature allows the coordinates to be written in any text input software as per the format given by the user. A near seamless connection was formed with a LabView program written to acquire the field microphone locations by employing this feature.

Thus, all the hardware components were controlled by the VIs written in LabView and the whole HELS system was controlled through a single GUI window. This

increases the viability of the system as it reduces the dependability on specialized personnel.

The acoustic pressure data over the user defined frequency range processed by LabView is then taken as input to the HELS program and the acoustic parameters are reconstructed over the desired locations. For brevity, the details of LabView and HELS programming are not provided in this thesis. However, some screenshots of block diagrams of VIs used to process the data are shown as follows. VIs were also created for visualization of acoustic parameter's distribution. Screenshots of such VIs are also presented.

B.2 Modified HELS Processing VI Block diagrams

The output signals from the sensor signal conditioners are analog in nature and are converted into digital format by the NI PXI-4472 dynamic signal acquisition modules. The data thus recorded is in time-domain but the HELS methodology used for this investigation requires the acoustic pressure data at discrete frequencies. Thus some software modules are required to perform Fast Fourier Transforms (FFT) to convert the time signals into a more refined frequency data. The LabView software package distributed by the National Instruments seemed to be the obvious choice because of its seamless interface with the data acquisition hardware and easy availability of FFT and windowing routines. Furthermore, some customized routines for sound and vibration computations were also available in the LabView Sound and Vibration Toolset.

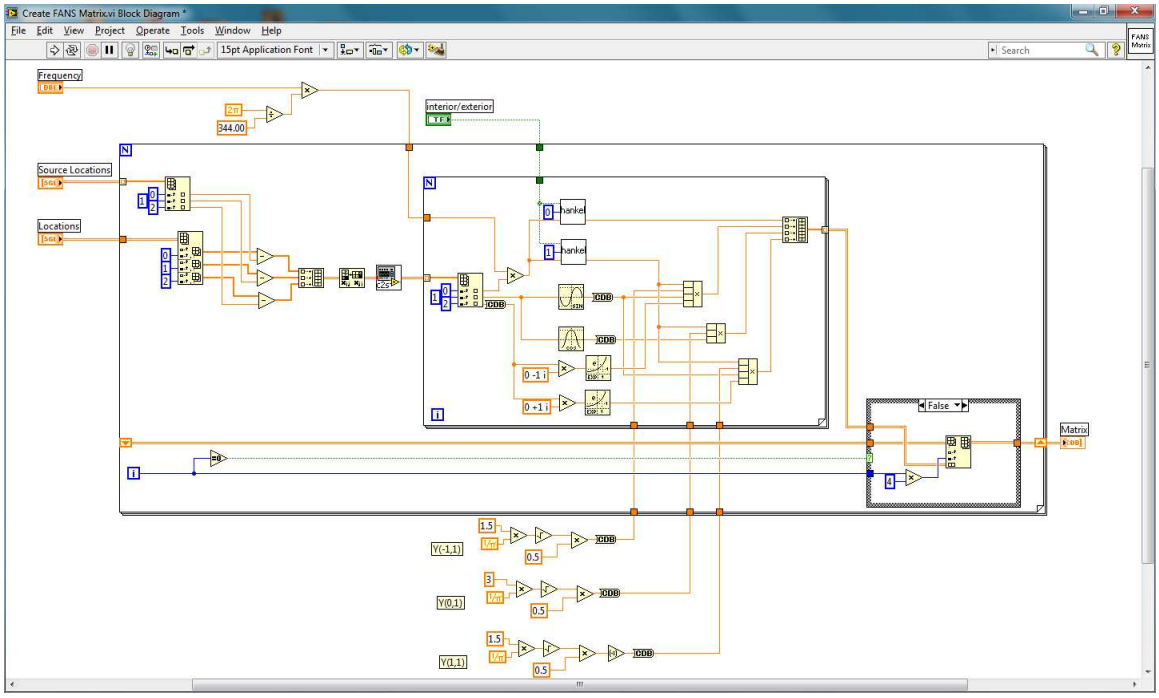

Figure B.1: Block diagram of the VI that creates the Φ_f matrix in Eq 3.3a

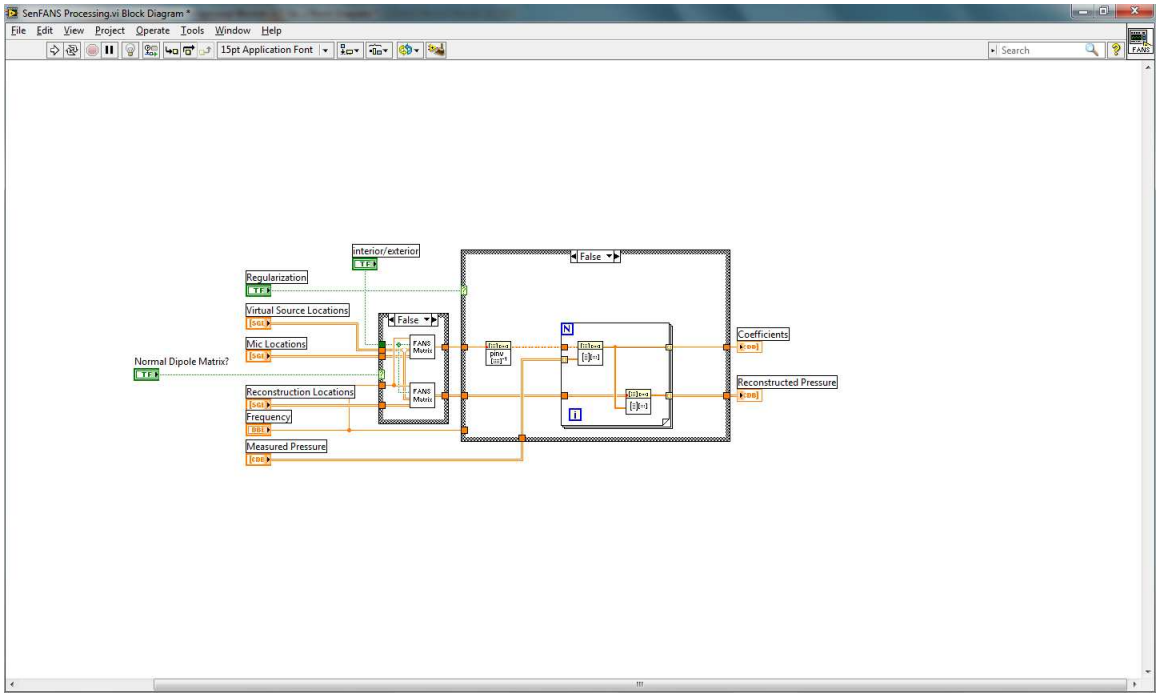

Figure B.2: Block diagram of the VI that calculates coefficients and reconstructs acoustic pressure at a given frequency.

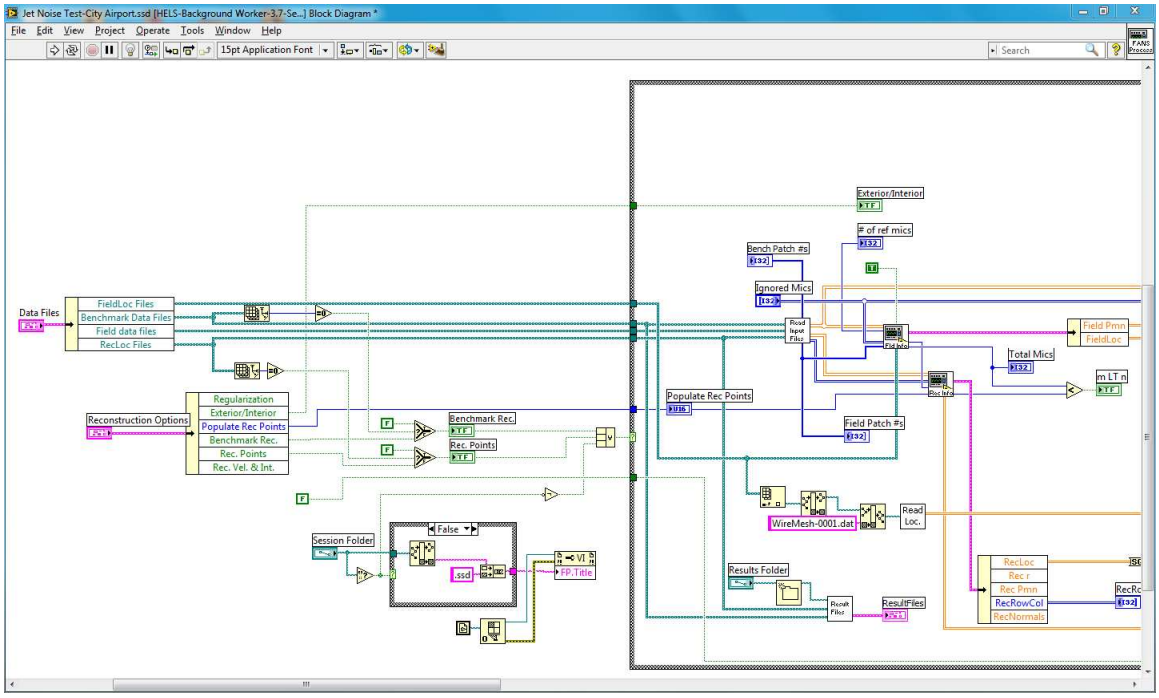

Figure B.3a: Block diagram of the VI that prepares measured data for processing and calculates coefficients and reconstructs acoustic pressure for a given frequency range.

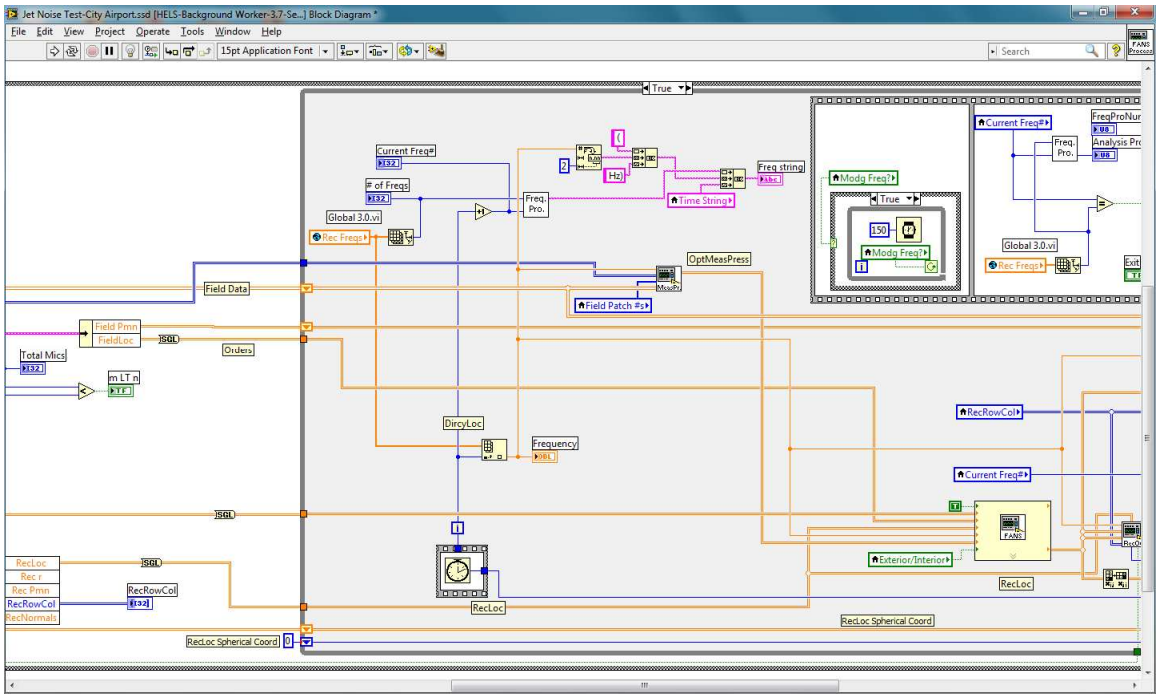

Figure B.3b: Block diagram of the VI that prepares measured data for processing and calculates coefficients and reconstructs acoustic pressure for a given frequency range.

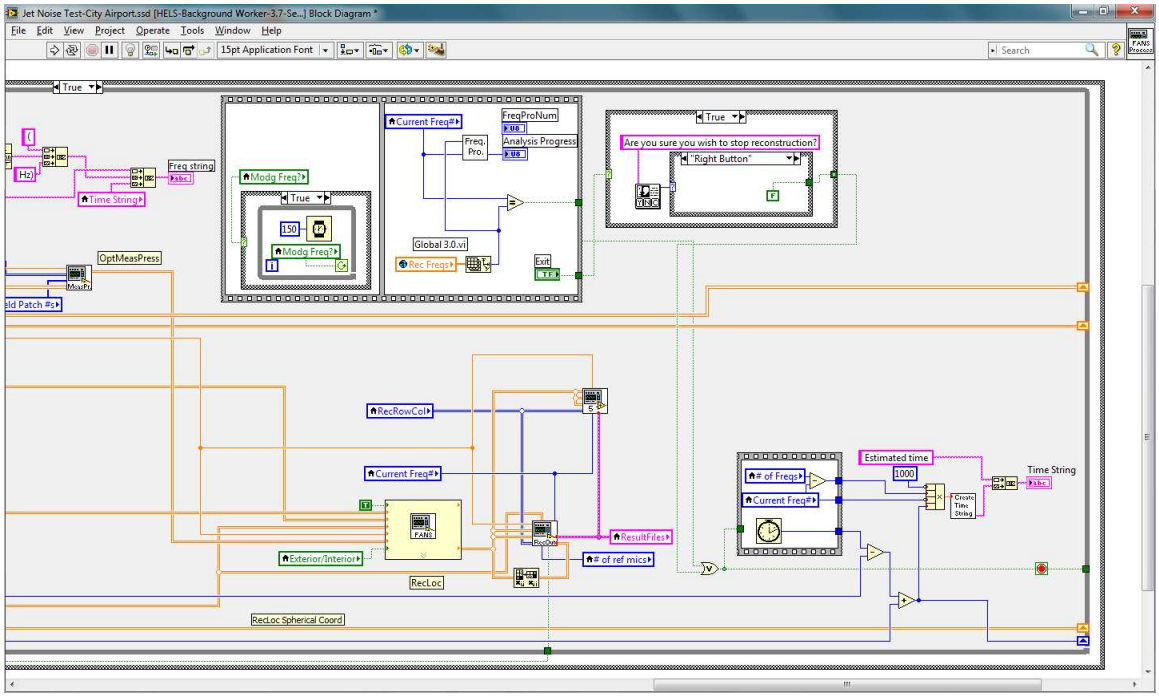

Figure B.3c: Block diagram of the VI that prepares measured data for processing and calculates coefficients and reconstructs acoustic pressure for a given frequency range.

B.3 Visualization Software Interface

Visualization software modules were also created for post-processing of acoustic field distribution data generated by HELS and modified HELS algorithms. Two different interfaces were created for stationary and non-stationary data post processing. Figure B.4a shows the main user interface screen of visualization module for stationary data. Figure B.4b shows the main interface for post-processing time-varying data and figure B.4c shows the main interface for post-processing data that varies with rpm of rotating machinery. For brevity, only the GUIs of visualization software are shared in this work.

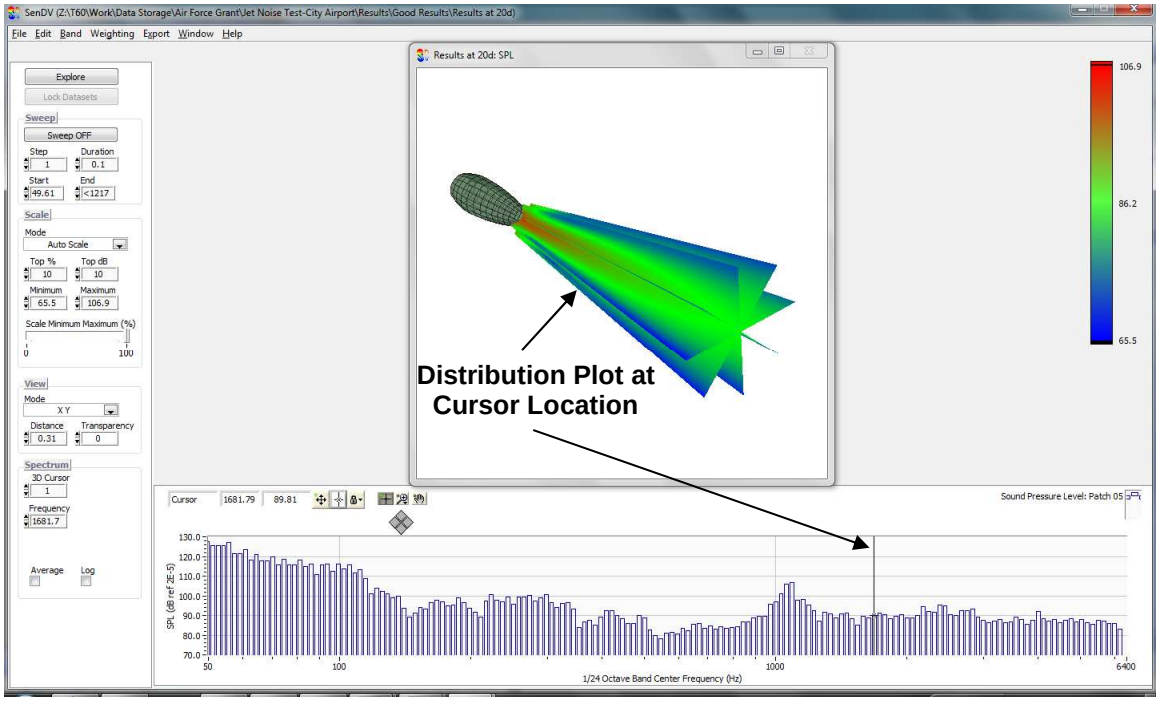

Figure B.4a: User interface for visualizing stationary data. Notice that the contour plot corresponds to the cursor frequency location in the SPL spectra under it.

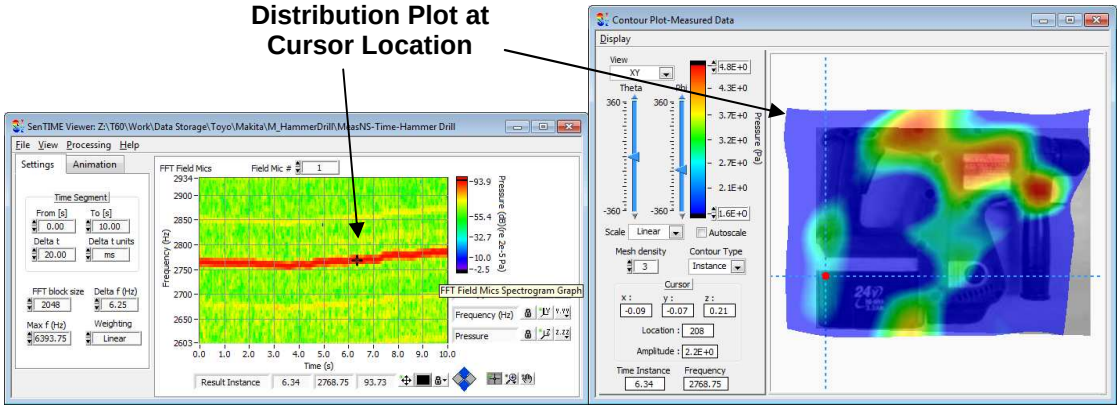

Figure B.4b: User interface for visualizing time-varying data. Notice that the contour plot corresponds to the frequency and time instant cursor location in the STFT spectrogram on the left.

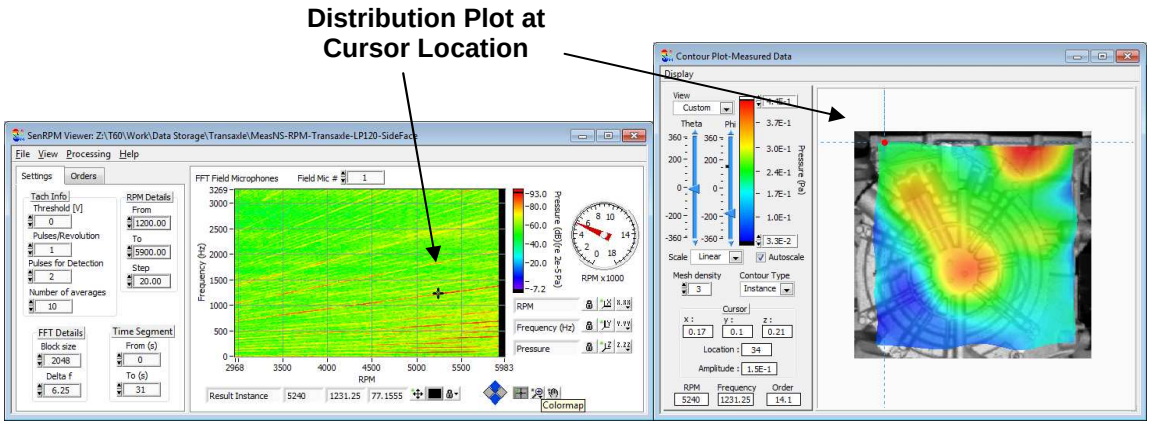

Figure B.4c: User interface for visualizing rpm-varying data measured for rotating machinery. Notice that the contour plot corresponds to the frequency and RPM cursor location in the STFT spectrogram on the left.

REFERENCES

1. B. P. Hildebrand and B. B. Brenden, *An Introduction to Acoustical Holo-graph* (Plenum, New York, 1974).

2. Bai, M.R., "Application of BEM (boundary element method)-based acoustic holography to radiation analysis of sound sources with arbitrarily shaped geometries," J. Acoust. Soc. Am., 1992, Vol. 92, pp. 533-549.

3. Hald, J., "STSF- A Unique Technique for Scan-Based Near-Field Acoustic Holography Without Restrictions on Coherence," Brüel & Kjær *Technical Review*, No. 1, 1989.

4. Hildebrand B. P. and Brenden B. B. (1974). *An introduction to Acoustic Holography*. Plenum Press, New York.

5. Kim, G.T. and Lee, B.T., "3-D Sound Source Reconstruction and Field Reproduction using the Helmholtz Integral Equation", Journal of Sound and Vibration, 1990, 136, pp. 245-261.

6. Koopmann, G.H., Song, L. and Fahnline, J.B., "A Method for Computing Acoustic Fields Based on the Principle of Wave Superposition," J. Acoust. Soc. Am., 1989, Vol. 86 (6), pp. 2433-2438.

7. Leo L. Beranek and István L. Vér; edited by; *Noise and Vibration Control Engineering: Principles and Applications*, John Wiley & Sons, 1992.

8. Lim, B.D. and Wu, S.F., “Determination of the optimal number of expansion terms in the HELS method,” *J. Acoust. Soc. Am*., 2000, Vol. 108, pp. 2505.

9. Maynard, J.D., Williams, E.G. and Lee, Y., “Nearfield Acoustic Holography; I. Theory of Generalized Holography and the Development of NAH,” *J. Acoust. Soc. Am*., 1985, Vol. 78 (4), pp. 1395-1413.

10. Morse, P.M. and Ingard, K.U., *Theoretical Acoustics*, Princeton University Press, 1986.

11. J. W. Goodman, *Introduction to Fourier Optics* (McGraw-Hill, New York,1968)

12. Pierce, A.D., Acoustics, *An introduction to its physical principles and applications*, Published by the Acoustical Society of America through the American Institute of Physics, 1994.

13. Rayess, N.E. and Wu, S.F., “Experimental Validations of the HELS Method for Reconstructing Acoustic Radiation from a Complex Vibrating Structure,” *J. Acoust. Soc. Am*., 2000, Vol. 107 (6), pp. 2955-2964.

14. Rayess, N.E., *An investigation in acoustic holography using the Helmholtz equation-least squares method*, Wayne State University, Detroit, Ph.D. Dissertation, 2001.

15. Sean F. Wu and Jingyou Yu, “Reconstructing interior acoustic pressure fields via Helmholtz equation least-squares method,” *J. Acoust. Soc. Am*., 1998, Vol. 104 (4), pp. 2054-2060.

16. Sean F. Wu, “On Reconstruction of Acoustic Pressure Fields by Using HELS Method,” J. Acoust. Soc. Am., 2000, Vol. 107, pp. 2511-2522.

17. Veronesi, W.A. and Maynard, J.D., “Digital Holographic Reconstruction of Sources with Arbitrarily Shaped Surfaces,” *J. Acoust. Soc. Am*., 1989, Vol. 85 (2), pp. 588-599.

18. Veronesi, W.A. and Maynard, J.D., “Nearfield Acoustic Holography (NAH) II. Holographic Reconstruction and Computer Implementation,” *J. Acoust. Soc. Am*., 1987, Vol. 81 (5), pp. 1307-1322.

19. Wang, Z. and Wu, S.F., “Helmholtz Equation-Least Squares Method for Reconstructing the Acoustic Pressure Field,” *J. Acoust. Soc. Am.*, 1997, Vol. 102 (4), pp. 2020-2032.

20. Wang, Z., *Helmholtz Equation-Least Squares (HELS) Method for Inverse Acoustic Radiation Problems*, Wayne State University, Detroit, Ph.D. Dissertation, 1995.

21. Williams, E.G., Dardy, H.D. and Washburn, K.B., “Generalized Nearfield Acoustical Holography for Cylindrical Geometry: Theory and Experiment,” *J. Acoust. Soc. Am*., 1987, Vol. 81 (2), pp. 389-407.

22. Williams, E.G., *Fourier Acoustics, Sound Radiation and Nearfield Acoustical Holography*, Academic Press, London, 1999.

23. Williams, E.G., Houston B.H., Herdic P.C., Raveendra S. T. and Gardner B., “Interior near-field acoustical holography in flight,” *J. Acoust. Soc. Am.*, 2000, Vol. 108, pp. 1451.

24. Williams, E.G., Houston, B.H. and Bucaro, J.A., “Broadband Nearfield Acoustical Holography for Vibrating Cylinders,” *J. Acoust. Soc. Am.*, 1989, Vol. 86 (2), pp. 674-679.

25. Williams, E.G., Houston, B.H. and Herdic, P.C., “Reconstruction of the Surface Velocity and Interior Acoustic Intensity from an Aircraft Fuselage using NAH,” *Noise-Con96*, Seattle, October 1996.

26. Williams, E.G., Maynard, J.D. and Skudrzyk, E., “Sound Source Reconstruction using a Microphone Array,” J. Acoust. Soc. Am., 1980, Vol. 68 (1), pp. 340-344.

27. Bajwa, Manjit S., *Reconstruction of transient acoustic radiation from impulsively accelerated objects*, Wayne State University, Detroit, Masters’ Thesis, 2001.

28. H. M. Smith, *Principles of Holography* (Wiley-Interscience, New York, 1969).

29. E. G. Williams and J. D. Maynard, *Numerical evaluation of the Rayleigh integral for planar radiators using the FFT*, J. Acoust. Soc. Am.72, 2020–2030 (1982).

30. E. G. Williams and J. D. Maynard, *Holographic imaging without the wavelength resolution limit*, Phys. Rev. Lett.45, 554–557 (1980).

31. E. G. Williams, J. D. Maynard, and E. Skudrzky, *Sound source recon-structions using a microphone array*, J. Acoust. Soc. Am. 68, 340–344(1980).

32. E. G. Williams, H. D. Dardy, and R. G. Fink, *Nearfield acoustical holography using an underwater automated scanner*, J. Acoust. Soc. Am. 78, 789–798 (1985).

33. P. R. Stepanishen and K. C. Benjamin, *Forward and backward projection of acoustic fields using FFT methods*, J. Acoust. Soc. Am.71,803–812 (1982).

34. M. C. Junger and D. Feit, *Sound, Structures, and Their Interactions*, (MIT, Cambridge, MA, 1972), pp. 403–432.

35. S. Hayek and T. Luce, *Aperture effects in planar nearfield acoustical imaging*, Trans. ASME, J. Vib., Acoust., Stress, Reliab. Des. 110, 91–96 (1988).

36. E. G. Williams, B. H. Houston, and P. C. Herdic, *Fast Fourier transform and singular value decomposition formulations for patch nearfield acous-tical holography*, J. Acoust. Soc. Am. 114, 1322–1333 (2003).

37. A. Sarkissian, *Extension of measurement surface in near-field acoustic holography*, J. Acoust. Soc. Am.115, 1593–1596 (2004).

38. A. Sarkissian, *Method of superposition applied to patch near-field*, J. Acoust. Soc. Am.118, 671–677 (2005).

39. M. Lee and J. S. Bolton, *Patch near-field acoustical holography in cylin-drical geometry*, J. Acoust. Soc. Am.118, 3721–3732 (2005).

40. F. J. Harris, *On the use of windows for harmonic analysis with the dis-crete Fourier transform*, Proc. IEEE66, 51–83 (1978).

41. J. W. Tukey, *An introduction to the calculations of numerical spectrum analysis*, in Spectral Analysis of Time Series, edited by B. Harris (Wiley, New York, 1967), pp. 25–46.

42. T. Loyau and J.-C. Pascal, *Broadband acoustic holography reconstruction from acoustic intensity measurements. I: Principle of the method*, J. Acoust. Soc. Am.84, 1744–1750 (1988).

43. T. Semenova, *On the behavior of HELS solutions for sound radiation and reconstruction*, Ph.D. thesis, Department of Mechanical Engineering, Wayne State University, pp. 113–123 (2004).

44. H. Lu, *Reconstruction of vibroacoustic responses using Helmholtz equation least squares method*, Ph.D. thesis, Wayne State University, Detroit, Michigan (2007).

45. Manmohan Moondra and Sean F. Wu, *Visualizing Airplane Propeller Noise*, Project report, SenSound LLC.

46. C. Hunter, *CFD software and post-processing tool help quiet the skies*, Case Studies, NASA Langley Research Center, 2003.

47. J. M. Seiner, *A new rational approach to jet noise reduction*, Theoretical and Computational Fluid Dynamics, Vol. 10, 373 – 383 (1998).

48. D. Papamoschou and R. S. Shupe, *Effect of nozzle geometry on jet noise reduction using fan flow deflectors*, the 12th AIAA/CEAS Aeroacoustics Conference (the 27th AIAA Aeroacoustics Conference), 8 - 10 May 2006, Cambridge, Massachusetts.

49. P. J. Bobbitt, K. S. Abdol-Hamid, A. Wulf, and A. F. Tinetti, “Jet plume flow solutions,” NASA/CR—2001- 210706 (2001).

50. F. A. Agboola, J. Bridges, and N. Saiyed, *Measurements of Infrared and Acoustic Source Distributions in Jet Plumes*, NASA/TM—2004-213042, 2004.

51. S. M. Dash, *Simulation of laboratory jets and full scale exhaust plumes*, Proceedings of FEDSM'03: the 4th ASME/JSME Joint Fluids Engineering Conference Honolulu, Hawaii, USA, July 6-11, 2003.

52. J. B. Freund, S. K. Lele, and P. Moin, *Direct Numerical Simulation of a Mach 1.92 Turbulent Jet and its Sound Field*, AIAA Journal, 38(11):2023-2031, 2000.

53. J. B. Freund, *Noise Sources in a Low-Reynolds Number Turbulent Jet at Mach 0.9*, Journal of Fluid Mechanics, 438: 277 – 305, 2000.

54. A. Uzun, *3-D Large Eddy Simulation for Jet Aeroacoustics*, PhD Thesis, School of Aeronautics and Astronautics, Purdue University, West Lafayette, IN, December 2003

55. L. A. Garrison, A. S. Lyrintzis, and G. A. Blaisdell, *RANS-based noise predictions of jets with internal forced mixers*, AIAA Paper 2006-2599, the 12th AIAA/CEAS Aeroacoustics Conference (the 27th AIAA Aeroacosutics Conference), 8 – 10 May 2006, Cambridge, Massachusetts.

56. Sean F. Wu, *Far-field analysis of noise sources*, U.S. Patent Reference No. 67,021-006.

57. Lighthill, M.J., *On sound generated aerodynamically: I. General theory*, Proceedings of the Royal Society of London A, 222, 1952, pp. 564-587.

58. Ffowcs Williams, J. E., *The noise from turbulence convected at high speed*, Phil Trans Roy Soc. Lond. 255, 1963, pp 469-503.

59. Dowling, A. P., Ffowcs Williams, J. E., and Goldstein, M. E., "Sound production in a moving stream". Phil Trans. Roy. Soc. Lond., A 288, 1978, pp 321-349.

60. Mani, R., *The influence of jet flow on jet noise*, Parts 1 and 2. J. Fluid Mech., 73, 1976, pp 753-793.

61. Lilley, G. M., *On the noise from jets*, Noise Mechanisms, CP-131-Agard, 1974, 113.1-13.12.

62. C. K. W. Tam, N. N. Pastouchenko, and R. H. Schlinker, *On the two sources of supersonic jet noise*, AIAA paper no. AIAA-2003-3163, May 2003.

63. J. Hileman, B. Thurow, and M. Samimy, *Exploring noise sources using simultaneous acoustic measurements and real-time flow visualizations in jets*, AIAA J. 40(12), 2382-2392 (2002)

64. L. D. Koch, J. Bridges, C. Brown, and A. Khavaran, *Experimental and analytical determination of the geometric far-field for round jets*, Noise Control Eng. J. 53(1), 20-29 (2005)

65. H. Xia, P.G. Tucker, S. Eastwood, M. Mahak, *The influence of geometry on jet plume development*, Progress in Aerospace Sciences, Applied Computational Aerodynamics and High Performance Computing in the UK, Volume 52, July 2012, Pages 56–66

66. Logesh Natarajan, Sean F Wu, *Panel acoustic contribution analysis*, Journal of Acoustical Society of America, Volume 133, Issue 2, pp. 799-809, February 2013

67. Logesh Natarajan, Sean F Wu, Reconstructing the normal surface velocity on a baffled plate using the Helmholtz equation least squares method, Journal of Acoustical Society of America, 131 (6), pp. 4570-4583, June 2012

68. Tatiana Semenova and Sean F. Wu, *On the choice of expansion functions in the Helmholtz equation least-squares method*, Journal of Acoustical Society of America, 117 (2), pp. 701-710, Nov 2004

ABSTRACT

VISUALIZING INTERIOR AND EXTERIOR JET AIRCRAFT NOISE

by

MANMOHAN SINGH MOONDRA

May 2014

Advisor: Dr. Sean F. Wu

Major: Mechanical Engineering

Degree: Doctor of Philosophy

In today's competitive aerospace industry, the quest for quiet has drawn significant attention to both the interior and exterior design of an airplane. Understanding the noise generation mechanisms of a jet aircraft is a crucial first step toward developing the most cost-effective noise and vibrations abatement methods. In this investigation, the Helmholtz Equation Least Squares (HELS) based nearfield acoustic holography will be used to understand noise transmission caused by jet engine and turbulence into the fuselage of a jet aircraft cruising at 30,000 ft.

Modern propulsive jet engines produce exterior noise sources with a high amplitude noise field and complicated characteristics, which makes them very difficult to characterize. In particular, there are turbulent eddies that are moving through the jet at high speeds along the jet boundary. These turbulent eddies in the shear layer produce a directional and frequency dependent noise. The original HELS approach assumes a

spherical source at the origin and computes the acoustic field based on spherical emission from this source. This assumption of one source at the origin is not sufficient to characterize a complex source like a jet. As such, a modified HELS approach is introduced that will help improve the source characterization as it is not dependent on a single source at the origin but a number of virtual sources throughout the space. Custom microphones are created to take acoustic pressure measurements around the jet engine. These measured acoustic pressures are then taken as input to the modified HELS algorithm to visualize the noise pattern of a subsonic jet engine.

AUTOBIOGRAPHICAL STATEMENT

Manmohan Moondra received a B.E. in Mechanical Engineering in 1997 from Punjab Engineering College, Chandigarh, India. Later he taught undergraduate students mechanical engineering at his alma mater as adjunct faculty. He enrolled into a MS program in Mechanical Engineering at Wayne State University in 2000. He won several student paper competition awards at various professional society meetings. In 2001, he won the Second Place Award in the student technical paper competition held at the 2001 SAE International Noise and Vibration Conference and Exposition, Traverse city, Michigan. He won the Best Student Paper Award at the 2001 ASME International Mechanical Engineering Congress and Exposition held in the New York City, New York. He won the 2002 Student Paper Prize at the Inter-Noise 2002, the 31st International Congress and Exposition on Noise Control Engineering held in Dearborn, Michigan. He won the First Place Award in the student paper competition of the 143rd meeting of the Acoustical Society of America held in Pittsburgh, Pennsylvania in June 2002. In 2003, he received the Thomas C. Rumble University Graduate Fellowship and won the First Place Award in the student technical paper competition held at the 2003 SAE International Noise and Vibration Conference and Exposition, Traverse city, Michigan. He later joined SenSound LLC, a Wayne State University startup company based on his research in 2004 as Lead Product Development engineer and continued to develop noise-imaging products based on the HELS method while working on his dissertation.